DESIGN AND FABRICATION OF DYE-SENSITIZED SOLAR CELL USING SELF-SYNTHESIZED QUATERNARY (TiO_2/ZnO/CdS/GRAPHENE) NANOCOMPOSITE BY PULSED LASER ABLATION TECHNIQUE

BY

Abdul-Mojeed Olabisi ILYAS

A Thesis Presented to the
DEANSHIP OF GRADUATE STUDIES

KING FAHD UNIVERSITY OF PETROLEUM & MINERALS
DHAHRAN, SAUDI ARABIA

In Partial Fulfillment of the
Requirements for the Degree of

MASTER OF SCIENCE

In

PHYSICS

DECEMBER, 2015

KING FAHD UNIVERSITY OF PETROLEUM & MINERALS
DHAHRAN- 31261, SAUDI ARABIA
DEANSHIP OF GRADUATE STUDIES

This thesis, written by **ABDULMOJEED OLABISI ILYAS** under the direction of his thesis Advisor and approved by his thesis Committee, has been presented and accepted by the Dean of Graduate Studies, in partial fulfillment of the requirements for the degree of **MASTERS OF SCIENCE IN PHYSICS.**

m. a. Gondal

Dr. Mohammad A. Gondal
(Advisor)

Dr. Abdullah A. Al-Sunaidi
Department Chairman

Dr. Zain Hassan Yamani
(Member)

Dr. Salam A. Zummo
Dean of Graduate Studies

Dr. Mohamed M. Faiz
(Member)

3/1/16

Date

This project is dedicated to the Giver of knowledge and Nourisher of wisdom who makes my academic life worthy of living

ACKNOWLEDGMENTS

All the praises and thanks be to Allah, the Lord of the worlds, and The Most Merciful.

I would like to express my sincere gratitude to: Dr. M. A Gondal (Distinguished Professor) for accepting me as a Masters student, giving me guidance in my research, supporting and giving me freedom to think and develop my personality

I would like to pay special thanks to: Dr. Zain Hassan Yamani for giving constructive criticism, financial support and countless encouragement, during my academic career in KFUPM. Dr. Mohamed M. Faiz for accepting to be my committee member and teaching me X-ray photoelectron spectroscopy analysis technique. Dr. Ibraheem M. A. Nasser for counselling me. Members of Laser research lab, center of excellence in nanotechnology and center of engineering research who, one way or another had shared in my lab activities such chemical preparation and sample characterization . Past and present chairman of Department of Physics and the faculty members.

Most of all, a great debt is owed to my parents Alh. Ilyas I.O, Mrs Ilyas N.A and My siblings and wife (HYA) for their quiet patience and unending spiritual, mutual, financial and loving support during my repeated absences. May Allah, subhanahu wa ta'ala, bless and continue to guide them to the right path.

TABLE OF CONTENTS

LIST OF TABLES

LIST OF FIGURES

ABSTRACT

Full Name : [ABDUL-MOJEED OLABISI ILYAS]

Thesis Title : [DESIGN AND FABRICATION OF DYE-SENSITIZED SOLAR CELL USING SELF-SYNTHESIZED QUATERNARY (TIO_2/ZNO/CDS/GRAPHENE) NANOCOMPOSITE BY PULSED LASER ABLATION TECHNIQUE]

Major Field : [PHYSICS]

Date of Degree : [DECEMBER, 2015]

Pollutant-free water and clean energy are the important challenges we currently face in the universe. Chemically stable and highly active materials are needed to solve these challenges. The drawbacks faced by existing catalysts are: (a) recombination of the photogenerated carrier and (b) restricted activity in the ultraviolet (UV) region. Therefore, designing semiconductor based composites is a promising approach to eliminate these drawbacks. Prominent semiconductors such as TiO_2, ZnO, cadmium sulfide (CdS), silicon carbide (SiC) and graphene were chosen for this purpose. In this work, CdS and graphene were first synthesized by a chemical method separately and then ZnO/TiO_2, TiO_2/CdS, TiO_2/SiC and TiO_2/graphene hybrid catalyst were prepared in different weight percentage ratio. The synthesized materials were then applied in the degradation of methyl orange (MO) dye and as photoanode in the dye-sensitized solar cell. The results obtained show that ZnO NR/TiO_2 NP of 9:1 weight ratio, TiO_2 with 1:10 weight ratio of CdS, SiC, and graphene have the best activity out of all the above mentioned binary nanocomposite. In order to have an excellent control over the enhanced performance in the best nanocomposite, a pseudo code was written to effectively combine the best binary composite to form ZnO/TiO_2/CdS/SiC and ZnO/TiO_2/CdS/graphene quaternary nanocomposite. However, the binary and quaternary composite were synthesized by an optical route known as Pulsed Laser Ablation in Liquid (PLAL) technique. The structural, optical, morphological and compositional studies were conducted on the binary and quaternary composite using XRD, SEM, TEM, FTIR, UV-Vis spectroscopy, Raman spectroscopy and XPS. Compared to ZnO, P-25 TiO_2, and binary composite catalysts, the quaternary composites show enhanced photovoltaic performance.

ملخص الرسالة

الاسم الكامل: عبدالمجيد اولابيسي ايلياس

عنوان الرسالة: تصميم وتوليف خلايا شمسية صبغية ذات حساسية بإستخدام التوليف الرباعي الذاتي (أكسيد الزنك- اكسيد التيتانيوم- كبريتيد الكادميوم-جرافين) نانوية التركيب بإستئصال الليزر النبضي

التخصص: فيزياء

تاريخ الدرجة العلمية: يناير 2015 م

يعتبر الحصول على ماء و طاقة نظيفة غير ملوثة من اهم التحديات التي تواجه العالم في الوقت الحاضر.و تعتبر المواد الكيمياءية عالية الثبات و النشاط احدي اهم طرق حل هذه المشكلة. العيب التي تواجهها المحفزات القائمة تشمل إعادة الاتحاد للشحنات المولدة بفعل الضوء من الناقل والنشاط المحدود في منطقة الأشعة فوق البنفسجية . لذلك، فان تصميم المواد المركبة القائمة على أشباه الموصلات هو نهج واعد للقضاء على هذه العيوب. وقد تم اختيار أشباه الموصلات بارزة مثل اكسيد التايتينيوم النانوية و أكسيد الزنك و كبريتيد الكادميوم، و كربيد السيليكون والجرافين لهذا الغرض. تم توليفها كبريتيد الكادميوم والجرافين لأول مرة على طريقة كيميائية وأعدت أكسيد الزنك / اكسيد التايتينيوم ، اكسيد التايتينيوم / كبريتيد الكادميوم ، اكسيد التايتينيوم / كربيد و اكسيد التايتينيوم / الجرافين في نسبة الوزن مختلفة. طبقت المواد في تحليل صبغ الميثيل البرتقالي و مثل قطب سالب في الخلية الشمسية توعية الصبغة. أظهرت النتائج أن أكسيد الزنك / اكسيد التايتينيوم من 9: 1 نسبة الوزن، اكسيد التايتينيوم مع 01:10 نسبة الوزن من كبريتيد الكادميوم، كربيد، والجرافين دينا أفضل النشاط من جميع بمركب متناهي في الصغر ثنائي. من أجل أن يكون لها سيطرة ممتازة على تحسين الأداء في أفضل بمركب متناهي في الصغر، وكتب رمز الزائفة إلى الجمع بين فعالية أفضل مركب ثنائي لتشكيل أكسيد الزنك / اكسيد التايتينيوم / كبريتيد الكادميوم / كربيد وأكسيد الزنك / اكسيد التايتينيوم / كبريتيد الكادميوم / الجرافين الرباعية بمركب متناهي في الصغر. وبالتالي، تم توليفها مركب ثنائي ورباعي بطريق البصرية المعروفة باسم نابض ليزر تذرية في السائل (تقنية. وقد أجريت الدراسة الهيكلية، البصرية، الصرفية والتركيبية على مركب ثنائي ورباعي باستخدام حيود الأشعة السينية، المجهر الالكتروني والأشعة فوق البنفسجية فيس التحليل الطيفي، رامان الطيفي و XPS. بالمقارنة مع أكسيد الزنك NR، اكسيد التايتينيوم ، ومركب ثنائي، يظهر مركب رباعي تحسين الأداء الضوئية.

CHAPTER ONE

INTRODUCTION

Energy and water are the basic elements for human survival. As the magnitude of energy requirement are approaching an unprecedented stage, mankind seeks for additional energy resources which brought the technology advancement. Nowadays, the highest percentage of the world energy requirement is supplied by fossil fuel[1]. Since energy is an essential ingredient for human transactions, the increase in world population and rising energy demand has led to gradual decrease in a quantity of oil reserve, an increase in the price of fossil fuel and several economic disaster. In addition, the continuous exploitation of fossil fuel has led to some different new undesirable phenomena like climate change, ozone layer depletion, acid rain and greenhouse effect[2]. These phenomena are understood scientifically to be related to the greenhouse gasses emitted when the fossil is burnt. Carbon dioxide (CO_2) and methane (CH_4) are examples of greenhouse gases which hinder the long-wavelength terrestrial radiation from escaping into space warming the earth's troposphere which becomes warmer. However, there is a need to explore inexhaustible, environmentally friendly and readily available energy sources. An example of CO_2 free technology is the nuclear power plant. Yet its unsolved problems such as availability of uranium and storage of radioactive waste create a setback[3]

Alternatives available sources include energies from sunlight, the wind, tides and geothermal. Apart from energy from the sun, other renewable energy suffer from lack of availability, geographical location and the high cost of management[4]. Solar energy is known to be one of the most prominent of these renewable energy sources. It is the root of all source of energies and the most ancient source. The acquisition of solar energy is achieved by using photovoltaic devices. The smallest unit of these devices is known as solar cell. The illumination power from the sun is about ten times the current energy demand. In 1954, bell laboratories designed the first practical photovoltaic cell with an efficiency of 6% using diffused silicon p-n technology [5]. Since then photoconversion efficiency of silicon-based solar cells has approached and exceeded 20% [6],[7]. Problems encountered with these solar cells include the high cost of production[8], the need for highly purified silicon and toxic chemicals requirement for its manufacture[9]. Due to these problems they have not been able to achieve grid parity [8]; hence they face restrictions to be useful worldwide[ref]. In order to combat these constraints, there is a need to search for low cost, easily manufacturable and environmentally friendly solar cells. A new photovoltaic cell was developed in 1991 by O'Regan and Gratzel [10]. This solar cell works on the principle of plant photosynthesis now known as the dye-sensitized solar cell (DSSC) was reported to have a photoconversion efficiency of 13 % [11]. It components include an electrolyte placed between a catalytic electrode, and a photoelectrode. The photoelectrode made of a thin layer of dye, is placed on a microscopic thin layer of semiconductor thin film. Hence, the spectroscopic properties of the dye, as well as the morphological properties and electrical property of electrolyte affect the photovoltaic parameters (open circuit voltage, closed circuit current density interfacial charge transfer resistance and fill factor) of the DSSC. This determines the electrical conversion efficiency [12]. Attractive features discovered so far about this device include easy fabrication, low-cost components, and usefulness in glass-based systems due to its semi-flexibility and transparency. But the difficulty in avoiding the use of expensive materials like platinum, ruthenium in dye and liquid electrolyte still pose a serious challenge[13]. So far, the photoconversion efficiency is still less than the best thin film solar cells. Logically the price /performance ratio is expected to be low in order to achieve grid parity while competing with fossil fuel generated electrical power. Therefore, to improve the competitiveness and performance of DSSC in the world market, a large number of investigations in photovoltaics focused on DSSC.

Water provides nourishment to a living organism in order to make life possible on earth. However, water pollution is a matter of great concern all over the world. The activities of food, leather and textile industries have been the major contributing factors to water pollution [14]. The removal of hazardous products in the form of dye waste from water has become an important area of research. The first characteristic of contamination in polluted water is color[15]. In the water bodies, the presence of dye noticed with color change cause luminosity loss and an increase in temperature which reduces the oxygen concentration available for the survival of the aquatic life [16]. Humans are exposed to a lot of life threatening diseases when they consume carcinogenic substances through agricultural products grown in a farm field exposed to industrial waste. Ultrafiltration, water remediation, adsorption method and biological treatment are few examples of the various method used in addressing water purification issues [17]. These methods are not favored because complete removal of pollutants is not achieved, rather only a phase change in the contaminant is acquired. Ideally, a technique is required that completely and efficiently removes the hazardous compounds with no by-product , an cost effective, requiring less energy source and catalysts which are cheap abundant and pollutant free. Hence, the technique that meets all these requirement is known as the Photodegradation process [18]

1.1 Statement of Problem.

Clean environment relies on green energy sources and unpolluted water supply. Renewable and environmentally friendly energy sources like solar energy has been an area of focus as it is readily available. Yet the conventional device used in converting solar energy into electrical energy known as silicon solar cell is costly due to energy and cost intensive processing technique. In order to solve this problem, easily made and cheap devices such as dye-sensitized solar cells (DSSC) are being developed. DSSC still face low efficiency 13 % compared to ~20% of the conventional solar cell. This is due to oxide semiconductors like TiO_2, ZnO which serve as the main building blocks of DSSC as it is responsible for electron transfer in the device. Another life-threatening technological process is in the area of industrial waste treatment. The careless disposal of industrial waste which might contain carcinogenic or toxic substances that get leached into nearby water bodies thereby hindering photosynthesis process and affecting aquatic lives. In order to remove these pollutants from water, semiconductors are used in a process known as photodegradation.

1.2 Aim and Objectives.

AIM: To synthesize a novel quaternary nanocomposite which would have excellent charge transport and reduced charge recombination by using pulsed laser ablation in liquid.

Objectives:

i. Synthesis of TiO_2/ZnO composite catalyst in different concentrations with a pulsed Nd-YAG laser in liquids.

ii. Synthesis of CdS quantum dot and deionized water suspended graphene

iii. Synthesis of TiO_2 /graphene composite catalyst in different concentration with a pulsed Nd-YAG laser in liquids.

iv. Synthesis of TiO_2 /CdS composite catalyst in different concentration with pulsed Nd-YAG laser in liquids.

v. Synthesis of TiO_2 /SiC composite catalyst in different concentration with pulsed Nd-YAG laser in liquids.

vi. Fabrication of Dye-Sensitized Solar Cell using all the binary nanocomposites

vii. Applying the binary nanocomposite as catalyst for photodegradation of Methyl Orange (MO) dye

viii. Writing a pseudo code useful in determining the percentage weight of starting material required for ideal quaternary nanocomposite using results obtained from optimized binary nanocomposite

ix. Synthesis of quaternary (TiO_2/ZnO/CdS/Graphene or SiC) nanocomposite.

x. Characterization of all the synthesized Nano-composite (i-iv) using various techniques such as UV-Vis spectroscopy, X-ray diffraction (XRD), Photoluminescence (PL), Field Emission scanning electron microscope (FESEM), and Transmission electron microscope (TEM).

xi. Designing a special technology for preparing a thin film with very small quantity of nanoparticles obtained from pulsed laser ablation technique.

xii. Fabrication of Dye-Sensitized Solar Cell using the quaternary (TiO_2/ZnO/CdS/Graphene) nanocomposite and measuring efficiency.

CHAPTER TWO

LITERATURE REVIEW

2.1 Dye-sensitized solar cell

DSSC in modern time is composed of a porous thin layer of oxide semiconductor nanoparticles, coated with dye molecules that are sunlight sensitive. The substrate of the thin semiconductor film which serves as the anode and the cathode is coated with a platinum-based catalyst. In between this two electrodes with dye-coated nanoparticles, an electrolyte solution is immersed to convey generated electric charges within the solar cell. Hence, the properties and functions of the basic components of DSSC: the semiconductor, dye, electrolyte, and electrode are discussed below

2.1.1Transparent conductive substrate

Two transparent conductive glasses are used for the construction of DSSCs; their main function is to act as a substrate for micrometer thick semiconductor and to serve as a current collector[19]. A good conductive substrate should have the following properties: (i) A transparency of >85% is needed from the substrate, in order to allow maximum sunlight to be transferred to the active area of the cell (ii) High electrical conductivity is needed for efficient charge transfer which minimizes energy loss. The two types of conductive substrate used are the indium doped tin oxide (ITO) and the fluorine doped tin oxide (FTO). Both substrates are made from soda lime glass coated. The FTO and ITO substrates have a transmittance of 75% for visible light and over 80 % respectively with a corresponding respective sheet resistance of 18 Ω/cm^2 and 8.5 Ω $/cm^2$. It has been reported that[20] the sheet resistance of ITO increases while that of FTO remain constant after being sintered for 2h at 450^oC. Also, investigation shows that the overall efficiency obtained from FTO is higher than that of ITO made from identical DSSC components. Hence, FTO is highly recommended for DSSCs due to its low sheet resistance[21].

2.1.2 The semiconductor

The semiconductor performs the following function in the DSSC (i) a surface area for the adsorption of the mesoscopic dye (ii) collection of an electron from the attached dye and (iii) the conduction of electron to the external circuit for electric current production[22]. Hence, the porosity, morphology, crystallinity and surface area of the semiconductor affect the performance of the DSSCs. The main Semiconductor materials used are oxide semiconductors such as titanium oxide (TiO_2), tin oxide (SnO_2)[23], niobium oxide (Nb_2O_5) and zinc oxide (ZnO) [24]. Experiment has shown that TiO_2 based DSSCs has a higher efficiency than ZnO and SnO_2 based DSSC. Since 1991 it has been considered an ideal semiconductor material for DSSC[25]

2.1.3 The sensitizer

The thin layer sensitizer bonded to the surface of the semiconductor layer is usually made of either quantum dot chalcogenides (PbS, CdS or CdSe) or dyes (N3, N719 or organic dyes). The main usefulness of the dye is to provide electron for the conduction band of the oxide semiconductor. The following properties are expected from a sensitizer before it can be considered efficient in a dye-sensitized solar cell. (i) Good absorption in the visible spectral region[26]. (ii) remarkable extinction coefficient[27] (iii) stability in its oxidized form such that it can be regenerated by the electrolyte (iv) long term stability for generation of electrons (v) a LUMO level that is more negative than the conduction band of the semiconductor[28] (v) a HOMO level more positive than that of the redox electrolyte [29], [30](vi) It must be a photosensitizer based on transition metals[31].

2.1.4 Electrolyte

The Electrolyte placed between the dyes coated semiconductor and the counter electrode is meant to perform two purposes (i) regenerate the electron lost by the dye during sensitization (ii) medium of charge transfer to the counter electrode. Hence, the stability of the DSSCs depends on the electrolyte property. Therefore the following are the expected characteristics of the electrolyte used in a DSSC (i) high electrical conductivity, fast diffusion of electrons, and low viscosity [32](ii) a good contact between the counter electrode and nanocrystalline semiconductor[33], and an electrolyte is not expected to (i) absorb light in the visible spectral region (ii) have the capability of degrading the dye[34], [35]. Hence, different classes of electrolyte have been investigated based on several different properties they possess. Organic electrolytes are made of redox couple such as $SCN^{-}/(SCN)_2$, Br^{-}/Br_3 [36], $SeCN^{-}/(SeCN)_2$ [37], [38], and substituted bipyridyl cobalt (III/II) [39]. They rapidly regenerate the dye with good stability and low visible light absorption and slow recombination of electrons at the semiconductor interface. Additives such as N-methyl benzimidazole (NMBI), guanidinium thiocyanate (GuNCS) [40]) and 4-tert-butylpyridine (TBP) are combined with other components in order to prevent recombination of tri-iodide ions and injected electrons. Nevertheless, leakage and high evaporation rate are the main problems faced by this electrolyte[41][42]. Hence solid state electrolytes(SSE) was developed by replacing the liquid electrolyte with a hole transfer semiconductor(inorganic(CuI, CuBr, and CuSCN) and organic(2,2′,7,7′-tetrakis(N,N-di-p-methoxyphenylamine)9,9′-spirobifluorene (OMeTAD)) which are compatible with the conduction band of the n-type semiconductor and the HOMO level of the sensitizer. However, the photoconversion efficiency obtained from SSE based DSSC is still low because the contact between the photoelectrode and SSE is poor causing increased rates of charge recombination between their interface. Hence, quasi-solid-state electrolytes made of polymer and liquid electrolyte are considered as an alternative. The electrolyte shows high electrical conductivity, good interfacial contact, and a better long-term stability and approaching an efficiency of 10% [43][44]. Hence, the phase transition encountered by this material from gel state to solution state at high temperature becomes its main problem[45]. Hence, organic liquid electrolyte remains a good option for DSSC.

2.1.5 The counter electrode

In a DSSC, the counter electrode made by coating a conductive substrate with carbon base on the Pt-based material. The electron oxidized in the electrolyte during its activity in the regeneration of the sensitizer is replenished at the counter electrode. This is achieved when the diffusing electrolyte has a good contact with the counter electrode in the DSSC enabling it to accept an electron from the external circuit. Catalyst usually used to accelerate the reduction reaction at the counter electrode is basically platinum (Pt) due to the fact that it has good catalytic activity, high transparency, and current density. The deactivation of the counter electrode is mainly achieved by the removal of the Platinum(Pt) deposited on the conductive substrate or by electrocatalytic property alteration[46]. The main disadvantage of using Pt is its high cost. Furthermore, its activity decreases with passage of time when in contact with redox couple electrolyte[47].

In summary, a DSSC consist of a micron thick semiconductor grown on a conductive substrate, a thin layer of sensitizer, an electrolyte (I_3^-/I^- and Co^{2+}/Co^{3+}redox couples) between the sensitizer, electrode and counter electrode (Pt or carbon material coated conductive glass) and conductive substrate. Hence the mechanism of the DSSC can be described as shown in figure 2.1[48]–[50], when the cell is illuminated by solar irradiation(1), the dye is oxidized and as a result, electrons excited from the ground state to the excited state in the adsorbed dye molecules are transferred to the conduction band of the wide band gap semiconductor (wbg-SC) (2) because there is a difference in the electronic state of energy levels . The electrons move to the electrode (FTO) from the CB of the wbg-SC (3). The oxidized dye is restored to its formal state by electron donation from the redox electrolyte in contact with the dye (4). The catalytic electrode in contact with the diffused electrolyte restores the electron lost by the electrolyte due to electron accepted from an external circuit (5). The processes causing reduced efficiency known as electron backward transfer from acceptor to donor are also represented with 7,8 and 9 in figure 2.1

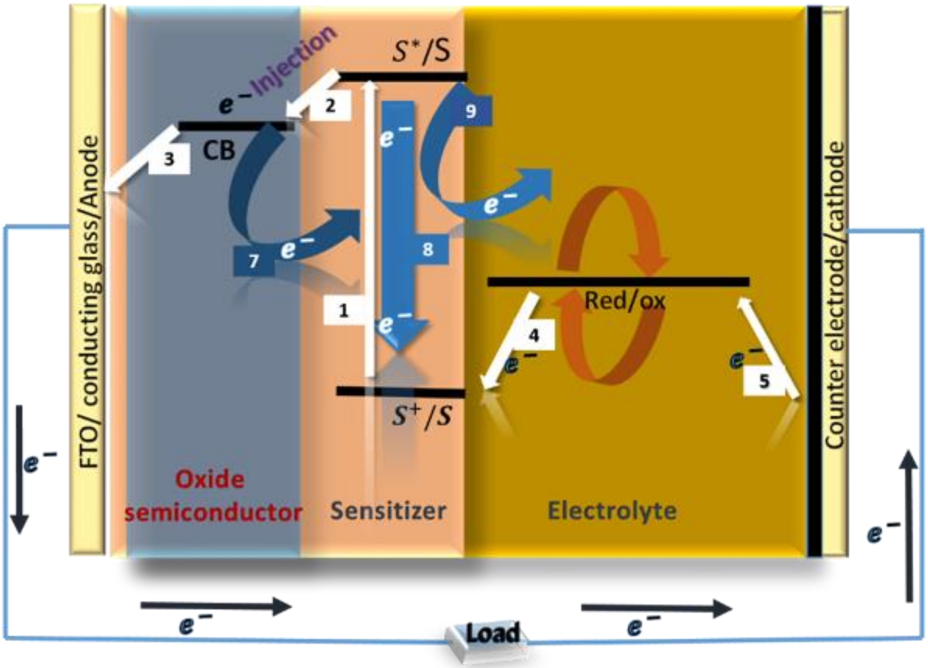

Figure 2.1 Charge transfer mechanism in DSSC

2.2 Photodegradation

The solar-driven process used in the removal of organic pollutants is known as photodegradation. It can be divided into two types (i) Photolysis and (ii) Photocatalysis.

2.2.1 Photolysis

The photolysis is a degradation process that uses solar light energy to produce ions, radicals and excited molecules in water[51]. It depends on the amount of energy and nature of the compound. The electrons, hydrogen radicals, and hydroxyl radicals are used to decompose the contaminants[52]. In a more advanced oxidation process, hydrogen peroxide, ozone or Fenton reagent are used as supporting agent in the presence of UV light to make the photolysis process more effective. The oxidizing species are the perhydroxyl and hydroxyl radicals produced in the reaction[53]. This method has an advantage over previously mentioned technique because the oxidant completely mixes with water, are commercially available, the color of the dye is completely removed and the aromatic compounds are completely degraded and the reaction occurs with no CO_2 emission, nor phase transformation problem of formation of sludge. The main setback is the low absorption rate of ultraviolet light by hydrogen peroxide[54].

2.2.2 Photocatalysis

Photocatalysis is another photodegradation process which uses solar light, but here a semiconductor is used to enhance the action of light by absorbing the photon and releasing electron-hole pair in the water containing contaminants[55]. The oxidation and reduction reaction is induced in this process by the semiconductor photocatalyst. The photocatalytic reaction requires photon energy greater than the bandgap of the semiconductor in the degradation process. This photon energy is used to excite an electron to the conduction band thereby creating hole pair within femtoseconds[56]. The mechanism shown in figure

2.2 of the photodegradation process are represented with set of equations shown below[57],[58]

$$(Semiconductor)SC + hv \rightarrow SC(e_{cb}^{-}, h_{vb}^{+})\ (1)$$

$$h^{+} + H_2O \rightarrow OH_{surf}^{\blacksquare}(hydroxyl\ radical) + H_{aq}^{+}(2)$$

$$e^{-} + O_2 \rightarrow O_2^{\blacksquare -}(oxygen\ radicals)(3)$$

$$OH_{surf}^{\blacksquare} + dye \rightarrow end\ products(4)$$

$$O_2^{\blacksquare -} + dye \rightarrow end\ products\ (4)$$

The end products usually comprise of CO_2 and H_2O (5).

The semiconductor is excited by photons to release reductive conduction band electron and oxidative valence band hole (1). Hydroxyl radicals are produced when the holes react with the H_2O (2) or else directly to oxidize the organic dye into radicals. The oxygen scavenges the electrons to form superoxide radical anions (3). The radicals are the reagents that take part in the rapid oxidation of the organic compounds (4 and 5). Hence, the end product is water from organic pollutants with the photocatalyst suspended in it.

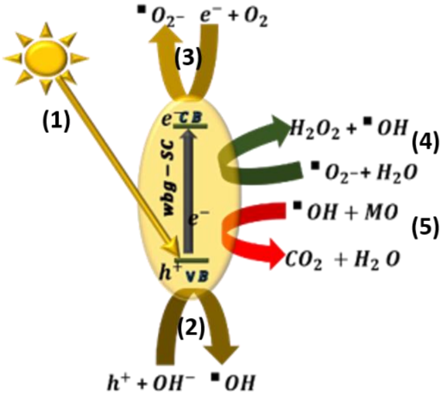

Figure 2.2 Photodegradation mechanism using MO dye as model pollutant

The photocatalysis process can be divided into the following steps: Transfer of the semiconductor to the organic contaminants prepared in water, the organic contaminants get adsorbed to the surface of the semiconductor, the surface is activated by photons, photocatalysis of the adsorbed organic contaminant on the semiconductor surface, and the intermediate species formed at the surface of the semiconductor during photocatalysis is desorbed.

The following are the properties of a semiconductor which would have excellent photocatalytic properties:

(i) The semiconductor must have a good surface area because this enhances the surface adsorption of the contaminants to the surface of the semiconductor and it improves its photocatalytic reaction[59], [60].

(ii) Electron-hole pair recombination at the surface of the semiconductor should be minimal so that charge carrier (electrons or hole) would be available for the photocatalytic reaction[61][62]

(iii) The semiconductors should be active both in the UV and visible spectral region in order to enhance its photodegradation efficiency[63]

2.3 Semiconductors

The common attribute in dye-sensitized solar cell and photodegradation of contaminated water is the use of semiconductor. Semiconductors act as the heart in both systems. The most interesting and prominent semiconductor material used in present time is titanium (IV) oxide (TiO_2) nanoparticles because of its self-cleaning, chemical stability, and photocatalytic property[64] . It is an n-type semiconductor with a conduction band level of -4.2 eV and the valence band is 7.5 eV[65]. It is found in three different crystal forms namely rutile, brookite and widely investigated anatase phase [66], [67]. The brookite phase is not so useful because it is stable only at very low temperatures. The fundamental optical, electrical and thermal properties of Rutile are well known as it is obtained after high-temperature calcination [68]. A type of TiO_2 nanoparticle containing anatase and rutile phase is known as P-25 TiO_2 [69]. This bi-phase semiconductor has shown improved performance in dye-sensitized solar cells because it has special properties like reduced charge recombination, high surface area to volume ratio as compared to other nanostructures [70]. Factors causing setback for TiO_2 include its inactivity in the visible spectral region which makes it compulsory to use a sensitizer and electron-hole recombination at the surface of TiO_2. The following approaches are used to provide a solution to the setback found in TiO_2.

2.3.1 **Coupling wide band gap oxide semiconductors.**

Photoinduced charge carrier recombination is a process in TiO_2 which limits its photodegradation property because fewer charge carriers are available for reacting with the pollutant molecules. In DSSCs, the main loss path is linked with the recombination of the electrolyte with dye created electrons. Previous research studies have reported that incorporating a semiconductor of wider band gap on the surface of TiO_2 can enhance the separation of photogenerated electron and holes. Examples of such semiconductors include zinc oxide (ZnO), aluminium oxide (Al_2O_3), niobium pentoxide (Nb_2O_5) and SiO_2. In a dye-sensitized solar cell, the insulating properties of these oxides are used to create an energy barrier which retards recombination of charge carriers. Zinc oxide (ZnO) is another oxide semiconductor which has competitive performance with TiO_2. It is an II-VI semiconductor with a wide bandgap (~3.37 eV) at room temperature [71]. It has an exciton binding energy of 60 meV which makes it an excellent material for excitonic devices. It has broad chemistry leading to its opportunity for a low threshold for optical pumping, wet chemical etching, and biocompatibility. It has good catalytic, optoelectronic, electrical, and photochemical properties which make it useful in gas sensing, medicine, varistors, photodetectors and light-emitting diodes [72]. It chemical and physical properties depend on its nanostructure morphology. A type of ZnO attracting interest nowadays is the monocrystalline nanorods because it has high electron mobility, energy band edge close to those of TiO_2 and can transport electrons faster than TiO_2 nanoparticle film hence has been a highly favorable material for application in DSSCs. Yet deficiencies associated with it include lower surface area for dye adsorption used in dye-sensitized solar cells [73]–[76]. Furthermore, in the photo-degradation of organic pollutants it is regarded as an important semiconductor such that it is more efficient than TiO_2 in organic compounds photo-oxidation[77] . Since the conduction band level of ZnO is 4.3 eV and the valence band is 7.6 eV showing a bandwidth more than TiO_2, therefore, it is reported that coupling ZnO to TiO_2 can be used to reduce electron-hole recombination in TiO_2 as doing this electron are transferred from conduction band of TiO_2 to that of ZnO and holes generated in the valence band of TiO_2 are trapped in the valence band of ZnO[78]–[80]. Several methods have been used to achieve this modification by a number of researchers. Chun et al. reported a higher catalytic activity and an enhanced use of UV-light from TiO_2-ZnO hybrid nanostructures synthesized using site-specific deposition of TiO_2 on ZnO nanorod [81].

2.3.2 Sensitization with semiconductors

Narrow band gap semiconductors are usually attached to the surface of wide band gap semiconductors in a process known as sensitization to serve as a component for trapping visible light. One of the most promising semiconductor sensitizers among all other narrow band gap semiconductors like CuTe[82], PbSe[83], PbS[84], CdSe[85], InP[86] and

CdS[87]. It has a good photocatalytic performance under visible light and sulfur deficient. It is widely used as a photo-anode in photo-electrochemical cells because it's highly stable, easy to fabricate and has a long lifetime[88]. It undergoes a phenomenon known as photo-corrosion which is the self-oxidation of the photo-generated holes[89]. The composite formed exhibit different band positions such that visible light photon creates electrons in the valence band of CdS which is transferred to the valence band of TiO_2 and the holes are retained in the valence band of CdS. Charge carrier separation is also achieved by anchoring CdS to TiO_2 surface and the photo-corrosion process is suppressed by the presence of TiO_2.

2.3.3 Doping with metals

Doping with metals is known to be the most active approach to shifting the absorption wavelength to the visible spectral region[90]. Among the group of metals in existence, noble metals have been of higher interest[91]. In a noble metal-doped metal oxides, equilibrium occurs between the Fermi levels of the two systems when a more negative potential is acquired by the conduction band of the semiconductor. This readjustment forms a schottky barrier to trap electrons when the energy levels bend to a higher energy [92]. Examples of noble metal that has attracted interest is silver (Ag), gold (Au) and platinum (Pt)[93]. Under illumination, the electrons in the conduction band interact with the oscillating electric field generated by the incident photon. The oscillation is intensified when the frequency of the photon is resonant with the collective vibration of the electrons in the conduction band. The resonance is known as Surface Plasmon Resonance for metal nanoparticles result in a broad and strong band in the visible spectral region which is used to produce visible light active metal doped photocatalysts[94]–[97].

2.3.4 Carbon nanomaterial attachment

The two most interesting carbon nanomaterials are carbon nanotube and graphene because they are both excellent candidates used to gather photo-generated electrons[98]. Carbon nanotube contains multiple layers of graphene from which electron flow through when in contact with oxide semiconductors[94], but graphene is more favorable because it is one atom sp^2-bonded carbon and a two-dimensional nanomaterial with extraordinary properties such as charge carrier mobility, thermal conductivity, mechanical strength and surface area[99]. In order to explore the properties of graphene, it has to be coupled to a semiconductor. TiO_2-graphene composite is one of the widely studied composite attracting attentions for various applications which have shown improved performance in solar cells, lithium-ion batteries and photo-catalysis[100][101]. This composite has been synthesized using several methods[102]–[106]. The work function of graphene and TiO_2 is 4.42eV and 4.2 eV respectively[107]. Hence, the difference in energy levels makes it possible for photogenerated electrons to be transferred from the conduction band of TiO_2 to the graphene sheet. This limits the ability of photogenerated charge carriers to recombine thereby improving charge carrier separation.

2.4 Pulsed Laser Ablation in Liquid

The irradiation of a target with a focused laser beam in a liquid medium creating high temperature at the surface of the target is known as pulsed laser ablation in liquid. The laser ablation of a solid iron target in water was first reported by Patil et al.[108] . Since then, the great potential of the PLAL technique was discovered and it has become one of the emerging techniques used in synthesizing nanostructured semiconductor material. Its advantages include i. preparation of nanocrystals without by-products ii. The product obtained after ablation can be collected in solution and easy to handle. iii. It does not require the use of high vacuum pumps and costly chambers. iv. It is a simple technique used in the synthesis of nanomaterials and it is of low cost compared to synthesis that uses a gas environment[109]. Although few disadvantages in this method include: low control on particle size distribution and structure, the surface chemistry of the nanoparticles is poorly controlled, the pulsed laser setup is expensive. It has been proved a useful technique for the production of impurity-free oxide semiconductors, like TiO_2 [110], CuO [111] , ZnO [112], [113] SnO_2[114], chalcogenides (CdSe) [115] and metal nanoparticles (Ag [116], Au[117], [118], Pt [119], [120], Cu[121]). The proposed mechanism of this technique is that a target is irradiated with a laser to generate high temperature and pressure plasma plume confined in the liquid medium. This is identified by the expanding bubble and shockwave generated. The nanoparticles are nucleated when the expanded plasma is quenched. Hence, the ions and atoms are released to combine to form the nanoparticles. Most of the chemical, physical and mechanical method of synthesizing nanomaterials face challenges such as preparation of chemicals, tedious and multistep methods, a preparation with special solvents, production of by-products high cost of processing and a need of a vacuum medium**.** Researchers have developed an interest in laser ablation in liquid technique because of its great potential in the field of nanotechnology. Hence, in the synthesis of nanocomposites, PLAL is considered to be the best option because two or more nanoparticles suspended in the liquid media is easily ablated into ions of the particles. They recombine during the rapid cooling of the laser plume to form a new catalyst known as nanocomposite catalyst in a decreased particle size corresponding to improved surface area which is desired for improved photocatalytic and photovoltaic performance.

CHAPTER THREE

METHODOLOGY

3.1 Materials

i. TiO_2 nanoparticles

ii. ZnO nanorod

iii. Cadmium acetate dihydrate ($C_4H_6CdO_4.2H_2O$)

iv. Thioacetamide

v. SiC granular material acquired from Saint-Gobain, USA.

vi. Deionized water

vii. Di-tetrabutylammonium cis-bis(isothiocyanate)bis(2,2’-bipyridyl-4,4’-dicarboxylato)ruthenium(II) (N719)

viii. I_2 based electrolyte:10 mL (component: CMI, LiI, I_2, TBP, AN)

ix. Fluorine-doped tin oxide (FTO) glass plate

x. Beaker

xi. Magnetic stirrer

xii. Oven

xiii. Commercial platinized FTO glass

xiv. Plastic dropper

3.2 Nanocatalyst Synthesis

3.2.1 Synthesis of Cadmium Sulfide

In the synthesis of CdS, 1.9 g of Cadmium acetate dihydrate ($C_4H_6CdO_4.2H_2O$) was mixed with 1.0 g thioacetamide (C_2H_5NS) in 50 ml of deionized water and the mixture was stirred continuously to make it uniform and then heated at 60^0C temperature for 2 hours. The yellow mixture, thus obtained was centrifuged for 30 minutes to separate the precipitate. After drying the precipitate for 3 days at 60^0 C, the CdS was obtained in solid form and was grinded to make it in fine powder form.

3.2.2 Synthesis of graphene sheet

The graphene sheets suspended in deionized water collected from an affiliated group but synthesized using the following process. Copper (Cu) foil was cut and heated from room temperature to 1000 ^oC in the presence of Ar and H_2 using chemical vapor deposition (CVD) system (First Nano Co. USA). The graphene was grown by introducing methane (CH_4) for 3 min into the reactor chamber, the total gas flow rate was set to 1500 sccm (Ar: H_2: CH_4= 1458: 37: 5 sccm). Finally, graphene/Cu samples were cooled down to room temperature. The CVD cycle comprised of the following steps: heating, annealing, growth and cooling. Cu foils were then etched away by ammonium persulfate leaving the graphene flakes suspended into the water.

3.2.3 Synthesis of TiO_2/ ZnO binary nanocomposite

The materials used in this work include TiO_2 nanoparticles (<20nm) and ZnO nanorods (NR)(<100 nm). The nanocomposites were synthesized in a stepwise manner. Series of ZnO NR/TiO_2 NP mixture with ZnO NR/TiO_2 NP weight ratio of 9:1, 7:3, 5:5 and 3:7 were prepared. The appropriate amounts of ZnO NR/TiO_2 NP mixture were dispersed in 10 ml of deionized water and sonicated for 30 min. The obtained ZnO NR/TiO_2 NP colloid was placed in pulsed laser ablation setup. The obtained solution after laser ablation was dried in an oven for 60 min to remove the moisture and obtain the nanocomposite in powdered form. The nanocomposite obtained from the mixture prepared with ZnO NR/TiO_2 NP weight ratio of 9:1, 7:3, 5:5 and 3:7 were labelled ZnO/TiO_2@ (9:1), ZnO/TiO_2@ (7:3), ZnO/TiO_2@ (5:5) and ZnO/TiO_2@ (3:7) respectively.

3.2.4 Synthesis of TiO_2-CdS binary nanocomposite

The nanoparticles (TiO_2 and CdS) in powder form were mixed at varied mass ratios in deionised water. The mixture was sonicated and placed in a PLAL setup. The optimization of nanocomposites was done by varying the mass of CdS and keeping the mass of TiO_2 constant. The obtained composite is denoted as T-CdS-k, where k (k = 0,10,20,40) represents the percentage weight of CdS in the nanocomposite.

3.2.5 Synthesis of TiO_2-graphene binary nanohybrid

In each of this solution, 0.1 g of TiO_2 was dissolved and kept for 45 min under magnetic stirring. The graphene suspension-DI water solution volume ratio used in this work include: (0.2:5.8), (1:5) and (3:3) which correspond to graphene percentage concentration of 3 %, 16 %, and 50 % respectively. The solution was then transferred to a pulsed laser ablation setup. The nanohybrid obtained are labeled as G@k-TiO_2, where k = 3 %, 16 %, and 50 %. After etching the Cu, few flakes of graphene were also collected onto the TEM grid (having a carbon film) for transmission electron microscopy (TEM).

3.2.6 Synthesis of TiO_2-SiC binary nanocomposite

Silicon carbide (SiC) used in this work has been reported in our previous work[122]. The SiC was calcined in air at 1200°C such that SiO_2 layer is formed on the surface of the SiC. This was done to prevent further oxidation of SiC[123] when used during the synthesis of the nanocomposite. The nanoparticles (TiO_2 and SiC) in powder form were mixed at varied mass ratios in deionized water. The mixture was sonicated and placed in a PLAL setup. The optimization of the nanocomposite was done by varying the mass of SiC and keeping the mass of TiO_2 constant. The obtained composite is denoted as T-SiC-k, where k (k = 0,10,20,40) represents the percentage weight of SiC in the nanocomposite.

3.2.7 Synthesis of the quaternary nanocomposite.

The Quaternary nanocomposite is first prepared by directly combining the best nanocomposite (ZnO/TiO_2 binary nanocomposite, TiO_2-CdS binary nanocomposite, TiO_2-graphene nanohybrid and TiO_2-SiC nanocomposite) using PLAL technique. In another way, the quaternary nanocomposites are prepared using a computational process written in form of a pseudo code described as follow: The nanoparticle common to all the binary nanocomposite serves as the base nanoparticle in the quaternary nanocomposite. However from the best ZnO/TiO_2 nanocomposite the weight ratio used to divide TiO_2 is determined and used for calculating the amount of ZnO needed, from best TiO_2-CdS binary nanocomposite, the percentage weight of CdS required to couple with TiO_2 is determined and used as the third component and from the best TiO_2-graphene binary nanocomposite, the concentration of graphene required to couple with TiO_2 is determined and used as the fourth component. Hence, a quaternary nanocomposite of ZnO/TiO_2/CdS/graphene is determined. In another fashion, from the optimization process in the TiO_2-SiC binary nanocomposite, the percentage weight of SiC required to couple with TiO_2 is determined and this is used to replace the fourth component in order to form a ZnO/TiO_2/CdS/SiC quaternary nanocomposite. The process is further described with a pseudo code after which the best binary nanocomposite has been determined from the varied combination of ZnO/TiO_2 binary nanocomposite, TiO_2-CdS binary nanocomposite, TiO_2-graphene binary nanohybrid and TiO_2-SiC binary nanocomposite

Hence, the Pseudo code obtained will be written in the following format.

Step 1: Choose a semiconductor common to the synthesized binary nanocomposites with the best performance in the photovoltaic application (DSSC).

Step 2: Compute

- Q(B) = Q(A)/x
- Q(C) = Q(B)/y
- Q(D) = Q(B)/z

Therefore the quaternary composite is denoted as Q (A) - Q (B)/ Q(C)/ Q (D)

Q (A) = common oxide semiconductor,

Q (B) = the other oxide semiconductor present,

Q(C) = narrow band gap semiconductor

Q (D) = carbon based catalyst

X= percentage weight of the dependent oxide semiconductor

Y=percentage weight of the chalcogenide

Z= percentage weight of carbon based material.

3.2.8 Pulsed Laser Ablation in Liquid Experiment

The Nd-YAG laser (532 nm wavelength) used in the synthesis process is kept at the laser energy of 350 mJ/pulse with laser pulse duration of 6 ns and repetition rate of 10 Hz. After the ablation, the resulting precipitates were collected by centrifugation. The laser ablation setup is shown in figure 3.1. The Laser produces an intense unidirectional beam of light. The triangular prism is used to direct the laser beam to the nanoparticle mixture placed at the bottom of the setup. The laser beam is focused on the samples using a convex lens and the mixture is kept under stirring using a magnetic stirrer to obtain uniform ablation.

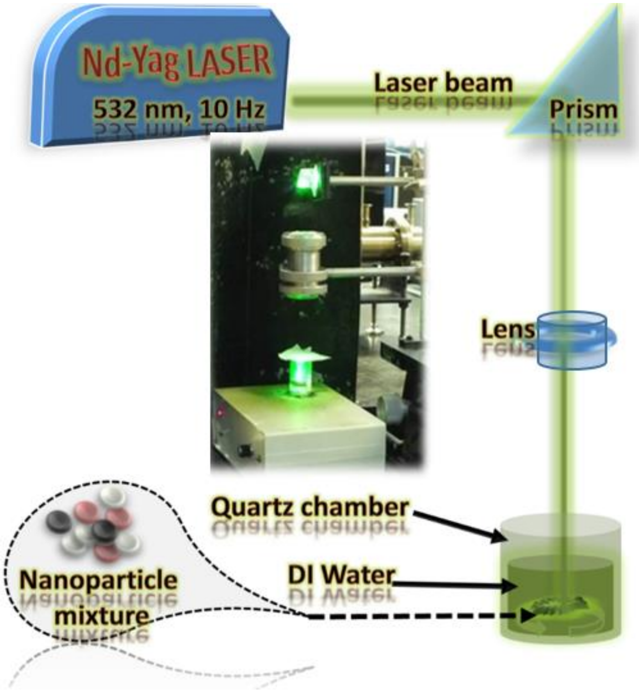

Figure 3.1 Pulsed Laser Ablation Setup

3.3 Photo-degradation of methyl orange (MO) dye

Photocatalytic activities of synthesized nanocomposite/nanohybrid were evaluated as follows. The photodegradation of methyl orange (MO) was conducted under a 500 W Xenon lamp (Oriel, USA). In a typical photodegradation experiment, a 0.05 g of photocatalyst was mixed with 100 ml of MO solution. In order to ensure adsorption equilibrium between the nanocomposite and MO, the suspension was kept under stirring in the dark for 30 min. The mixture was further exposed to UV- Vis light. The suspension was collected and centrifuged (4000 rpm, 2 min) to remove the photo-catalyst particles at regular time intervals of 12 min. The degradation of MO was determined at 460 nm by UV-Vis spectroscopy.

3.4 Solar Cell Fabrication

The nanocomposite solution with a mass concentration of 3g/dm^3 was prepared in ethylene glycol. The solution was sonicated and then drop cast on an FTO glass substrate placed in an oven at ~70 °C. The thin film was further annealed at ~450 °C for 30 min. As shown in figure 3.2 (a).The obtained thin film cooled to ~100 °C was immersed for 10 minutes in 0.27 mM of the N719 dye prepared in ethanol solution (1). The 0.25 cm^2 area thin film with dye molecules adsorbed to its surface is bonded with a commercial Pt coated counter electrode. The internal space of the cell was filled with the I_2 based electrolyte (2). In (3) the picture of the fabricated DSSC is shown. The whole fabrication process is shown in figure 3.2(b).

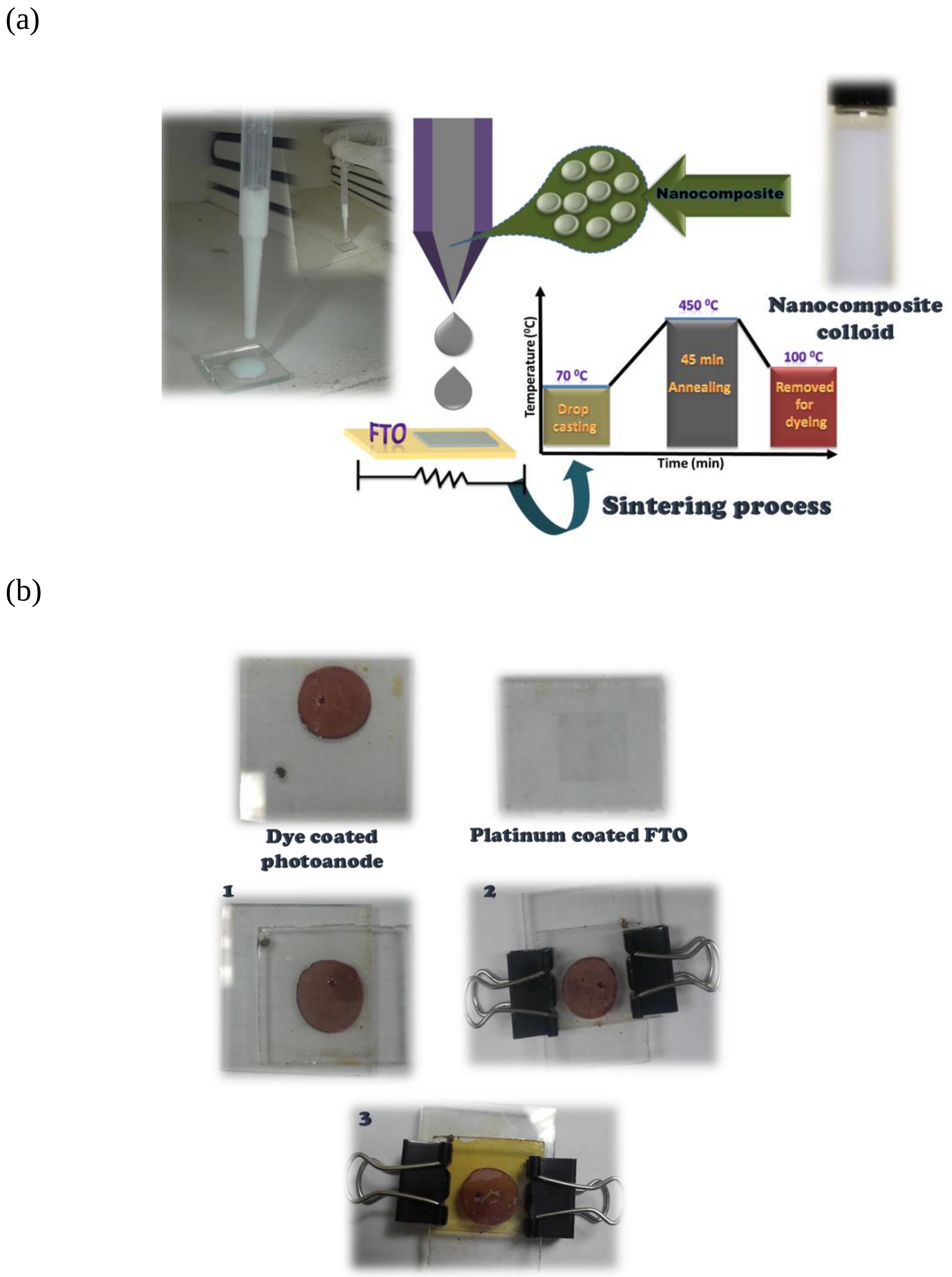

Figure 3.2 (a) Thin film Production (b). Dye-sensitized solar cell fabrication steps

3.5 Characterization

3.5.1 Optical Characterization

i. The UV-vis. absorption spectra of synthesized nanocomposite were recorded on Jasco 670 double beam spectrophotometer.

ii. Fluorolog FL3-iHR, HORIBA Jobin Yvon using Xenon lamp light source with 350 nm excitation wavelength was used to obtain the photoluminescence (PL) property.

iii. FTIR spectra were acquired on a Nicolet 6700 FT-IR spectrometer (Thermo Electron Corp.) The samples were prepared for FTIR studies by mixing 0.5 mg of each of the samples with 98 mg of dry KBr homogeneously to make pellets of 6.95 mm diameter and 0.44 mm thick.

iv. In-situ Raman analysis was done using Yvon Jobin Horiba Raman spectrometer (iHr320) with CCD detector and green type (532 nm) laser source.

3.5.2 Structural characterization

X-ray diffraction (XRD) is one of the primary techniques used to determine physicochemical make-up of crystalline solids. It can be used for determination of crystal structure, crystallinity, compounds identification, crystallite size measurement, and Residual stress measurement. It advantages include its non-destructive analysis of materials. During XRD analysis, x-rays of known wavelength irradiate the sample and gets diffracted at certain angles (θ). Hence the inter-atomic spacing (d-spacing) is calculated from the formula: $n\lambda=2d\sin\theta$. Each crystalline material has a unique XRD pattern is used as a signature for its recognition. Compounds are identified by comparing spectra or data stored in the computer database. The crystallization of the as-prepared nanocomposite was investigated using X-ray diffraction (XRD, Bruker advance-D8 diffractometer) with Cu-Kα radiation

3.5.3 Morphological characterization

i. Field Emission Scanning Electron Microscope (FESEM)

The scanning electron microscope (SEM) is a tool used for materials characterization with the aim to obtain information about the structure, composition and defects in materials. The images are obtained by scanning an electron beam of high energy on the sample surface, thus the name scanning electron microscope. During SEM analysis, signals are generated from the surface of solid specimens by focusing high-energy electron beam on the sample. These signals reveal the morphology, orientation, and composition of the materials. Data are usually collected over a selected area and in a 2-dimensional generated display. Selected point locations can also be analyzed; especially when chemical composition and crystal orientation is being investigated. A conventional SEM can measure areas in the range of 1 cm to 5 microns in width with magnification ranging from 20x to ~30000x, but a field emission scanning electron microscope can additionally provide elemental and topographical information at a magnification of up to 10^6 x. FESEM produce a clearer and less distorted image.

The morphology of the samples was obtained using Lyra TESCAN Field emission electron microscope (FE-SEM) equipped with an energy-dispersive X-ray spectrometer

ii. Transmission Electron Microscope (TEM)

The transmission electron microscopy (TEM) is a process whereby highly accelerated electrons transmit through a sample of nanometer thickness while interacting with the sample to form an image known as a TEM image which is focused on a fluorescent screen.

Image contrast occurs when the electrons are absorbed by the sample at small magnification and this is determined by specimen thickness and elemental composition. The sample size is limited to a disc-shaped sample holder of 3 mm size. A phase contrast imaging technique used to obtain atomic resolution images is known as the high-resolution transmission electron image (HRTEM). It can be used to identify defects, crystal phases, lattice plane and crystallinity of the sample. Crystallographic information of selected regions of the sample from micron to 100 nm scale is provided using the selected area electron diffraction (SAED). The orientation and spacing of the diffraction spots are interpreted as the planar spacing and orientations in the sample.

FEI Titan 80-300 CT TEM instrument was employed to obtain the Transmission electron microscope (TEM) image, High-resolution TEM (HRTEM) and selected area electron diffraction (SAED) of the synthesized composite

3.5.4 X-ray Photoelectron Spectroscopy (XPS)

X-ray Photoelectron Spectroscopy (XPS) is a surface analysis technique applicable to a broad range of materials. It provides chemical state and quantitative information from an average depth of ~5nm of the material studied. The surface of the sample is excited with mono-energetic x-rays which eject photoelectrons and their kinetic energy is measured by an electron energy analyzer. The intensity and binding energy of the photoelectron are used to determine the chemical state and elemental identity of the elements at the surface of the sample.

X-ray photoelectron spectroscopy (XPS) experiments was carried out using ESCALAB-250Xi System (Thermos-Scientific) with Al Kα radiation ($h\nu$=1486.6 eV).

3.5.5 Dye-sensitized Solar Cell Characterization

The determination of the DC current-voltage curves under incident light intensity is the standard technique of determining the performance of a PV device. In a metrohm Auto lab PGSTAT302N, a potential scan is applied from 0 V to the open circuit potential under constant light intensity in order to obtain the photocurrent-voltage measurement (IV curves). The IV curve gives the following parameters:

i. Short circuit current (I_{SC}) The current measured at an applied potential of 0 V

ii. Open circuit voltage (V_{OC}): the potential of the cell measured when at 0 A current

iii. Fill factor (FF): the ratio of the maximum power to the open and short circuit values. Both the I_{SC} and V_{OC} depend on the light intensity according to the Schottky equation. Although there is a logarithmical increase in the open circuit voltage according to the distribution of the energy states in the semiconductor

The Autolab PGSTAT302N in combination with 500 W Xenon Lamp (Oriel, USA) equipped with a visible light filter was used to characterize the solar cell. The obtained parameters such as the open circuit voltage and short circuit current were used in calculating the fill factor and efficiency of the solar cell [124], [125].

$$Efficiency\ \eta = \frac{J_{sc} \times V_{oc} \times FF}{I} \times 100\ \% \quad [18] \tag{1}$$

where $$FF = \frac{J_m \times V_m}{J_{sc} \times V_{oc}} \quad [2]$$

Where, V_m is the maximum voltage, J_m is the maximum current density, I incident light intensity, J_{SC} is the short-circuit current density under irradiation

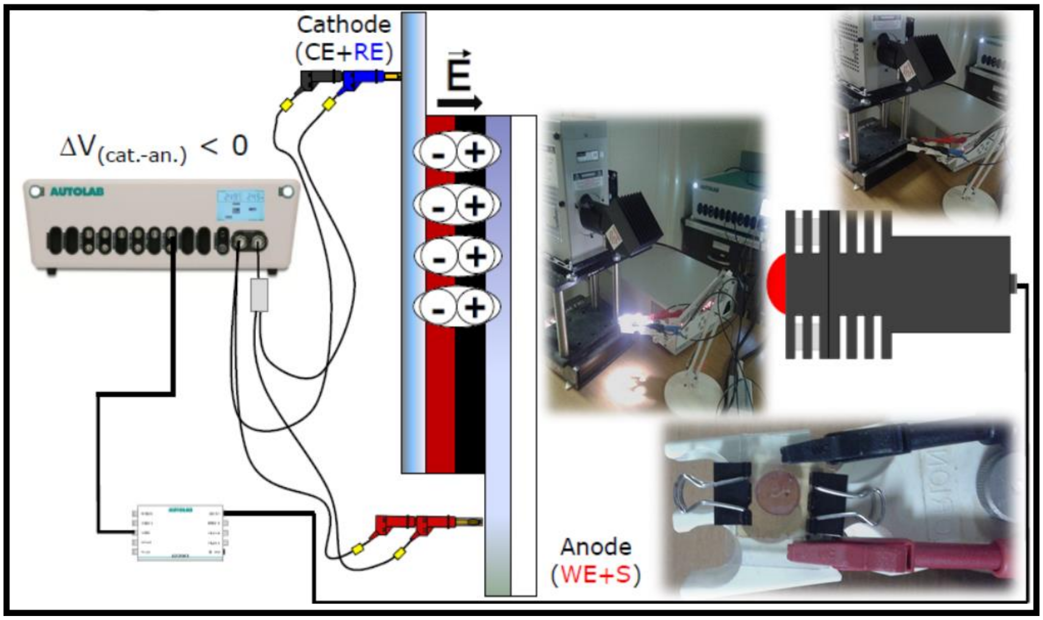

Figure 3.3 Metrohm Auto lab PGSTAT302N setup used for measuring the DSSC parameters

The internal dynamics of the PV device cannot be understood using the DC technique. Therefore, frequency-dependent measurement need to be done to obtain additional information about the device. In particular, electrochemical impedance spectroscopy (EIS) offers the possibility to investigate the dynamics of the device in the frequency domain at constant light intensity under operating conditions. It studies how the impedance of the device varies with the frequency of a small-amplitude AC perturbation. In practice, a function of frequency which is a complex quantity is obtained from the conversion of the input and output signals time domain. These input and output signals are software and hardware processed to yield a transfer function that is frequency dependent. The Nyquist plot is one of the most often used data plots in EIS. The EIS measurement was done under illumination at open circuit voltage and all the measurements were carried out with NOVA software.

CHAPTER FOUR

RESULT AND DISCUSSIONS

4.1 ZnO/TiO_2 nanocomposite

4.1.1 Optical analysis of ZnO/TiO_2 nanocomposite

The semiconductor materials generate photoluminescence from the recombination of the photogenerated electron-hole pair. The transfer, migration and trapping of charge carriers in a semiconductor are determined using PL measurement. ZnO is known to be a defect prone semiconductor. The luminescence of ZnO which appears in the visible spectral region (400-700 nm) is due to oxygen vacancy, oxygen interstitial, zinc interstitial, and zinc vacancy created in ZnO lattice[126][127]. The weak luminescence in the UV -region is due to radiative band to band recombination of excitons[128]. Hence, coupling TiO_2 with ZnO lattice should have a positive or negative effect on its luminescence in the UV-Vis region. These emissions can be used to monitor the charge transfer interaction in the ZnO/TiO_2 nanocomposite. The photoluminescence spectra of TiO_2, ZnO, and synthesized ZnO/TiO_2 nanocomposite were recorded and are depicted in figure 4.1. This shows both the ZnO and ZnO/TiO_2 nanocomposite has the emission in the UV and visible regions. The weak emission at UV-region is magnified and shown in figure 4.1 (b). This shows that compared to ZnO NR whose peak is centered at 387 nm, there is a blue shift to a position at 377 nm for all the synthesized nanocomposite which can be the effect of extra TiO_2 band in ZnO. Since TiO_2 has no emission in the visible region. Figure 4.1 (c) shows magnified broad visible peak for ZnO and the nanocomposite. In this figure, ZnO, ZnO/TiO_2@(3:7), ZnO/TiO_2@(5:5) and ZnO/TiO_2@(7:3) exhibits an emission peak centered at around 485 nm which is an indication of the violet-blue luminescence. This emission is due to radiative defect linked with zinc vacancy in ZnO[129]. Hence, the synthesized nanocomposite experiences a lesser emission as compared with the pure ZnO. This shows that there is a fine interfacial interaction between the nanoparticles of two catalysts [130] and the radiative defect was clearly reduced in the nanocomposite.

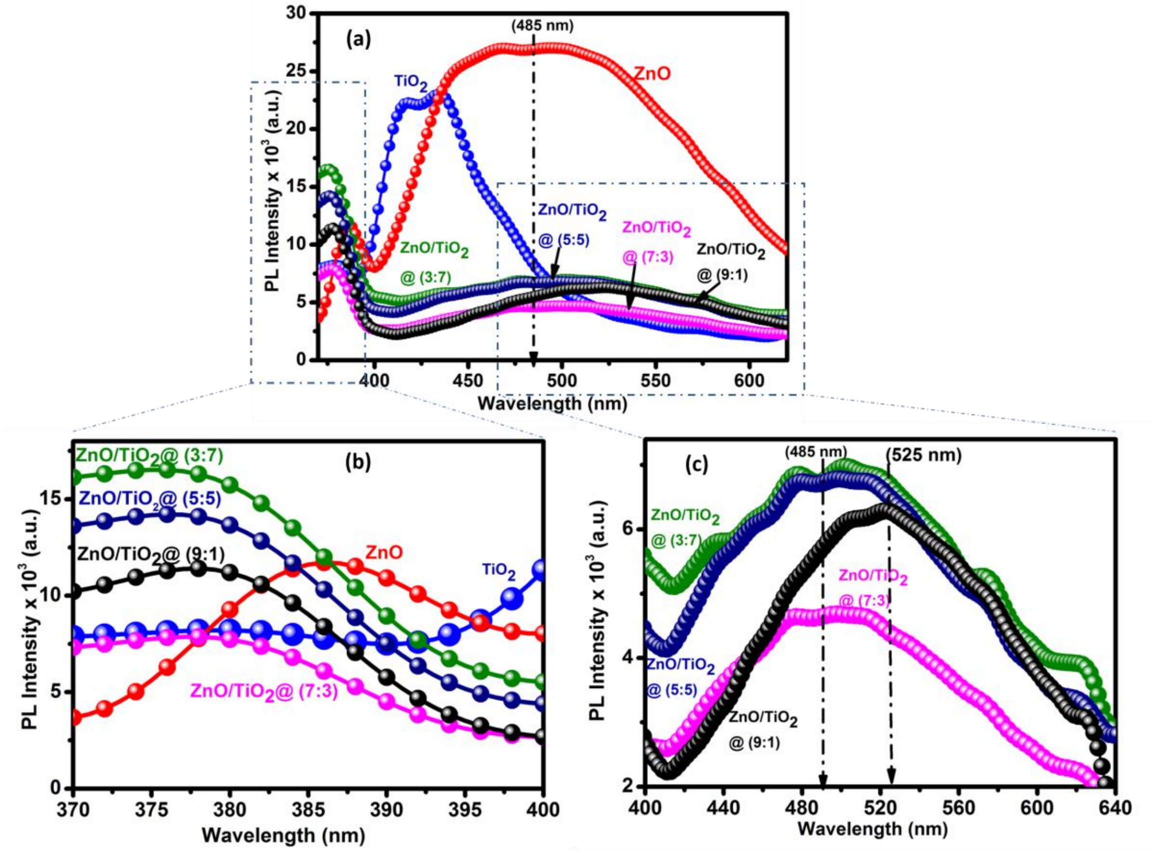

Figure 4.1 (a) Photoluminescence spectra of TiO_2, ZnO, ZnO/TiO_2@(3:7) ZnO/TiO_2@(5:5), ZnO/TiO_2@(7:3) and ZnO/TiO_2@(9:1).(b) high magnification of the small peak in the UV region (c) high magnification of the broad luminescence peak of the nanocomposite in the Vis spectral region.

As it is clear from figure 4.1(b), PL emission intensity decreases with increase in TiO_2 concentration, suggesting a reduction of radiative defect as the concentration of zinc oxide reduces. Another observation is that compared to ZnO, ZnO/TiO_2@(3:7), ZnO/TiO_2@(5:5) and ZnO/TiO_2@(7:3), a red shift occurs for ZnO/TiO_2@(9:1) whose peak is centered at ~525 nm at orange-red in the visible region. This shows that ZnO/TiO_2@ (9:1) has some oxygen vacancy defect in its colloid[127], [129]. Since deep energy levels are created by defects in the band gap of ZnO[129], it is reported that [114] zinc vacancy creates an acceptor level but oxygen vacancy created in ZnO/TiO$_2$@ (9:1) provides a donor level which would allow it to trap charge carriers, therefore, reducing the electron-hole pair recombination as compared with another nanocomposite.

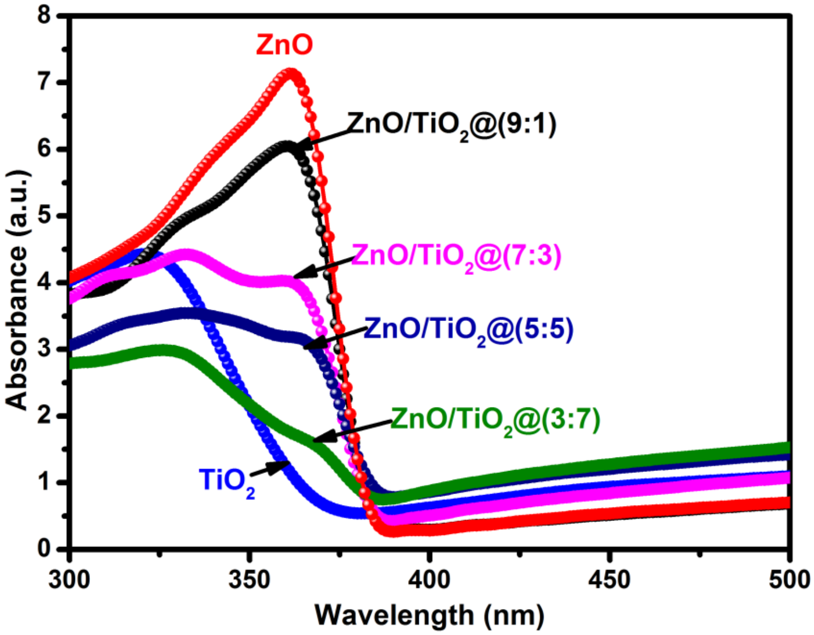

Figure 4.2 Absorbance spectra of TiO$_2$, ZnO/TiO$_2$@(3:7), ZnO/TiO$_2$@(5:5), ZnO/TiO$_2$@(7:3), ZnO/TiO$_2$@(9:1) and ZnO.

The UV-Vis absorption spectra of TiO$_2$ NPs, ZnO NR, and synthesized ZnO/TiO$_2$ nanocomposite are depicted in figure 4.2. The TiO$_2$ dominant nanocomposite (ZnO/TiO$_2$@ (3:7)) has a strong absorption edge similar to that of TiO$_2$ with weak absorption in the deep UV-region because of the small concentration of ZnO in the composite. ZnO and ZnO dominant nanocomposite (ZnO/TiO$_2$@(9:1), ZnO/TiO$_2$@(7:3) and ZnO/TiO$_2$@(5:5) have strong absorption over a wide range of the UV–region extending to the absorption edge of 385 nm which correspond to a band gap energy of 3.22 eV[131].

4.1.2 Structural analysis of ZnO/TiO_2 nanocomposite

Figure 4.3 shows the XRD patterns of the TiO_2, ZnO and the synthesized ZnO/TiO_2 nanocomposite. Some major and minor peaks of wurtzite-type hexagonal-phase ZnO with lattice parameters a = 3.252 Å and c = 5.208 Å (JCPDS card, No. 36-1451) [132] were present in all the produced nanocomposite. In addition, Zinc titanium oxide (ZnTiO) major and minor peaks were matched with some of the peaks that appear in the XRD spectra of the nanocomposite according to the DB card No. 00-049-0687 which explains transformation has occurred in their crystal structure as a result of laser ablation of titanium dioxide and zinc oxide.

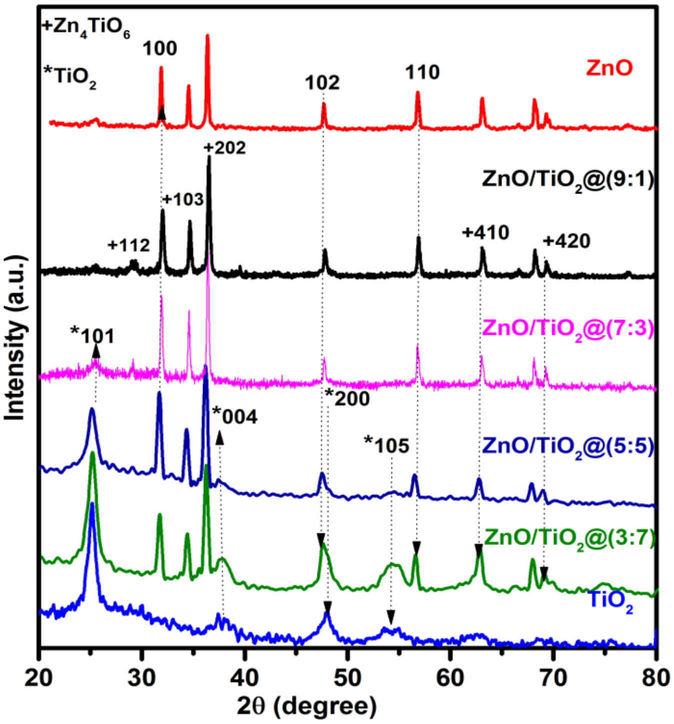

Figure 4.3 XRD pattern of TiO_2, ZnO, ZnO/TiO_2@ (3:7), ZnO/TiO_2@ (5:5), ZnO/TiO_2@ (7:3) and ZnO/TiO_2@ (9:1).

The presence of anatase type TiO_2 (JCPDS 211272) [133] [131], [134], [135]with *a* = 3.7852 Å is clearly observed in the commercial TiO_2 used for the synthesis of the nanocomposite. The (101) major peak of anatase phase TiO_2 is seen in nanocomposites such as ZnO/TiO_2@(7:3), ZnO/TiO_2@(5:5) and ZnO/TiO_2@(3:7). The intensity of the (101) major peak reduces as the concentration of TiO_2 reduces in the order: ZnO/TiO_2@(3:7)>ZnO/TiO_2@(5:5)>ZnO/TiO_2@(7:3) > ZnO/TiO_2@(9:1). This (101) plane almost completely disappears in ZnO/TiO_2@ (9:1) nanocomposite. A small peak at 2θ =29.2^0 indexed to (112) plane of ZnTiO is found in only (ZnO/TiO_2@(7:3) and ZnO/TiO_2@(9:1)) nanocomposites. Also observed is that the nanocomposites has a broader peak than ZnO. In addition, the (102) plane of ZnO overlaps with the (200) plane of TiO_2. This serve as a proof that a perfect interaction occur within the lattice of TiO_2 and ZnO in the produced ZnO/TiO_2 nanocomposite.

4.1.3 Raman spectra analysis of ZnO/TiO_2 composites

The Raman spectra of TiO_2, ZnO, and synthesized ZnO/TiO_2 composites are depicted in figure 4.4 In ZnO, the highest and most significant peak is observed at 435 cm^{-1} which imply, ZnO has wurtzite structure and highly crystalline. This peak is attributed to E_{high2} mode of hexagonal ZnO and it is due to vibration of oxygen atom in ZnO lattice [136]. In $TiO_{2,}$ the Raman peak at 133.5 cm^{-1}(E_g), 393 cm^{-1}(B_{1g}) and 513 cm^{-1}(A_{1g}) band are associated with bending mode of O-Ti-O bond, oxygen atom liberation along the c-axis out of phase and Ti-O stretching mode respectively which confirms the presence of anatase phase[137], [138]. In the synthesized ZnO/TiO_2 nanocomposite, the obtained typical Raman spectra show characteristic Raman peaks almost similar to that of TiO_2 because the Raman scattering of TiO_2 is more than ZnO scattering at the excitation wavelength. Hence, it is evident that the synthesized ZnO/TiO_2 nanocomposite has anatase phase according to Raman spectra. The Eg mode of synthesized nanocomposite at 133.5 cm^{-1} shifts towards higher wavenumbers (red shift) as shown in figure 4.4 (b), this demonstrates that: higher content of oxygen vacancies are present in the nanocomposite than TiO_2. In ZnO dominant composites (ZnO/TiO_2@(9:1) and ZnO/TiO_2@(7:3)), a B_{1g} band of TiO_2 centered at 393 cm^{-1} was broadened because it overlaps with the 435 cm^{-1} optical phonons of ZnO as shown in figure 4.4(c). The overlap of the two bands explains that interaction sets in between the two crystals when the laser beam sets there oxygen atoms into vibration.

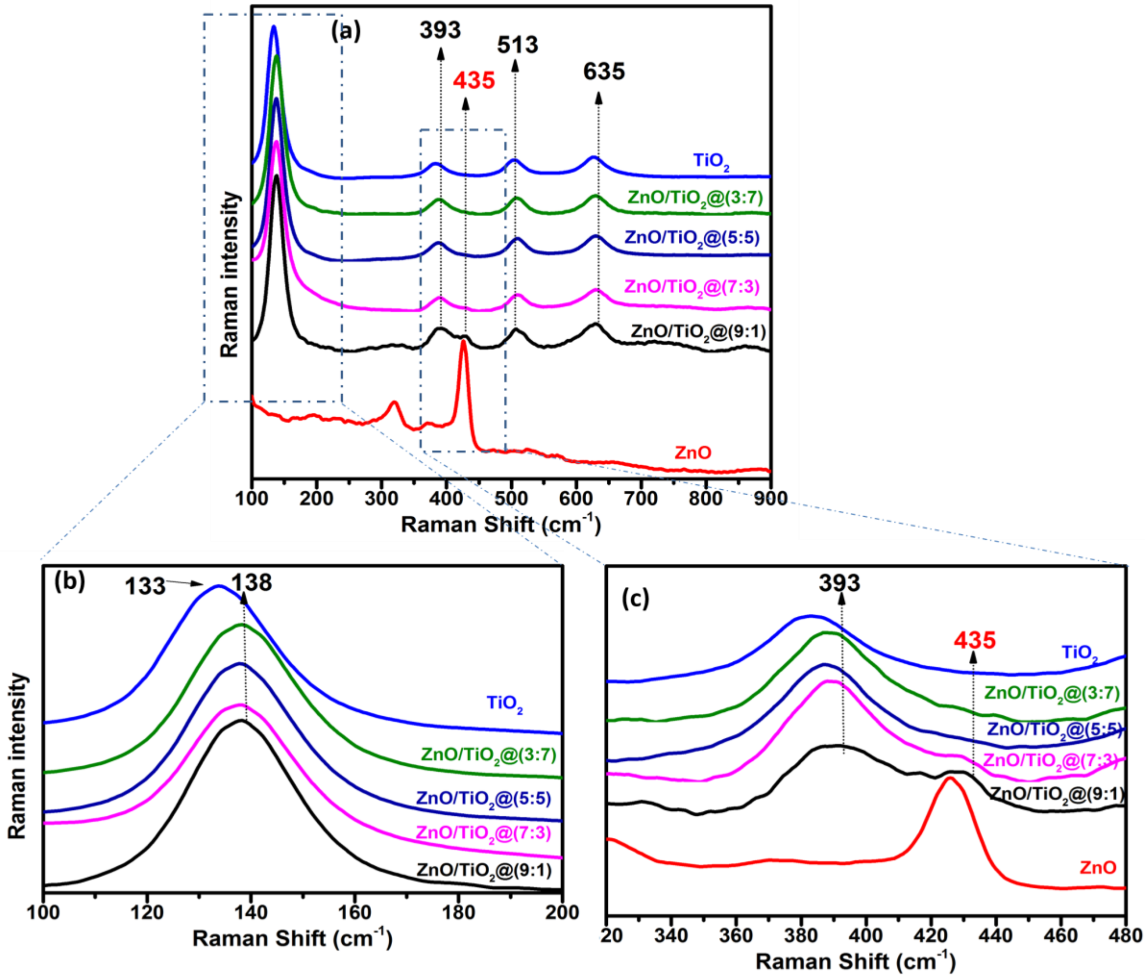

Figure 4.4 (a) Raman spectra of ZnO, TiO_2, ZnO/TiO_2@ (3:7), ZnO/TiO_2@ (5:5), ZnO/TiO_2@(7:3) and ZnO/TiO_2@(9:1) (b) Higher magnification of peak X in the Raman Spectra(c) Higher magnification of $TiO_2$and ZnO peak overlap in the Raman Spectra.

4.1.4 Morphology of ZnO/TiO_2 nanocomposite

The morphology of the best nanocomposite ZnO/TiO_2@ (9:1) was observed with the scanning electron microscopy (SEM) image. It is depicted in figure 4.5. This shows the ZnO matrix is completely decorated with spherical particles of TiO_2. It was also observed that the TiO_2 and ZnO nanorods were integrated into each other in a perfect fashion. This perfect coalition makes it easy for charge carriers to transfer across the interfaces

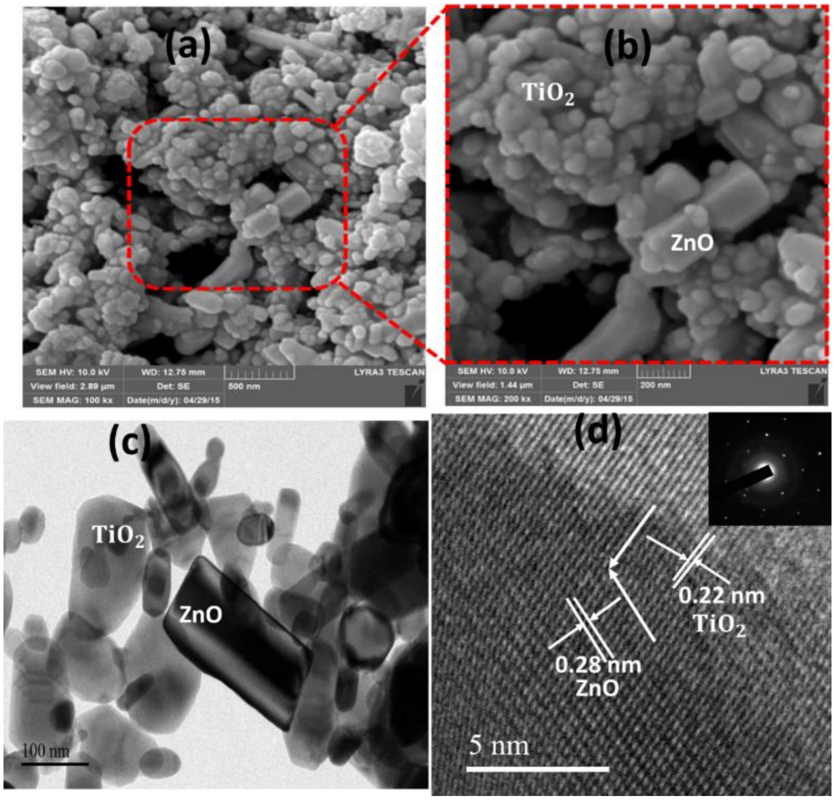

Figure 4.5(a) FE-SEM Image of ZnO/TiO_2@ (9:1) nanocomposite (b) high magnification of ZnO/TiO_2@ (9:1) nanocomposite (c) A typical TEM image of ZnO/TiO_2@ (9:1) nanocomposite (d) HRTEM of ZnO/TiO_2@ (9:1) nanocomposite(inset :SAED of ZnO/TiO_2@ (9:1) nanocomposite)

Figure 4.6(c) shows the low magnification TEM image of the ZnO/TiO_2@9:1 nanocomposite. The ZnO NR and the spherical TiO_2 have an average size of 50 nm and 10 nm respectively. In the inset of figure. 4.5 (c). The selected area electron diffraction

(SAED) image shows diffraction spots of ZnO dominant and it confirms the crystalline nature of the nanocomposite. The high-resolution TEM (HRTEM) image in fig. 4.5(d) taken from the core-shell ZnO/TiO2@9:1 shows lattice fringes having d-spacing of 0.22 nm and 0.28 nm belonging to TiO_2 and wurtzite-type hexagonal ZnO at the interface portion.

4.1.5 XPS analysis of ZnO/TiO_2 nanocomposite

The XPS analysis was carried out to investigate valence states of the elements and the chemical composition of the best composite (ZnO/TiO_2@ (9:1)). Figure 4.6 shows a typical survey scan for ZnO/TiO_2@ (9:1) over a large range at low resolution. This figure shows that ZnO/TiO_2@ (9:1) contains Zinc, Oxygen, and Titanium indicating the presence of TiO_2 and ZnO nanoparticles.

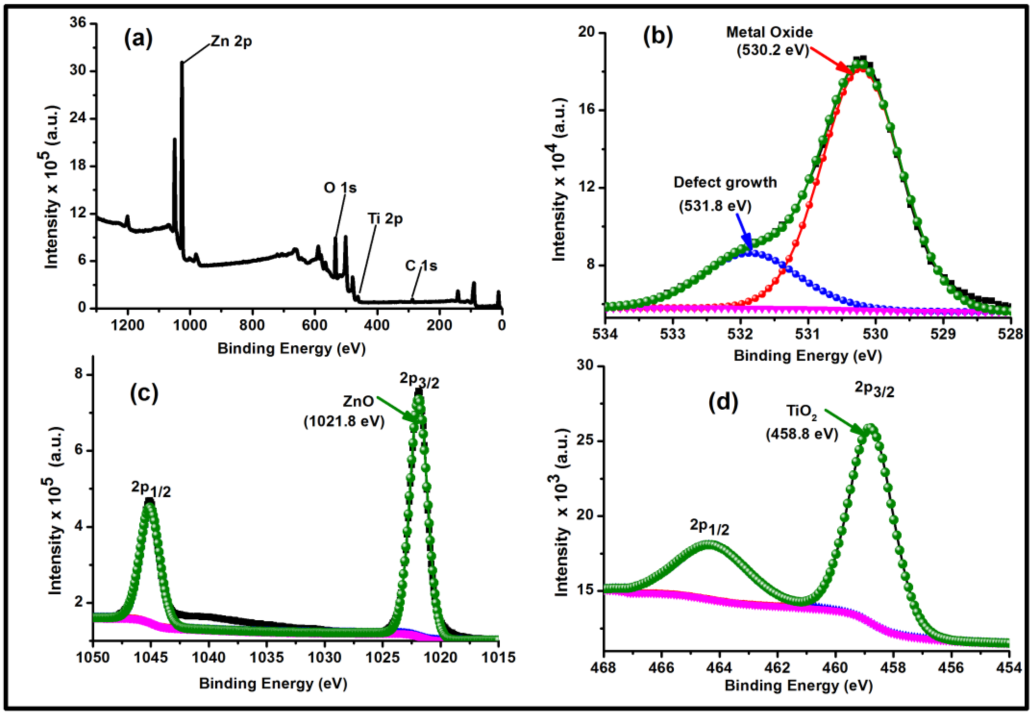

Figure 4.6 XPS Analysis of ZnO/TiO_2@ (9:1) nanocomposite

The high-resolution scan of Ti 2p, O1s, and Zn2p states are given in figure 4.6(b-d) with spin-orbit splitting observed at Ti 2p and Zn 2p states. The O1s peak in figure 4.6 (b) was deconvoluted into peaks located at 530.2 eV and 531.8 eV which is assigned to metal oxides (O-Ti bond and Zn = O bond) [139]–[141] and oxygen associated with the growth of defect[142]. Zn $2p_{3/2}$ of the spin-orbit split peak of Zn shown in figure 4.6 (c) was fitted into a peak at 1021.8 eV associated with Zn^{2+} bonds in ZnO [143], [144]. The Ti $2p_{3/2}$ peak in figure 4.6 (d) was fitted into a single peak with a position at 458.7 eV corresponding to the presence of Ti^{4+} bond of TiO_2 in the nanocomposite [145].

4.1.6 Photovoltaic performance analysis

The current density (J)-voltage (V) curve of the DSSC fabricated with the nanocomposite-based photoanode is depicted in figure 4.7. The short-circuit current density (Jsc) and open circuit voltage (Voc) obtained from the J-V curve of the DSSC is used to calculate the efficiency and fill factor of the solar cell. The difference between the redox potential of the electrolyte and the Fermi level of an electron in the nanocomposite photoanode is proportional to the Voc [146]. The ZnO/TiO_2@ (9:1) nanocomposite shows highest Voc of 0.5027 V and the ZnO/TiO_2@ (5:5) nanocomposite has the least Voc of 0.2884 V**.** The highest Jsc was also observed in the ZnO/TiO_2@ (9:1) and ZnO/TiO_2@ (3:7) nanocomposite has the least Jsc value. It was observed that the Jsc value decreases as the concentration of TiO_2 increases. All the nanocomposite has a Voc value higher than that of $TiO_{2,}$ but only ZnO/TiO_2@ (9:1) has Voc higher than ZnO. The obtained photoconversion efficiency of the DSSC varies with the weight ratio of the nanocomposite photoanode. The efficiency obtained from the DSSC synthesized with the nanocomposite decreases with increase in the amount of TiO_2 and decrease in ZnO. The highest power conversion efficiency, 6.70 % was achieved from ZnO/TiO_2@ (9:1) nanocomposite with Jsc of 2.02 mA, Voc of 0.50 V and FF of 0.53. The least efficiency, 0.30 % was observed in ZnO/TiO_2@ (3:7) nanocomposite with Jsc of 0.196 mA, Voc of 0.35 V and FF of 0.35.

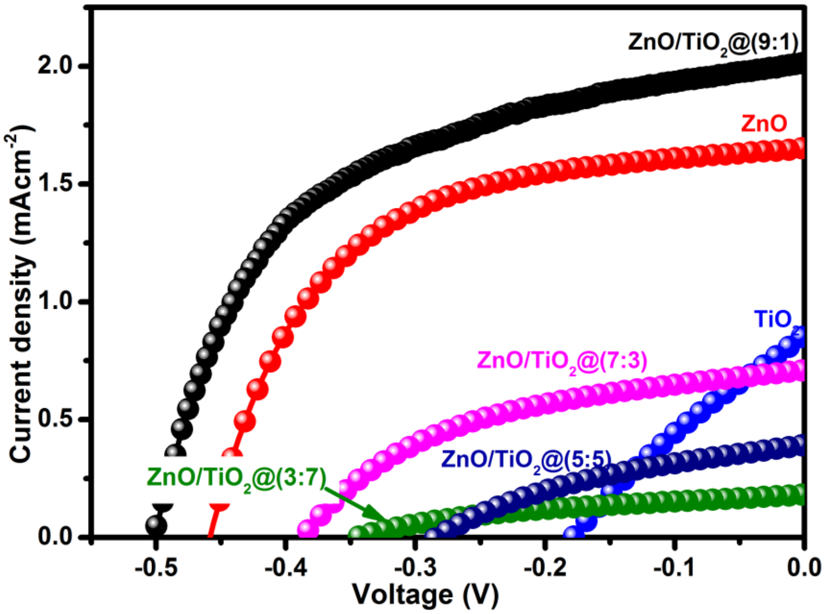

Figure 4.7 J-V curve of DSSC with ZnO/TiO_2@(9:1), TiO_2, ZnO, ZnO/TiO_2@(7:3), ZnO/TiO_2@(5:5) and ZnO/TiO_2@(3:7) nanocomposites

The efficiency is in the order: ZnO/TiO_2@ (9:1)> ZnO/TiO_2@ (7:3)> ZnO/TiO_2@ (5:5)> ZnO/TiO_2@ (3:7) as shown in Table 4.1. ZnO shows the highest efficiency out of the two single element nanoparticles. The efficiency of ZnO/TiO_2@ (9:1) and ZnO/TiO_2@ (7:3) DSSC is increased by 12 and 3 times respectively as compared with the pure TiO_2. The efficiency of pure ZnO was improved by 63.73 % in ZnO/TiO_2@ (9:1) DSSC.

Efficiency decrease was observed in DSSC made from ZnO/TiO_2@ (5:5) and ZnO/TiO_2@ (3:7) with respect to TiO_2 DSSC. With respect to ZnO NR there is a 60.78 %, 87.25 % and 92.16 % decrease in ZnO/TiO_2@ (7:3), ZnO/TiO_2@ (5:5) and ZnO/TiO_2@ (3:7) DSSC respectively. This can be due to band misalignment in the nanocomposites. In order to understand the J-V performance of DSSCs fabricated from the synthesized nanocomposites, the electrochemical impedance spectroscopy (EIS) measurements were carried out to understand the interfacial charge transfer dynamics within the DSSCs.

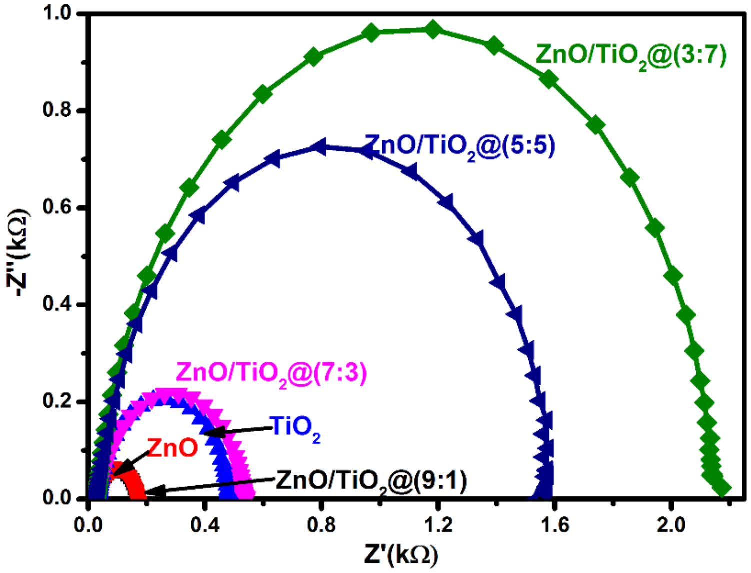

Figure 4.8 Nyquist plot of DSSC with ZnO/TiO_2@(9:1), TiO_2, ZnO, ZnO/TiO_2@(7:3) ZnO/TiO_2@(5:5) and ZnO/TiO_2@(3:7) nanocomposites

Table 4.1 J-V characteristics of the DSSCs with TiO_2, ZnO, ZnO/TiO_2 @ (3:7), ZnO/TiO_2 @ (5:5), ZnO/TiO_2 @ (7:3) and ZnO/TiO_2 @ (9:1) nanocomposite.

	Isc (mA/cm^2)	Voc (V)	FF (%)	η (%)	Rct (kΩ)
TiO_2	**0.852**	**0.1787**	**29.32**	**0.56**	**0.48**
ZnO	**1.643**	**0.4612**	**56.60**	**5.36**	**0.18**
ZnO/TiO_2@(9:1)	**2.015**	**0.5027**	**52.90**	**6.70**	**0.16**
ZnO/TiO_2@(7:3)	**0.702**	**0.3875**	**46.70**	**1.59**	**0.52**
ZnO/TiO_2@(5:5)	**0.384**	**0.2884**	**36.78**	**0.51**	**1.55**
ZnO/TiO_2@(3:7)	**0.196**	**0.3495**	**35.37**	**0.30**	**2.13**

The Nyquist plot of the DSSCs based on the nanocomposites photoanode is shown in figure 4.8. The second semi-cycle shows the difference in the charge transfer resistance (Rct) at the photoanode/dye/electrolyte interface [147]. It was observed that as the concentration of TiO_2 increases as the electron transfer resistance increases. ZnO/TiO_2@ (3:7) has the highest resistance of 2.13 kΩ while ZnO/TiO_2@ (9:1) nanocomposite has the least transfer resistance (0.16 kΩ). This explains one reason why it has the highest efficiency. The almost identical Rct value between ZnO/TiO_2@(9:1) and ZnO clearly explains the enhanced performance of ZnO/TiO_2@(9:1) is not only due to reduction in transfer resistance but other properties like increase in surface area associated with TiO_2 surface attachment.

4.1.7 Photocatalytic performance analysis

The difference in the photodegradation capability of the synthesized nanocomposite was investigated by examining the decomposition of Methyl Orange (MO) dye in solution over ZnO/TiO_2@(9:1), ZnO/TiO_2@(7:3), ZnO/TiO_2@(5:5), and ZnO/TiO_2@(3:7) nanocomposite under full solar spectrum (UV and Vis) light irradiation. The result is shown in figure 4.9. The MO dye was exposed to the full solar spectrum without the catalyst and with the catalyst in a dark environment in order to show that the decomposition is neither by catalysis nor photolysis. This is confirmed by the nearly unchanged concentration of MO dye over the 60 mins irradiation period as shown in figure 4.9. It can be observed that: at 36 min the activity decreases in the order ZnO/TiO_2@(9:1) > ZnO/TiO_2@(5:5) > ZnO/TiO_2@(7:3)>ZnO/TiO_2@(3:7). All the nanocomposite catalysts are more active than $TiO_{2,}$ but only ZnO/TiO_2@ (5:5) and ZnO/TiO_2@ (9:1) nanocomposite have better activity than ZnO.

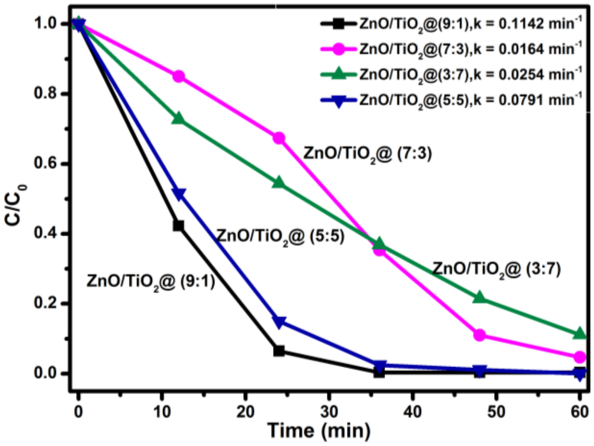

Figure 4.9 Photo-degradation of MO by ZnO/TiO$_2$@ (3:7), ZnO/TiO$_2$@ (5:5), ZnO/TiO$_2$@ (7:3) and ZnO/TiO$_2$@ (9:1)

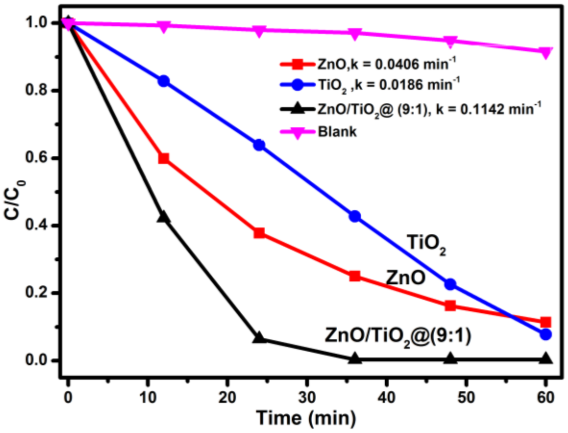

Figure 4.10 A Comparison of the Photocatalytic properties of Blank, TiO$_2$, ZnO and ZnO/TiO$_2$@ (9:1)

However, at 60 mins the activity of ZnO/TiO$_2$@(5:5) is almost similar to that of ZnO/TiO$_2$@(9:1). This is because the absorption edge of the nanocatalyst plays a significant role in the photocatalytic performance. Therefore the broad absorption edge makes it to have a performance better than other nanocomposites (ZnO/TiO$_2$@(7:3)>ZnO/TiO$_2$@(3:7)) except ZnO/TiO$_2$@(9:1). In order to confirm the effectiveness of the nanocomposite catalyst, ZnO and TiO$_2$ were also used in the decomposition experiment and there performance was compared with that of ZnO/TiO$_2$@(9:1) nanocomposite as shown in figure 4.11. The MO degradation process was fitted using linear first-order kinetics and the rate constant (k) is shown in figure 4.11. The rate constant for MO degradation over ZnO/TiO_2 @ (9:1) nanocomposite was about 3 times and 6 times that of ZnO and TiO_2 respectively. Using the rate constant, it is observed that the photocatalytic activity of the ZnO/TiO_2 nanocomposite increases as the concentration of TiO_2 reduces in the nanocomposite matrix that is: ZnO/TiO_2 @ (9:1) > ZnO/TiO_2 @ (7:3) > ZnO/TiO_2@ (5:5) > ZnO/TiO_2@ (3:7). The most efficient nanocomposite catalyst in the degradation of the MO dye is the ZnO/TiO_2 @ (9:1) nanocomposite. This is because the rapid interfacial electron transfer of ZnO and high surface area of TiO_2 is combined in the nanocomposite or the electron-hole recombination is highly reduced.

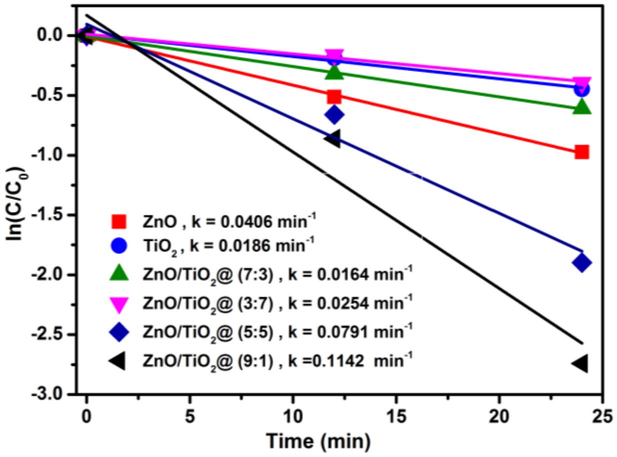

Figure 4.11 Linear fit of ZnO/TiO_2@ (3:7), ZnO/TiO_2@ (5:5), ZnO/TiO_2@ (7:3) and ZnO/TiO_2@ (9:1)

In figure 4.12(a) and (b) the absorption spectrum of TiO_2 and ZnO was compared with the best nanocomposite (ZnO/TiO_2 @ (9:1)) at 60 min irradiation time. The results show that pure ZnO has the highest absorption intensity and ZnO/TiO_2 @ (9:1) have the least absorption intensity. Since the amount of MO removed was estimated by the depreciating absorption curve, ZnO/TiO_2 @ (9:1) has the best photo-activity. In order to investigate the changes that occur in the absorbance of the MO during the photocatalytic activity of ZnO/TiO_2@(9:1), UV-Vis absorbance spectrum of MO dye at different time intervals after removal of ZnO/TiO_2@(9:1) is shown in figure 4.12(c) as it can be observed that the absorbance peak was blue shifted in stepwise average of 2 nm in both the UV and Vis absorption peak of MO .The broadening of the peak increases as the time of irradiation increases.

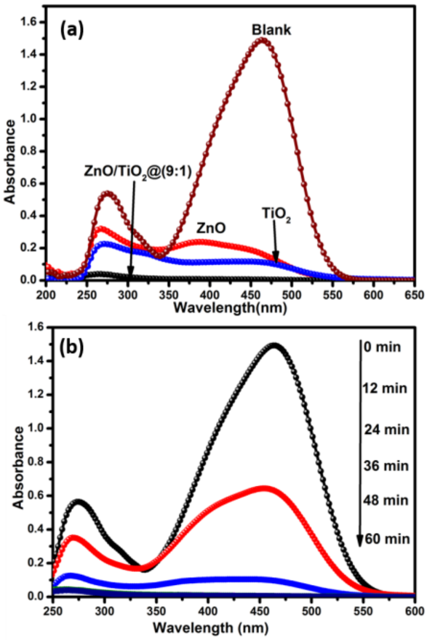

Figure 4.12(a) Absorption spectra of MO dye degraded under UV light irradiation for 60 min using ZnO/TiO_2@ (3:7), ZnO/TiO_2@ (5:5), ZnO/TiO_2@ (7:3) and ZnO/TiO_2@ (9:1)(b) Absorption spectra of MO dye degraded under UV light irradiation for 60 min using TiO_2, ZnO and ZnO/TiO_2@ (9:1) (c) Absorption spectra of MO dye degraded under UV light irradiation for ZnO/TiO_2@ (9:1) at 12 mins time interval.

4.1.8 BET Surface Area and Pore Properties Measurements

The Nitrogen adsorption-desorption isotherms of TiO_2, ZnO NR and ZnO/TiO_2@(9:1) nanocomposites is shown in figure 4.13. The TiO_2 NP (204.69 m^2/g and 0.36 cm^3/g) has a higher BET surface area and BJH adsorption cumulative volume of the pores (total pore volume) than ZnO NR (13.99 m^2/g and 0.04 cm^3/g). The ZnO/TiO_2@(9:1) nanocomposites has BET surface area and total pore volume of 13.80 m^2/g and 0.10 cm^3/g respectively. Therefore, introducing 10% by weight of TiO_2 on the matrix of ZnO NR only improves the pore volume but the surface area is not improved. The Barrett-Joyner-Halenda (BJH) analysis of the desorption isotherms shows the BJH adsorption average pore size of the TiO_2 NP, ZnO NR and ZnO/TiO_2@(9:1) nanocomposites are 6.58 nm, 11.67 nm ad 70.91 nm respectively. Since the pore size of ZnO NR and TiO2 NP is far less than the pore size of ZnO/TiO_2@(9:1) nanocomposites, Hence oxygen and zinc vacancy defect created in ZnO NR as a result of attaching TiO_2 to its surface with PLAL confirmed from photoluminescence and XPS analysis reduced the surface area but created enhanced pore size in the nanocomposite. This large pore size could facilitate dye adsorption thereby improving light harvesting and in the same way improve the electrolyte diffusion in the DSSC which creates enhancement in its photovoltaic performance.

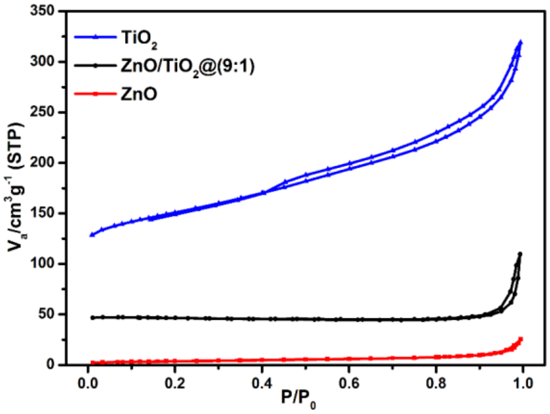

Figure 4.13 (a) N_2 aadsorption-desorption isotherms of ZnO/TiO_2@(9:1)

4.1.9 Charge transfer Mechanism in the solar applications

A possible mechanism that occurs during the photovoltaic and photocatalytic application is illustrated in figure 4.14. In the DSSC, an incident photon excites electrons in the N719 dye (1). The N719 dye injects the excited electron (2) to the CB of ZnO which are later transferred to CB of TiO_2. The electrons are supplied into the back contact of the anode from the CB of TiO_2 and hence it flow through an external circuit to the counter electrode (3). Electron lost in the dye is regenerated by the I_2 based electrolyte (4) and the lost electron in the electrolyte is regenerated by the counter electrode (5). The circuit is completed by transferring electrons to an external load or Auto lab potentiostat through the electrode. In the photo-degradation process, the electrons react with oxygen molecules to form superoxide radical anions (a). The hydroxyl group trap the holes to yield hydroxyl radicals (b). The superoxide radical anions are protonated to generate highly reactive H_2O_2 molecules and hydroxyl radicals (c) and the methyl orange dye in water are oxidized by hydroxyl radicals to form H_2O and CO_2.

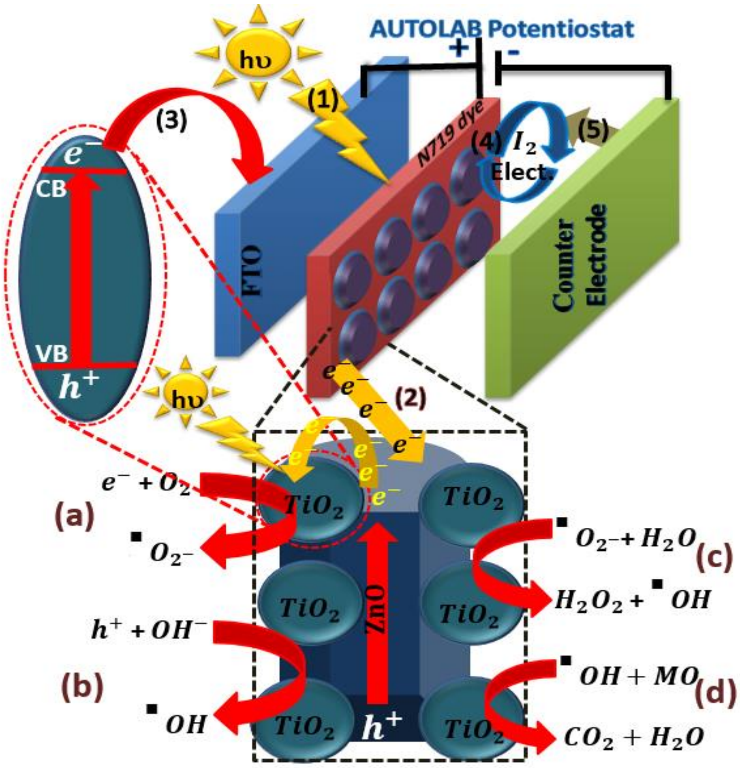

Figure 4.14 Possible photocatalytic mechanism

4.2 The TiO_2/CdS nanocomposite

It was observed that the nanocomposite obtained after laser ablation in liquid vary in color with respect to the concentration of CdS in nanocomposite matrix. The appearance of as-synthesized T-ox-CdS nanocomposite is shown in Fig. 4.15. Herein, T-ox-CdS-10, T-ox-CdS-20, and T-ox-CdS-40 have a gray, Bangladesh green and yellow colors, respectively. Since the TiO_2 and CdS used in this experiment are white and yellow in color, respectively and the prepared mixture is yellowish in color; it is evident that the CdS color is dominant. Since the wavelength of the Nd-Yag laser is within the absorbance wavelength of the CdS nanoparticle, the CdS in the TiO_2/CdS mixture is possibly oxidized during laser ablation in a liquid which brings about the change in color. Hence, T-ox-CdS-20 has a green color because it completely absorbs the laser beam and gets oxidized. T-ox-CdS-40 was partially oxidized because the concentration of CdS is about 50 % in the nanocomposite matrix; whereas the quantity of CdS is very small in the T-ox-CdS-10 nanocomposite. This makes CdS completely oxidized, but the populated TiO_2 nanoparticle limits its ability to absorb the color of the laser beam.

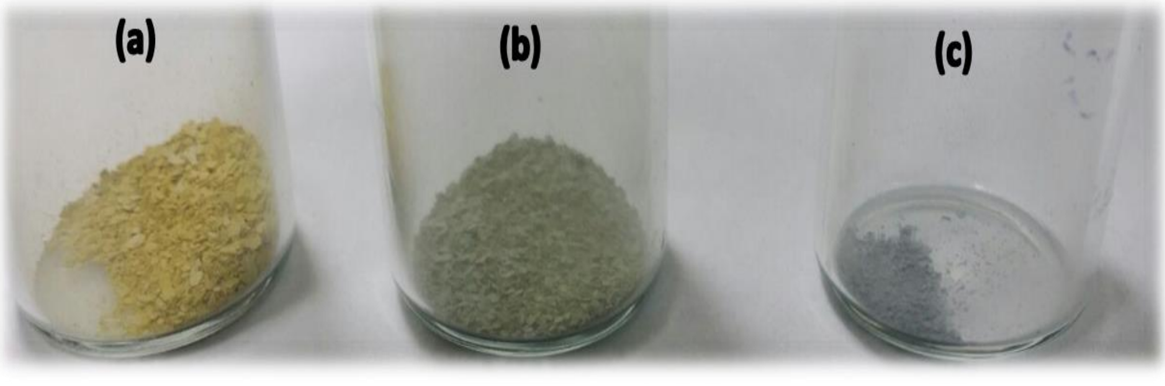

Figure 4.15 Vials of the synthesized nanocomposite (a)T-ox-CdS-40 (b) T-ox-CdS-20 (c) T-ox-CdS-10

The mechanism that occurs within the laser plume is described in Fig. 4.16. The laser Ablation of the TiO_2/CdS mixture in deionised water starts with the absorption of photons (532 nm wavelength) which leads to photoionization and oxidation (loss of electrons) in the nanoparticles when plasma plume is created. Exchange of photogenerated charge carriers occurs within the plasma plume because photogenerated electrons are therefore trapped in the conduction band of TiO_2 as they migrate from the conduction band of CdS to $TiO_{2.}$ Since there would be charge carrier mobilization during the laser ablation because the wavelength of the laser light falls within the broad visible absorption peak of CdS; meanwhile CdS also collects the photogenerated holes migrating away from the valence band of TiO_2. Hence, there would be effective charge separation that makes the synthesized TiO_2/CdS behave like a single entity (nanocomposite). This process is described below

$CdS\ \langle e^-|h^+\rangle + TiO_2 \rightarrow\ TiO_2\ \lceil e^- \rceil + CdS\ \lfloor h^+ \rfloor$

$TiO_2\ \langle e^-|h^+\rangle + CdS\ \langle e^-|h^+\rangle \rightarrow CdS\ \langle h^+ \big| h^+\rangle\ + TiO_2\ \langle e^-|e^-\rangle$

Since the ablation takes place in a medium (Deionized H_2O), there is the possibility of a chemical reaction. During laser ablation process, solvated ions/free ions are created. These ions include Cd^{2+}, O^{2-}, $Ti^{4+,}$ and $S^{2-.}$

There should be an uptake of oxygen from H_2O or TiO_2 by CdS to form

$CdSO_4$/ Cd^{2+}/SO_4^{2-}

That is: $CdS + 2O_2 \rightarrow CdSO_4$ aids the oxidation reaction that occur in the laser plume.

In a north shell, the TiO_2 shares its oxygen with the oxidized CdS to form Ti^{4+}/$CdSO_4$

$TiO_2 + CdS + O_2 \rightarrow (Ti^{4+}|Cd^{2+}|SO_4^{2-})$ Laser plume

$(Ti^{4+|}Cd^{2+}|SO4^{2-})$ Laser plume→ TiO_2-ox-CdS

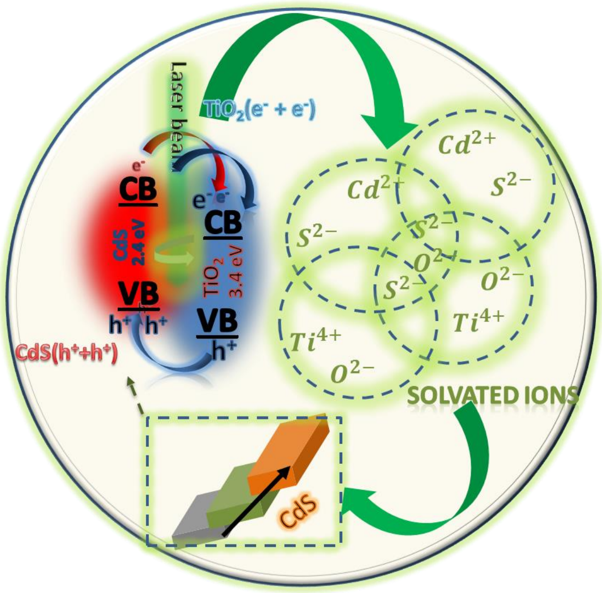

Figure 4.16 Possible Laser Ablation mechanism of the formation of T-ox-CdS

4.2.1 Structural analysis of T-ox-CdS nanocomposites

Fig. 4.17 shows the XRD patterns of TiO_2, CdS and synthesized T-ox-CdS nanocomposites in different ratios. The CdS has cubic zinc blende structure with lattice constant a = 5.8320 Å (JCPDS 41-1049) [148], [149]. The presence of anatase type TiO_2 (JCPDS 211272) with a = 3.7852 Å of the commercial TiO_2 [133] is clearly observed in the produced T-ox-CdS nanocomposites [T-ox-CdS-10, T-ox-CdS-20 and T-ox-CdS-40]. Compared to anatase type TiO_2, there was broadening of the peaks due to the presence of chemical structures formed when there was a reaction between TiO_2 and CdS during Laser Ablation in liquid. This broadening is in the order: T-ox-CdS-10< T-ox-CdS-20 <T-ox-CdS-40. The T-ox-CdS-10 broadened peak at $2\theta = 24.82^0$, 25.62^0, 49.85^0 and 55.13^0 was due to presence of (111) plane of CdS, (111), (113) and (320) of SO_2 (DB card number 01-073-2096) respectively. In addition to these planes the peaks of T-ox-CdS-20 and T-ox-CdS-40 became broader due to the presence of (220) and (332) plane of cadmium oxide sulfate (DB card number: 00-025-0113) at 26.65^0 and 48.48^0 respectively and the titanium sulfate

((113) and (134)) planes located at $2\theta = 24.27^0$ and 47.68^0 respectively according to DB card number:00-042-0230. In addition, the (220) and (311) planes of CdS appeared in the XRD pattern of T-ox-CdS-40 nanocomposite. The presence of these CdS planes were also observed in T-ox-CdS-10 and T-ox-CdS-20 but with low intensity. The Bangladesh green appearance of T-ox-CdS-20 was due formation of cadmium oxide sulfate and titanium sulfate and the transformation to yellow appearance in T-ox-CdS-40 is confirmed with the presence of CdS as shown in the XRD spectra.

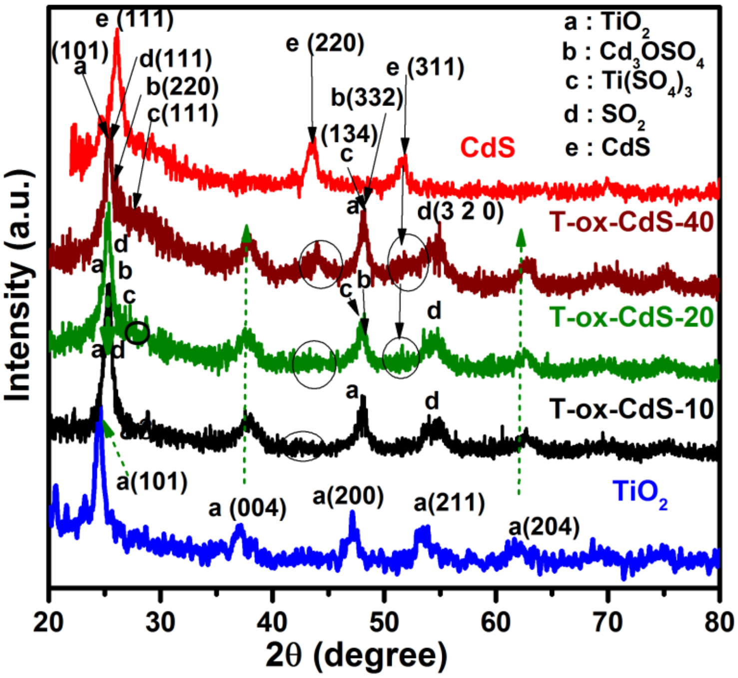

Figure 4.17 XRD pattern of TiO_2, T-ox-CdS-10, T-ox-CdS-20, T-ox-CdS-40 and CdS

4.2.2 Raman spectra analysis of T-ox-CdS nanocomposites

Fig. 4.18 shows the Raman spectra of TiO_2, CdS and synthesized T-ox-CdS nanocomposite. The four fundamental modes in TiO_2 (strong 144.7 cm^{-1}, 378.9 cm^{-1} (B_{1g}), 507.3 cm^{-1} (A_{1g}) and 632.1 cm^{-1} (Eg) bands) is associated with anatase TiO_2 as confirmed with XRD spectra [150]. The Raman active longitudinal optical (LO) phonon, the first

(2LO) and second overtones (3LO) of CdS at approximately 295.7 cm^{-1}, 590.5 cm^{-1} and 901 cm^{-1} respectively were also present in the synthesized CdS respectively [151], [152].

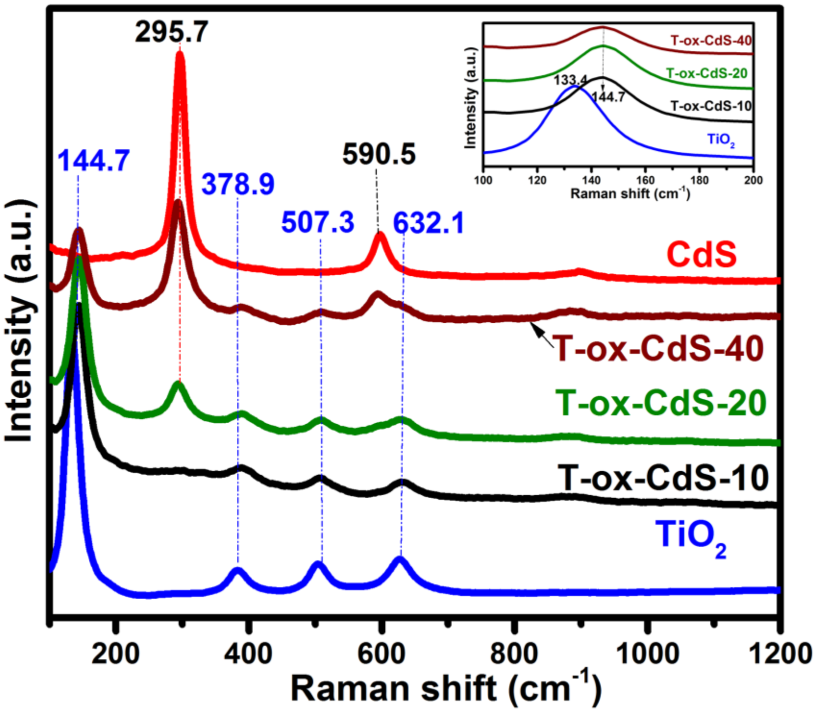

Figure 4.18 Raman spectra of TiO$_2$, CdS, T-ox-CdS-10, T-ox-CdS-20 and T-ox-CdS-40

The anatase low-frequency mode is the most intense peak in T-ox-CdS-20 and T-ox-CdS-10 nanocomposite with <40 wt% of CdS, but T-ox-CdS-40 nanocomposite with >40 wt% conc. of CdS gives the resonantly excited longitudinal optical (LO) phonon of CdS as the most intense peak. At the low-frequency side, asymmetric broadening of the CdS LO mode was observed which can be fitted to the superposition of the LO mode at 592 cm^{-1} and anatase 632.1cm^{-1} (Eg) band. This broadening explains the absence of strong phonon confinement effect [153], in agreement with optical absorbance of TiO$_2$/CdS [152].

4.2.3 Morphology of T-ox-CdS nanocomposites

The SEM image of T-ox-CdS-10 nanocomposite catalyst is shown in **Fig. 6(a)**. This shows the presence of CdS particles aggregates representing CdS nanoparticles homogeneously intertwined into the agglomerated TiO_2 NP. The EDS mapping of the T-ox-CdS-10 nanocomposite shows how the constituent elements namely Ti, O, Cd and S are evenly and homogeneously distributed within the nanocomposite in figure 6(b). The low magnification TEM image of T-ox-CdS is shown in figure 6(c). A very small particles with particle size average of ~ 4-10 nm which is known to be TiO_2 is seen coagulated on the surface of spherical shaped CdS in the range of 10-50 nm in size.

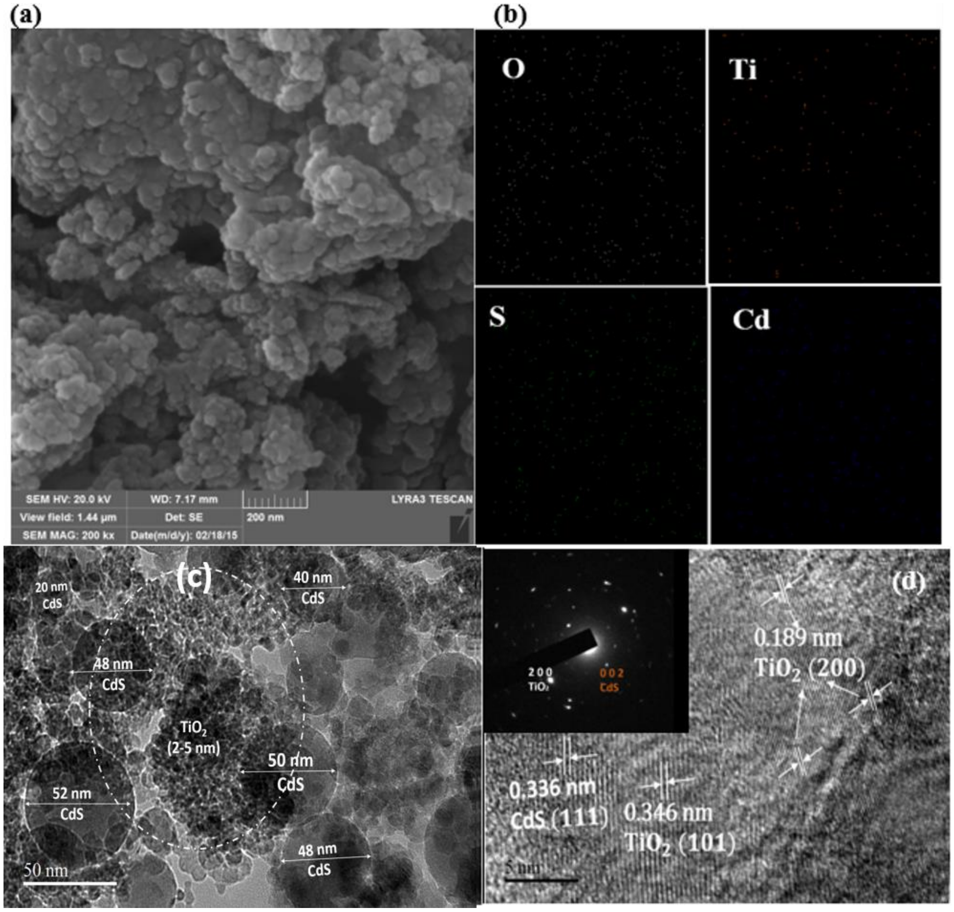

Figure 4.19 SEM image of (a) T-ox-CdS-10 (b)EDS mapping (c) A typical TEM image of T-ox-CdS-10 (inset :SAED of T-ox-CdS-10) (d) HRTEM of T-ox-CdS-10

This shows the TiO_2 nanoparticles became smaller during PLAL process. It was seen that no spherical particle is left unattached with the tiny particles marked out with white dotted circles. However, the particles were uniformly coupled. The high-resolution TEM (HRTEM) image reveals the microstructure of T-ox-CdS-10 nanocomposite in figure 6(d). The CdS coagulated TiO_2 obtained shows fringe spacing of 0.189 nm and 0.346 nm which correspond respectively to (200) and (101) plane of TiO_2 and 0.336 nm of (111) plane in CdS. In the inset of figure 6 (d), the SAED pattern shows a mixture of the anatase TiO_2 phase and cubic CdS by the appearance of diffraction spots matched with (200) plane of TiO_2 and (002) plane of CdS but diffraction spot of TiO_2 is more brightened than CdS because of nanoparticles concentration effect. This is consistent with the XRD pattern. The SAED pattern and HRTEM proves the nanocomposite is still crystalline at the nanoscale.

4.2.4 Optical analysis of T-ox-CdS nanocomposites

The UV-Vis absorption spectra of TiO_2, CdS and synthesized T-ox-CdS nanocomposite are compared in Fig. 4.20. The TiO_2 have a strong absorption in the deep UV region at the absorption edge ca.315 nm with a corresponding band gap of 3.9 eV. The Cubic CdS have a broad absorption in the visible spectral region (350-530 nm) which corresponds to band gap of 2.33 eV. All the T-ox-CdS, absorbance peak was noticed both in UV and Vis spectral region. The UV absorbance peak corresponds to that of TiO_2 and the Vis peak corresponds to that of CdS. The Vis peak becomes less pronounced as the concentration of CdS reduces from T-ox-CdS-40 to T-ox-CdS-10. Hence, the visible spectral sensitivity of the nanocomposite is a function of CdS concentration.

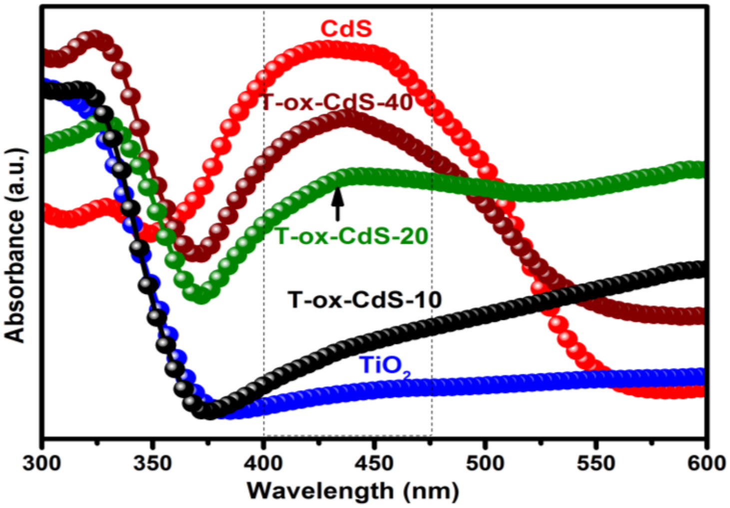

Figure 4.20 Absorption Spectra of (a)TiO_2 (b)T-ox-CdS-10 (c)T-ox-CdS-20 (d)T-ox-CdS-40 and (e) CdS

In Fig. 4.21 shows the FTIR spectra of CdS, TIO_2, and T-ox-CdS nanocomposites. The Cd-S bond is observed in the range of 550- 690 cm^{-1}[154]. The presence of Ti-O-Ti, lattice vibration of TiO_2 and Ti-OH is observed at 630cm^{-1}[155],1420 cm^{-1} and 1630 cm^{-1} absorption bands [156]respectively.

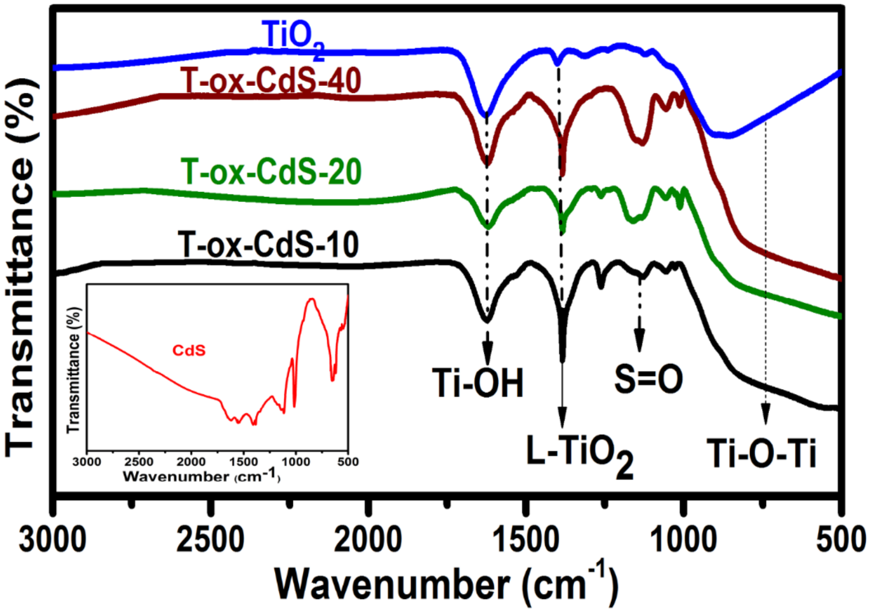

Figure 4.21 FTIR Spectra of TiO_2, CdS, T-ox-CdS-10, T-ox-CdS-20 and T-ox-CdS-40

All these absorption band do not change in intensity because percentage weight of TiO_2 is maintained in the nanocomposites. The relatively intense S=O vibrational absorption band associated with the bond between the S in CdS and Oxygen in TiO_2 is observed at 1094-1220 cm^{-1} [157] in all the samples. This absorption band decreases in intensity with respect to decreasing the concentration of CdS in the nanocomposites (T-ox-CdS-40> T-ox-CdS-20> T-ox-CdS-10). This indicates that sulfate is present in all the nanocomposite but very minimal in the T-ox-CdS-10 nanocomposite.

4.2.5 XPS Analysis of T-ox-CdS nanocomposites

The possible chemical reaction during laser ablation and valence state of the elements in T-ox-CDS-10 was investigated using XPS analysis. Fig. 4.22(a-d) shows the high-resolution scan of Ti 2p, O 1s, Cd 3d, S 2p, that appears in the survey scan. The spin-orbit split was observed in Ti 2p and Cd 3d states.

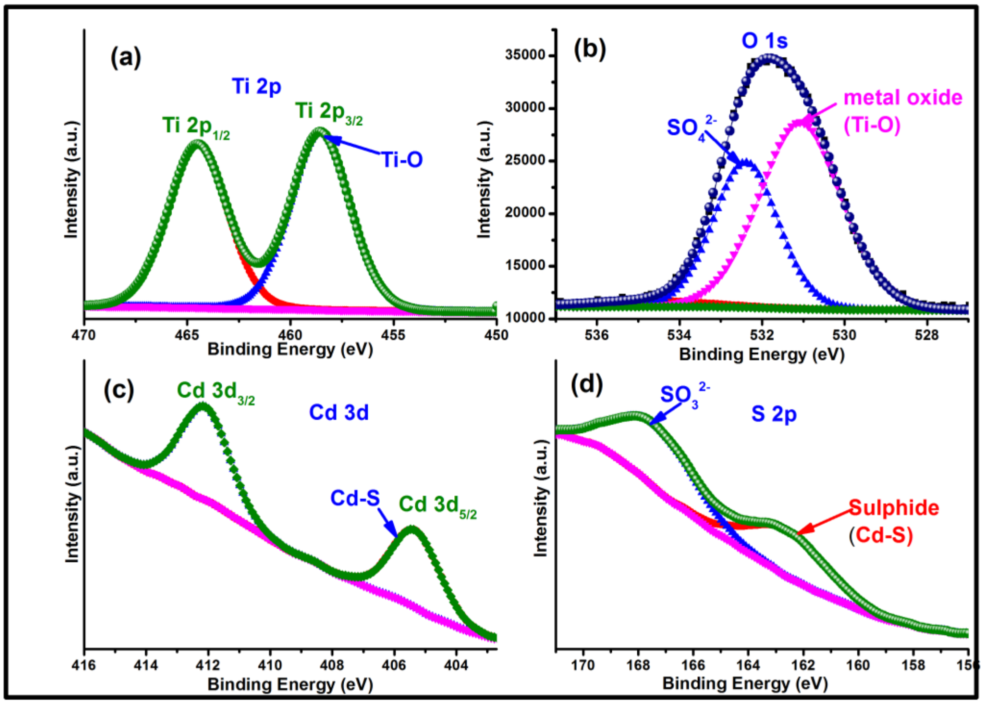

Figure 4.22 XPS analysis of T-ox-CdS-10

In Fig. 4.22(a) the Ti $2p_{3/2}$ peak was fitted into a single peak located at 458.7 eV indicating the presence of Ti-O bond in the sample [36]. The O1s peak in Fig. 4.22(b) was deconvoluted into two peaks located at 531.1 eV and 532.6 eV which are assigned to metal oxide bond, and sulfate [36, 38]. The $Cd3d_{5/2}$ peak of the spin-orbit split peak was fitted as shown in Fig. 4.22 (c) into peaks positioned at 405.2 eV attributed to Cd-S bond in the sample. The deconvoluted sulfur peak in Fig. 4.22(d) positioned at 167.5 and 163.5 eV was linked with the presences of sulfate (SO_3^{2-}) and S in the CdS sample which agrees with the FTIR result. The sulfate found in the S 2p and O1s peak confirms the CdS is oxidized during the ablation process.

4.2.6 BET Surface Area and Pore Properties Measurements.

The Nitrogen adsorption-desorption isotherms and the Barrett-Joyner-Halenda (BJH) analysis of the desorption isotherms of TiO_2, CdS and T-ox-CdS-10 samples are shown in figure 4.23. The presence of hysteresis loop indicates the TiO_2 NP, CdS and T-ox-CdS-10 nanocomposite are mesoporous. The TiO_2 NP (204.69 m^2/g and 0.36 cm^3/g) has a higher BET surface area and BJH adsorption cumulative volume of the pores (total pore volume) than CdS (34.81 m^2/g and 0.17 cm^3/g). The BET surface area and total pore volume of T-ox-CdS-10 (147.4 m^2/g and 0.32 cm^3/g) is increased as compared with that of CdS but reduced when compared with TiO_2.This might be because the presence of CdS in TiO_2 results in a slight increase in the crystal size. Larger crystallite size results in a smaller surface area. The CdS (20.49 nm) has a BJH adsorption average pore size width larger than TiO_2 NP (6.58 nm). The pore size of T-ox-CdS-10 (8.44 nm) is more than that of TiO_2 but less than CdS strongly suggests that the surface and pore of TiO_2 is covered and blocked with CdS during the formation of T-ox-CdS-10 that contains 10% by weight of CdS as described in the SEM and TEM image. Therefore enhancement in the photovoltaic performance of T-ox-CdS-10 can be related to its large pore size which could facilitate dye adsorption thereby improving light harvesting and in the same way improve the electrolyte diffusion in the DSSC.

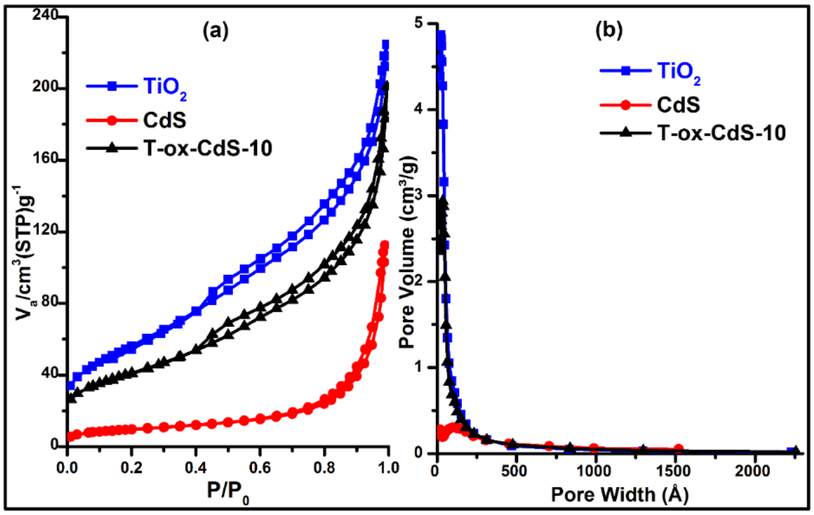

Figure 4.23 (a) N_2 aadsorption-desorption isotherms and (b) pore size distribution of TiO_2, CdS and T-ox-CdS-10

4.2.7 Photocatalytic activity analysis

The photo-oxidation capability of the nanocomposites was evaluated by the degradation of MO dye in solution over the synthesized T-ox-CdS nanocomposite under UV and Vis light irradiation. A comparative experiment was done by comparing the activity of CdS and TiO_2 with the nanocomposites under the same experimental condition. The relative concentration ((C/C_0), C_0 is the initial concentration and C is the final concentration after the MO degradation for time t) as a function of time is shown in Fig. 4.24(a). The MO was kept under UV-vis light to confirm the aforementioned high stability of MO under solar irradiation. This was shown by the almost unchanged relative concentration with irradiation time. The decomposition of the chromophoric structure of MO was confirmed by a gradual change in the color of the suspension as the reaction time increases. The UV-Vis photocatalytic activity of T-ox-CdS-10 was the highest. The activity of TiO_2 supersedes T-ox-CdS-40, T-ox-CdS-20, and CdS because oxidation occurs in the aforementioned nanocomposites during Photodegradation process. T-ox-CdS-20 has the lowest activity because the charge carriers needed for degradation are almost insufficient due to pre-oxidation that occurs in it during Laser ablation. A plot of ln(C/Co) against time in Fig. 4.24(b), shows the decomposition kinetics follows the first order kinetics linear profile. Using the classical equation $\ln\left(\frac{C}{Co}\right) = -q.t$, where q is the so called pseudo first rate kinetic constant, The presented q values in Fig. 4.24(b) are from fitting curves of the data for a 0 - 60 min period.

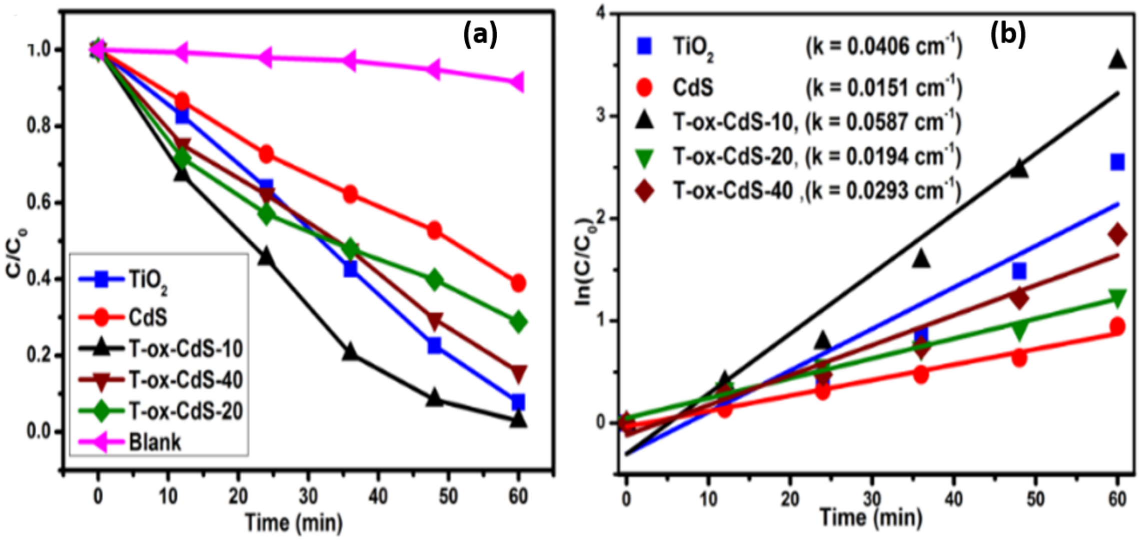

Figure 4.24 Photocatalytic performance of TiO_2, CdS, T-ox-CdS-10, T-ox-CdS-20 and T-ox-CdS-40 for the degradation of MO solution

These values represent a good measurement of the overall photo degradation rate of all the investigated structures. T-ox-CdS-10 with q = 0.0587 min^{-1} that corresponds to 30 % and 74 % increase of TiO_2 and CdS kinetic constant, respectively has the fastest MO decomposition rate. The photocatalytic activities of T-ox-CdS increase as oxidation of CdS decreases (T-ox-CdS-20>T-ox-CdS-40>T-ox-CdS-10). In order to investigate the changes that occur in the absorbance of the MO during the photodegradation activity of T-ox-CdS-10. The UV-Vis absorbance spectrum of MO dye at different time intervals after removal of T-ox-CdS-10 was shown in Fig. 4.25(a) as it was observed that the absorbance peak was blue shifted in stepwise average of 2 nm in both the UV and Vis absorption peak of MO. The rate of decomposition of MO was further investigated by comparing the absorption spectrum of MO after 60 mins decomposition with the nanocatalyst as shown in Fig. 4.25(b). The major absorption peak of MO around 464 nm diminished gradually under UV-vis light irradiation in the presence of the synthesized nanocomposite.

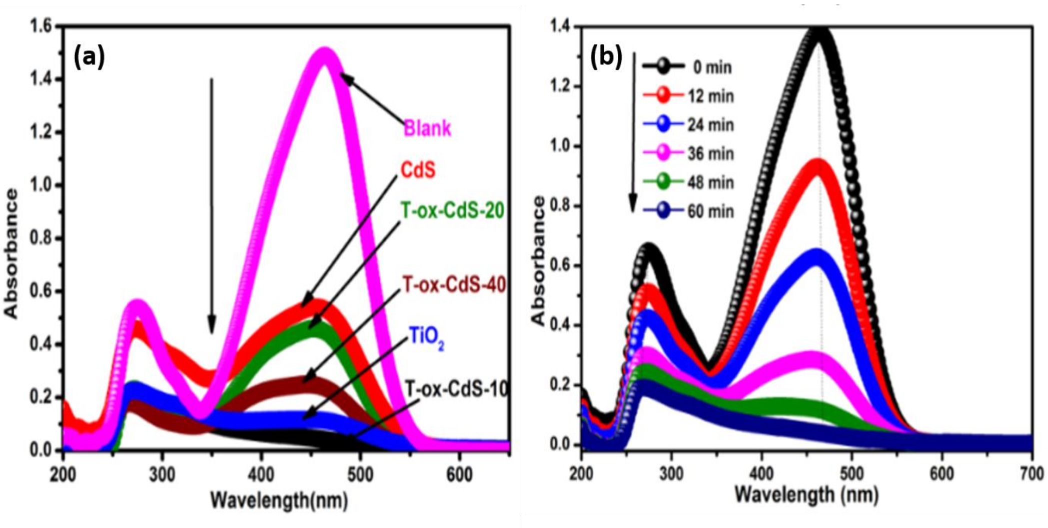

Figure 4.25 Absorption spectra of (a) MO dye degraded under UV-Vis light irradiation for 60 min using CdS, T-ox-CdS-40, T-ox-CdS-20 and T-ox-CdS-10 (b) T-ox-CdS-10 and TiO_2 (b) MO dye degraded under UV-Vis light irradiation at 12 mins time interval using T-ox-CdS-10.

The result obtain shows that the absorption intensity decreases in the order T-ox-CdS-20>CdS>T-ox-CdS-40>TiO_2>T-ox-CdS-10, Since the amount of MO that was decomposed was estimated by the depreciating absorption curve, after 60 mins of irradiation 97%, 92%, 83%, 72% and 68% of MO was removed by T-ox-CdS-10, TiO_2, T-ox-CdS-40, CdS and T-ox-CdS-20 hence T-ox-CdS-20 has the highest absorption with least activity and T-ox-CdS-10 has the least absorption intensity with best activity.

4.2.8 Photovoltaic performance analysis

A typical current density (J) versus voltage (V) curve demonstrating the effect of oxidized CdS concentration in the synthesized T-ox-CdS nanocomposite was shown in Fig. 4.26and the obtained photovoltaic parameters such as Voc and Jsc values with the calculated Fill factor (FF) and efficiency (Ƞ) was shown in Table 4.2. Fig. 4.26 shows T-ox-CdS-40 with the highest concentration of CdS has the highest Voc and Jsc due to improvement in light harvesting. T-ox-CdS-20 has the least Voc and Jsc because the CdS present in the composite was completely oxidized during laser ablation the composite in the liquid medium. T-ox-CdS-10 has an almost similar value of Voc and Jsc with T-ox-CdS-40 because the oxidized CdS present in T-ox-CdS-10 is overwhelmed by TiO_2, therefore, reducing the tendency of oxidation and electron-hole recombination to occur in nanocomposite during laser ablation. The fill factor of T-ox-CdS-40 is ~ 0.32, which is low compared with T-ox-CdS-10 with ~0.49 because of high concentration of oxidized and un-oxidized CdS present in T-ox-CdS-40. This compensates for the little difference between their Jsc and Voc values and hence the performance of T-ox-CdS-10 supersede. Hence, T-ox-CdS-10 exhibited the highest efficiency of 4.296 %. with J_{SC} of 1.25 mA/cm^2, Voc of 0.55 V and FF of 0.49 as compared to pure TiO_2 and CdS based DSSC with Ƞ of 0.56 and 0.21%, J_{SC} of 0.85 and 0.53 mA/cm^2,Voc of 0.18 and 0.11 V; same FF of 0.29. This shows that T-ox-CdS-10 is an improved catalyst over TiO_2 and CdS. This is almost 20 and 7.6 times the photoconversion efficiency (Ƞ) enhancement of T-ox-CdS-10 compared to CdS and TiO_2.

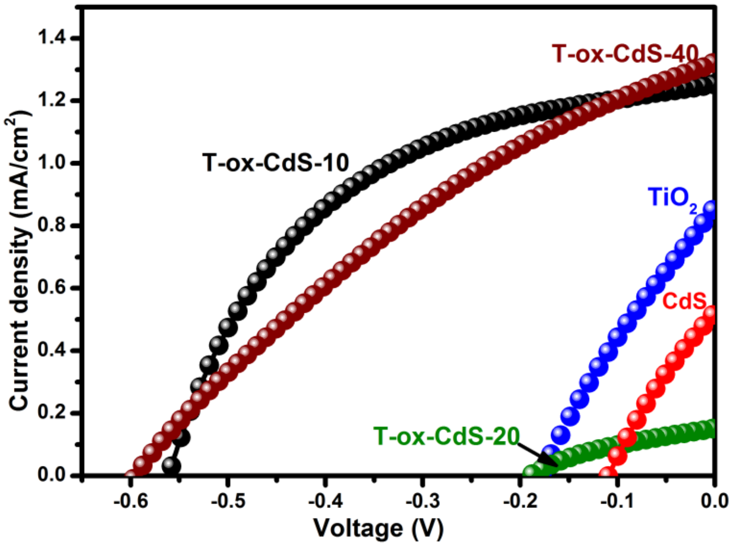

Figure 4.26 J-V curve of TiO$_2$, T-ox-CdS-10, T-ox-CdS-20, T-ox-CdS-40 and CdS

The electrochemical impedance spectroscopy (EIS) is used to analyze the internal resistance and charge transport process within a photovoltaic device. The role electron-hole recombination that occur in T-ox-CdS nanocomposite (T-ox-CdS-10, T-ox-CdS-20, and T-ox-CdS-40) photoanode used in fabricated DSSCs is explained using EIS analysis which described by the Nyquist plot shown Fig. 4.27.

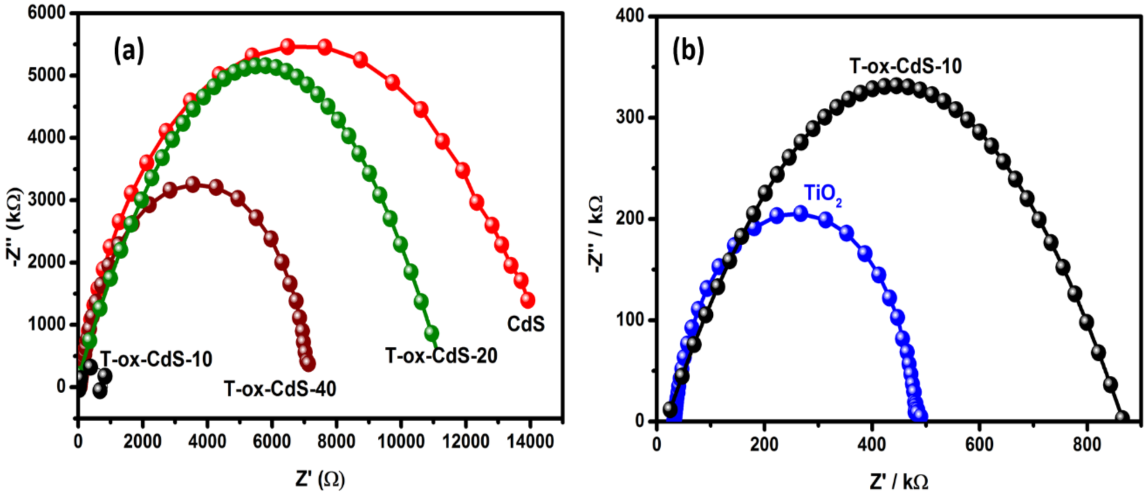

Figure 4.27 Nyquist plot of (a) CdS, T-ox-CdS-40, T-ox-CdS-20 and T-ox-CdS-10 (b) T-ox-CdS-10 and TiO$_2$

A decrease in charge transfer resistance (R_{CT}) of the TiO_2-ox-CdS composite indicates an increase in electron transport and increase in electron collection efficiency. Hence, the R_{CT} values obtained are shown in Table 4.2, It is observed that the R_{CT} values decreases in the order: CdS > T-ox-CdS-20 > T-ox-CdS-40> T-ox-CdS-10>TiO_2. This explains the rate of oxidation of CdS during Laser ablation and concentration of CdS affects the R_{CT} value because during laser ablation the nanocomposite undergoes an oxidation reaction when excited by the 532 nm wavelength laser beam and this can aggravate the electron-hole recombination.

Table 4.2 J-V characteristics of the DSSCs with TiO_2, CdS, T-ox-CdS-10, T-ox-CdS-20 and T-ox-CdS-40 nanocomposite.

	J_{SC} (mA/cm^2)	**Voc (V)**	**FF (%)**	**Ƞ (%)**	**Rct (kΩ)**
TiO_2	**0.852**	**0.1787**	**0.2932**	**0.56**	**0.48**
CdS	**0.532**	**0.1084**	**0.2962**	**0.21**	**0.18**
T-ox-CdS-10	**1.248**	**0.5581**	**0.4935**	**4.30**	**0.16**
T-ox-CdS-20	**0.150**	**0.1904**	**0.3348**	**0.12**	**0.52**
T-ox-CdS-40	**1.331**	**0.5927**	**0.3252**	**3.21**	**1.55**

This also shows that the photoconversion efficiency of the nanocomposite varies with R_{CT}. CdS and all the nanocomposite has a higher charge transfer resistance than TiO_2, the incorporation of CdS creates electron-hole recombination enhancement in TiO_2 but the reverse occur when TiO_2 is introduced into CdS. In Fig. 4.25(c), T-ox-CdS-10 has a higher R_{CT} value than TiO_2 because the incorporation and oxidation of CdS in TiO_2 matrix during laser ablation has improved its electron-hole recombination but the electron generation is increased because there is an improved absorption in the visible spectral region which makes the electron-hole recombination rate negligible factor and hence open circuit voltage is improved.

4.2.9 Charge transfer mechanism in the solar applications

The Photodegradation of MO dye process described in Fig. 4.28 is explained as: The UV-Vis light excites electrons which are hindered from recombination. The electrons react with molecular oxygen to produce superoxide radical anions (a), hydroxyl radicals generated by hole trapping activity of hydroxyl group (b) and hydroxyl radicals oxidize the methyl orange in water to form CO_2 and H_2O (c). The photodegradation efficiency varies in the order T-ox-CdS-10< TiO_2<T-ox-CdS-40< CdS < T-ox-CdS-20.This shows that during the degradation process CdS undergoes another oxidation process. Since the rate of oxidation determined by the rate of electron-hole recombination in the nanocomposite depends on the concentration of CdS hence T-ox-CdS-10 that is active in UV-Vis spectral region with least oxidation activity and charge recombination has the best performance. In the operation mechanism of the DSSC described in Fig. 4.28, where the synthesized T-ox-CdS Nanocomposites are used as photoanode. (1) The solar irradiation excites electrons from the CdS and the N719 dye, the electron at the gateway of CdS and the photoexcited electron from the dye are therefore transferred to the conduction band of TiO_2 (2) before being conveyed to the electrode by the electrolyte (3). The lost electron in the dye is therefore replenished by the redox electrolyte (4) and the redox electrolyte gets regenerated by the counter electrode (5) which is used with the main electrode (FTO) to convey electric charges to the outside circuit (Auto lab potentiostat). The photoconversion efficiency of the nanocomposite varies in the order: T-ox-CdS-10> T-ox-CdS-40>TiO_2> CdS > T-ox-CdS-20. Since the nanocomposite has no contact with water during photoexcitation, minimum oxidation activity occurs in all the nanocomposite. Compared with the order at which the nanocomposite efficiently photodegrades as shown in Fig. 4.28, T-ox-CdS-40 has a better performance than TiO_2 in this case because they are active in both the UV and Vis spectral region and minimum oxidation occurs during the reaction process. T-ox-CdS-10 has a better performance than T-ox-CdS-40 in both cases (DSSC and photodegradation) because the percentage ratio of TiO_2 to CdS is good enough for the conduction band of TiO_2 to trap photogenerated electrons ready to recombine with the holes and the CdS is moderate enough for visible light sensitivity. A reduced performance occurs in T-ox-CdS-40 because the percentage ratio is not sufficient enough for the elimination of charge recombination. The performance of the nanocomposite varies in the two photocatalytic application. Hence, T-ox-CdS-20 has a lower performance than CdS because almost all the charge carriers have recombined during laser ablation making it to completely change its color to that of the laser beam. CdS has some electrons in its conduction band ready to be activated by visible light.

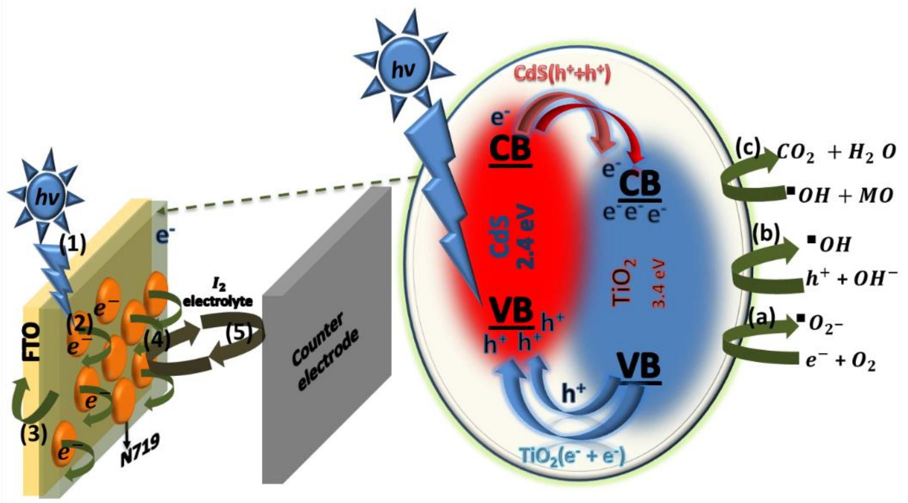

Figure 4.28 Schematic describing the photocatalytic application mechanism of T-ox-CdS nanocomposite.

4.3 The TiO_2-graphene nanocomposite

4.3.1 Optical analysis of TiO_2-graphene nanocomposite

The absorption spectra of TiO_2 and G@k-TiO_2 nanohybrid are given in Figure 4.29. An obvious absorption peak was observed at 324 nm for TiO_2 and a flat absorption band in the region between 300 and 334 nm was obtained for the entire G@k-TiO_2 nanohybrid. Also, a flat and broad absorption band was observed in the visible spectral region. This flat absorption band in the ultraviolet (UV) and visible (Vis.) absorption regions is due to the bonding of surface carbon from graphene with oxygen in the TiO_2 matrix. Hence, this can aid improvement in photocatalytic and photovoltaic performance. This means that hybridization of graphene can enhance the ability of TiO_2 matrix to generate charge carriers when exposed to UV and visible light. Thus, use of graphene with TiO_2 can aid the photocatalytic and photovoltaic performance.

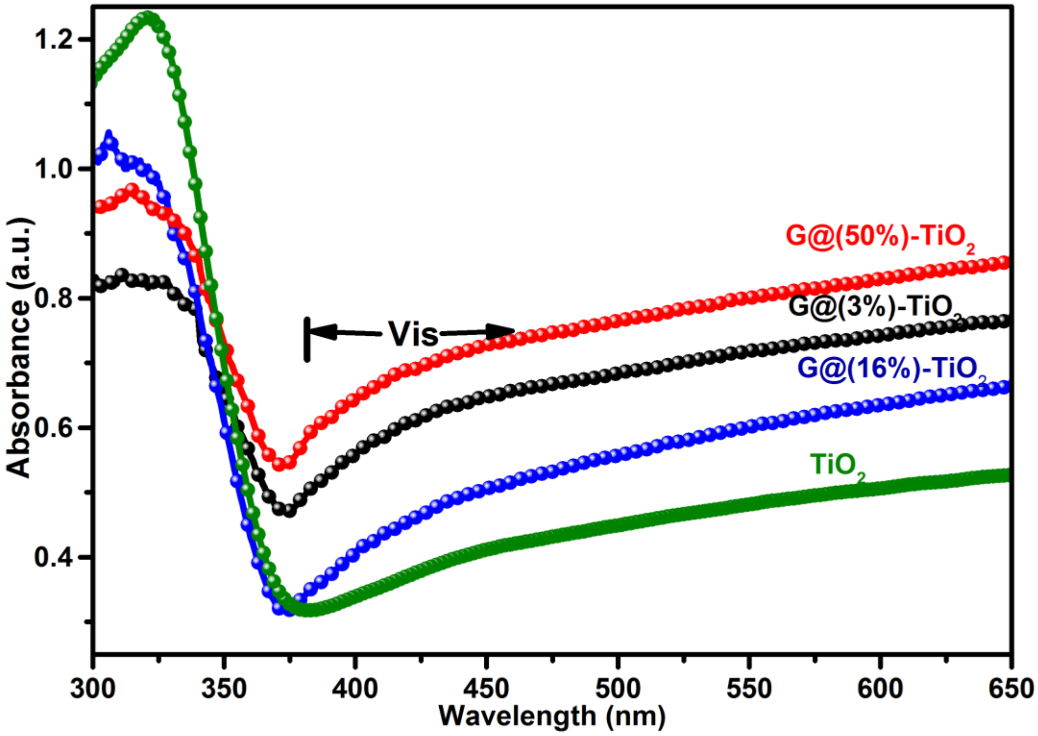

Figure 4.29 UV-Vis spectra of G@k-TiO_2 nanohybrid (a) TiO_2 (b) G@(16%)-TiO_2 (c) G@(50%)-TiO_2 (d) G@(3%)-TiO_2

The FTIR spectra of the TiO_2 and G@k-TiO_2 nanohybrid are shown in Fig. 4.30. A broad peak observed at 3201 cm^{-1} corresponds to the stretching vibration of the adsorbed water on the surface. This peak broadening was due to the adsorption of water on the surface during the PLA synthesis of G@k-TiO_2 in water. The peaks situated at 1648 cm^{-1} and 1409 cm^{-1} are produced due to the bending vibration of Ti–OH and Ti–O–Ti bonds present, respectively in TiO_2 and G@k-TiO_2 nanohybrid. This result indicates the presence of TiO_2 in nanohybrid matrix. In the nanohybrid, the 1648 cm^{-1} band was broadened because of the presence of C=O stretching vibrations of the COOH groups at 1740 cm^{-1}. The presence of C-OH group, the C-O stretching vibrations and the epoxide groups indicated by the peaks positioned at a 1363 cm^{-1}, 1097 cm^{-1} and 1230 cm^{-1} respectively is a signature of the bond formed between the carbon in graphene and titanium dioxide which is observed and stated in absorption spectrum of the G@k-TiO_2 nanohybrid.

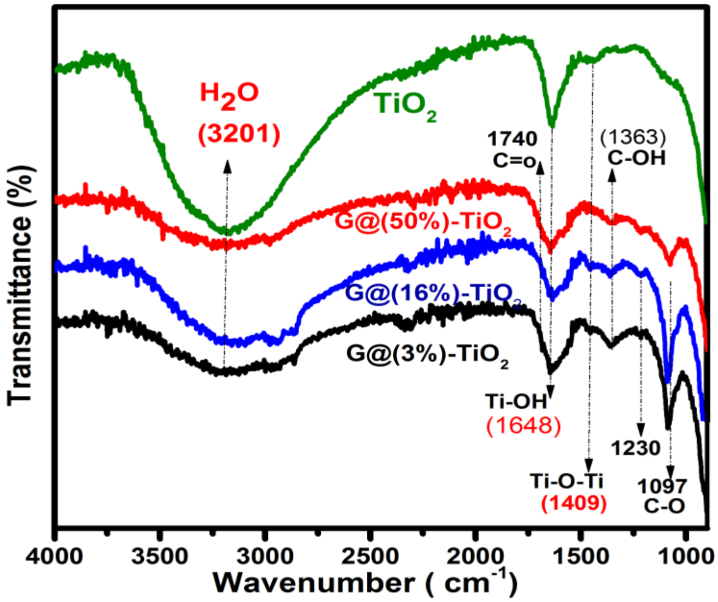

Figure 4.30 FTIR spectra of G@k-TiO_2 nanohybrid (a) TiO_2 (b) G@(50%)-TiO_2 (c) G@(16%)-TiO_2 (d) G@(3%)-TiO_2

4.3.2 Structural analysis of TiO_2-graphene nanocomposite

The crystalline phase of TiO_2, G@(3%)-TiO_2, G@(16%)-TiO_2 and G@(50%)-TiO_2 nanohybrid catalysts are investigated using the XRD spectra shown in Fig. 4.31. The patterns of both TiO_2 and graphene-TiO_2 Nano-hybrid catalysts exhibit diffraction peaks positioned at 2θ: 37.9°, 47.8°, 54.3°, 55°, and 62.7°, indexed as the characteristic (004), (200), (105), (211) and (204) peaks of anatase TiO_2 (JCPDS 21-1272) phase [131].

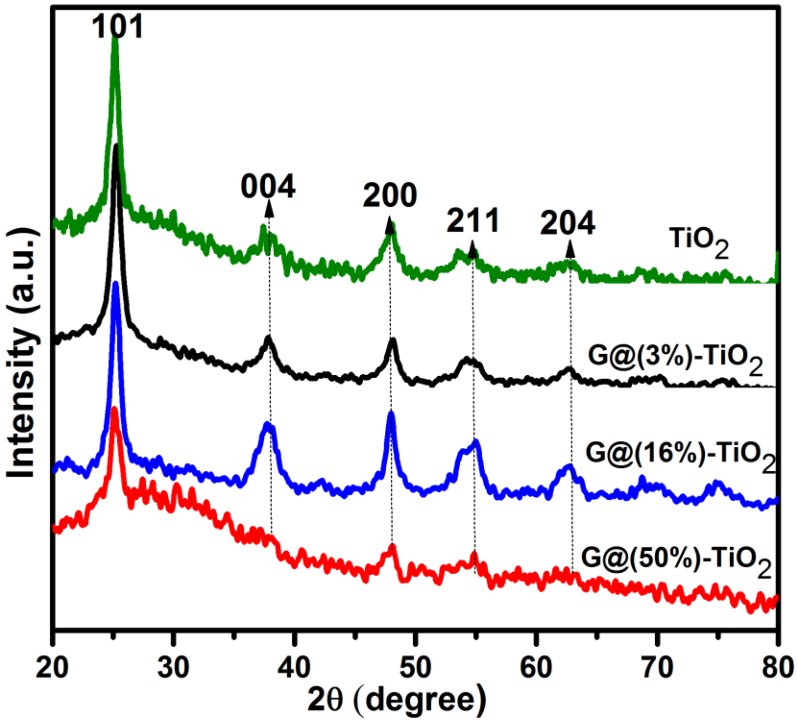

Figure 4.31 XRD pattern of TiO_2, G@(3%)-TiO_2, G@(16%)-TiO_2 and G@(50%)-TiO_2

It can be stated that anatase form of TiO_2 is dominant in the prepared nanohybrid The characteristics peaks of graphene which were supposed to be observed at 2θ ~ 25.8^0 and ~ 42.8^0 indexed to (002) and (100) reflections of graphene (JCPDS 01-0646)[158] [159] were suppressed due to high intensity of TiO_2 peak in the XRD pattern of G@(3%)-TiO_2, G@(16%)-TiO_2 and G@(50%)-TiO_2 nanohybrid. It is observed that, crystallinity was improved in G@(3%)-TiO_2 Nano-hybrid due to appearance of well-defined peaks and peak broadening started to occur in G@(16%)-TiO_2 which became more prominent in G@(50%)-TiO_2 nanohybrid distorting the appearance of (004), (200) major peaks. Therefore crystallinity was diminished in G@(50%)-TiO_2 nanohybrid and it can be concluded that, the crystallinity would be greatly affected when the concentration of graphene becomes too high in a nanohybrid.

4.3.3 Raman spectra analysis of TiO_2-graphene nanocomposite

Raman spectroscopy was used to determine the characteristics peaks of graphene and to investigation further the crystal structure of the TiO_2, G@(3%)-TiO_2, G@(16%)-TiO_2 and G@(50%)-TiO_2 nanohybrid catalysts. The Raman spectra of pure TiO_2, G@(3%)-TiO_2, G@(16%)-TiO_2 and G@(50%)-TiO_2 Nano-hybrid catalysts are shown in Fig. 4.32

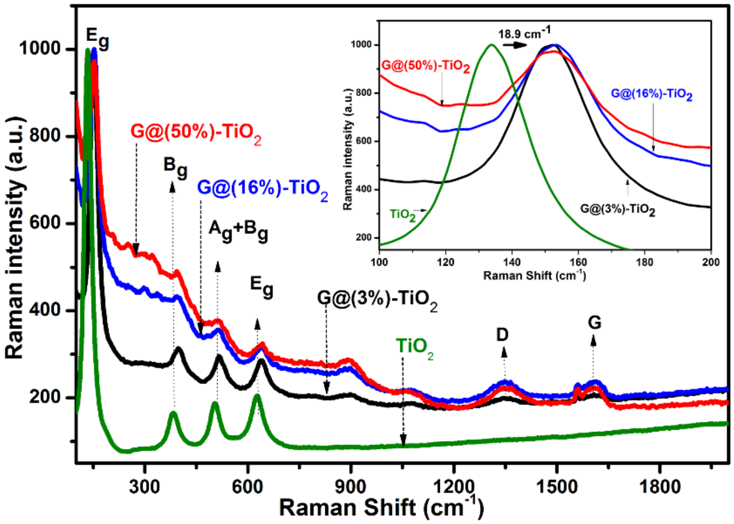

Figure 4.32 Raman spectra of G@k-TiO_2 nanohybrid TiO_2, G@(50%)-TiO_2 , G@(16%)-TiO_2 and G@(3%)-TiO_2

The characteristics of pure anatase TiO_2 is described by the presence of the four bands located at ~135.6 (E_g), 395 (B_g), 513 ($A_g + B_g$) and 637 cm^{-1} (E_g). However, it was observed that the Eg mode in case of nanohybrid got shifted towards higher wavenumbers to 162.9

cm^{-1} (red shift). This shift in Eg band demonstrates that higher oxygen vacancies are present in the nanocomposites than pure TiO_2 [160]. In addition, four lower wave number bands located at ~1356 and 1600 cm^{-1} is found in all the graphene-TiO_2 nanohybrid spectra**.** These two bands are identified as the characteristic bands of graphene, known as D- and G-band, respectively. The presence of D-band in the graphene spectrum is due to the structural disorder, defects and is a signature of the vibrational modes of ring-like sp^2 atoms. compared to G@(3%)-TiO_2, more structural disorder is observed in G@(16%)-TiO_2 and G@(50%)-TiO_2 due to increase in the intensity of D-band in the order (G@(3%)-TiO_2 < G@(16%)-TiO_2 < G@(50%)-TiO_2)which is directly related with the increase. This explains why a reduction in crystallinity was observed in the XRD pattern of G@(16%)-TiO_2 and G@(50%)-TiO_2 Nano hybrids. The stretched sp^2-hybridized carbon-carbon bonds are described with a G-band, which is strain effect sensitive in graphene sheet sp^2 systems. However, strain effect sensitivity increases in the order of (G@(3%)-TiO_2 < G@(16%)-TiO_2 < G@(50%)-TiO_2. This result is almost consistent with the order at which the major peaks become broadened in the XRD pattern and Also observed is the broadening of the other TiO_2 bands as the graphene concentration increases which explains a possible interaction between TiO_2 nanoparticles and graphene sheets in the G@(3%)-TiO_2, G@(16%)-TiO_2 and G@(50%)-TiO_2 nanohybrids.

4.3.4 Morphology of G@ (3%)-TiO_2 nanohybrid

The morphology of CVD grown graphene was investigated with Transmission electron microscopy (TEM). Figure 4.33(a) shows the graphene sheets having to fold at many places due to it atomically thin nature. The inset image is an SAED pattern shows the hexagonal structure of graphene crystal.

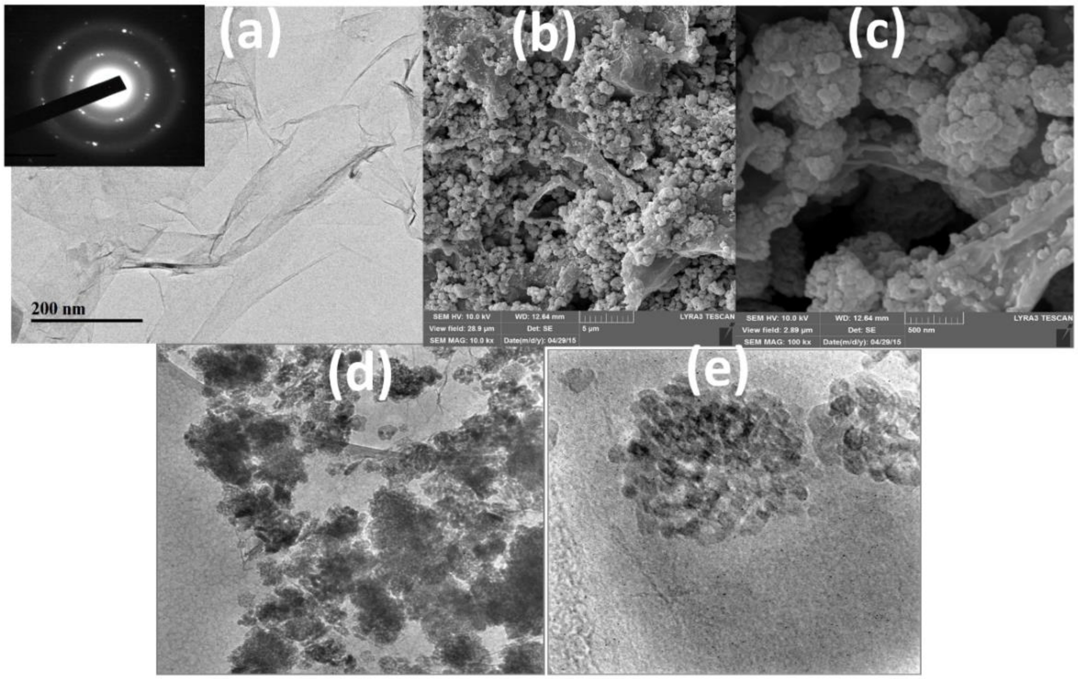

Figure 4.33 (a) A typical TEM image of CVD grown graphene sheet over carbon film showing folding (inset: selected area electron diffraction (SAED) pattern of the graphene where hexagonal planes of the graphene can be seen). (b) FESEM Image of G@ (3%)-TiO_2 Nanohybrid (c) high magnification of G@(3%)-TiO_2 Nanohybrid (d) TEM image of synthesized G@(3%)-TiO_2 Nanohybrid (e) high magnification TEM image of TiO_2 nanoparticles attached with a graphene sheet.

These graphene sheets were used to prepare a G@ (3%)-TiO_2 Nanohybrid. G@ (3%)-TiO_2 Nanohybrid was characterized by field-emission scanning electron microscopy (FE-SEM) and TEM). FESEM and TEM image of G@ (3%)-TiO_2 Nanohybrid was shown in Fig. 4.33(b-e)) gives a visible appearance of agglomerated spherical TiO_2 nanoparticles on the graphene sheets. The high magnification of one agglomerated section shown in Fig. 4.33(c & e) confirms the TiO_2 nanoparticles were dispersed and closely engraved on the surface of the functionalized graphene sheets. It is a well-known phenomenon that when two particles of opposite charge are brought together, a mutual coagulation may occur, leading an easy electron conduction from conduction band of TiO_2 to graphene, and reducing charge recombination substantially.

4.3.5 XPS Analysis of G@ (3%)-TiO_2 nanohybrid

The oxidation states of the elements in the G@(3%)-TiO_2 and the attached group to the surface of TiO_2 nanoparticles are investigated using XPS analysis. The survey spectrum of the G@(3%)-TiO_2 is shown by Fig. 4.34 (a). The characteristic energy peaks of the three elements: titanium (Ti 2p), oxygen (O 1s) and carbon (C 1s) can be observed by this spectrum. The XPS of Ti 2p peak shown in figure 4.34 (b) has a spin-orbit split which is located at 460.0 eV (Ti $2p_{3/2}$) and 465.7 eV (Ti $2p_{1/2}$). The Ti $2p_{3/2}$ peak is de-convoluted into two peaks, the first peak located at 460.0 eV undergoes a shift to higher binding energy as compared to Ti in bulk anatase TiO_2 which explains the effect of graphene sheet shielding on TiO_2 nanoparticles[161] and the second peak at 458.3 eV is associated with Ti in TiO_2 [41, 42] . The amount of unshielded TiO_2 is very less as confirmed by relating the intensity of TiO_2 peak which is high in intensity as compared to graphene shielded TiO_2. This explains the effective shielding of TiO_2 using PLAL. The O1s spectrum was de-convoluted into three peaks as shown in Fig. 4.34(c). The contextual description of this de-convoluted peaks is as follows: the peak located at 531.4 eV is attributed to metal oxygen bond (i.e Ti-O) [164], at 531.9 eV is associated with carbonate (CO_3^{2-}) [165] and the chemisorbed oxygen ($O_2(H_2O)$) is linked with 533.0 eV binding energy peak [166] . The high resolution XPS C1s spectra are shown in Fig. 4.34 (d). To investigate the type of carbon bonding present in the composite, the C1s peak is de-convoluted into five Gaussian components: (i) The sp^2 bonded carbon (C–C) (284.8 eV), (ii) sp^3-hybridized carbon atoms(C-C) (285.5 eV) [161], (iii) the C of the C-OH bonds (285.9 eV) [167], and carbon atoms bonded to one and two oxygen atoms, because electronegative oxygen atoms induce a positive charge, on a carbon atom which corresponds to: (iv) C=O [161] or epoxy/hydroxyl (C–O) (287.0 eV) [168] and (v) O—C==O species (289.9 eV) [161].

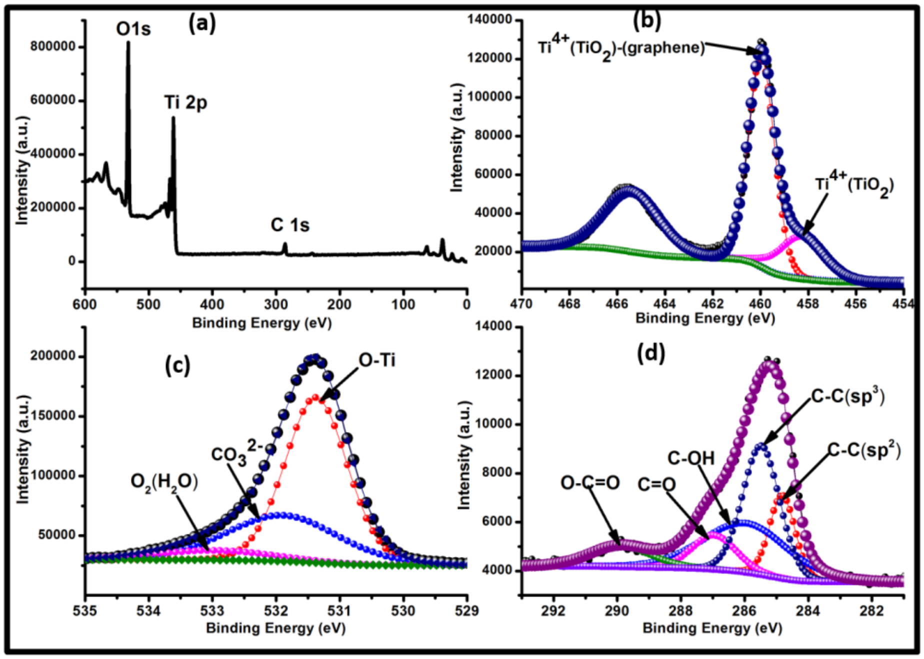

Figure 4.34 XPS Analysis of G@(3%)-TiO_2 nanohybrid

4.3.6 Photovoltaic performance analysis

In order to investigate the effect of graphene concentration on the performance of the synthesized nanocomposite, three different solar cells based on synthesized nanohybrid were fabricated. For comparison, we also fabricated the DSSC based on the TiO_2 NP. The current density-voltage (J-V) response is presented in figure 4.35. The values of open circuit voltage (Voc), short-circuit current (Jsc), Fill Factor (FF) and energy conversion efficiency for the cells. Using the parameters are shown in table 4.3, A DSSC based on a TiO_2 NP exhibited a Jsc of 0.86 $mAcm^{-2}$, Voc of 0.1837 V, an FF of 0.2785 and an efficiency of 0.5507 %. G@ (3%)-TiO_2 based DSSC resulted in greatly improved performance with Jsc of 1.357 mA, Voc of 0.5558V, an FF of 0.4047 and eff of 3.8149%.

The efficiency was significantly improved from 0.5507 % to 3.8149 % corresponding to 592.47 % improvement. G@ (16%)-TiO_2 also has better performance than other nanohybrid (G@ (16%)-TiO_2 and G@ (50%)-TiO_2). Generally comparing with TiO_2 NP, the Jsc value was improved in G@ (3%)-TiO_2 and G@ (16%)-TiO_2 nanohybrid but was reduced in G@ (50%)-TiO_2 nanohybrid. The Voc, FF, and efficiency were improved in all the synthesized nanohybrid. This shows that the introduction of the graphene into TiO_2 matrix improved the photovoltaic performance parameters of the DSSC. Since Graphene has an electron mobility of 10^4 cm^2/Vs at room temperature [169] its incorporation would enhance electron transfer through the G@k-TiO_2 network as well as the effective charge separation and resultant suppression of recombination of the excited electrons with the oxidized dye and the redox electrolyte [170]. Other reasons could be the TiO_2 nanoparticles are well anchored on the 2D graphene as shown in the TEM image, so there is easy transfer of photo-induced electrons to the graphene from TiO_2 and some reports indicate that contribution of graphene increase the pore volume thereby enhancing the diffusion of electrolyte in the cell [171][172]. Since the Voc was obtained from the difference between the redox potential of the electrolyte and the Fermi level of the photoanode rather than the device structure [173] and the apparent Fermi level of TiO_2 was not affected by the incorporation of graphene since graphene is a zero band material [170]. Improvement in Voc is due to increase of photo-excited electrons leading to further shift in the quasi-Fermi energy level towards the CB of TiO_2. Modification of potentials at the photo and counter electrodes interface with the G@k-TiO_2 nanocomposite can also affect the V_{OC} of the device [174]. It was observed that the increase in the concentration of graphene from the optimum concentration reduces the J_{SC} and V_{OC} values. This accounts for 51.34 % and

79.06 % decrease in photo-conversion efficiency with respect to G@(16%)-TiO_2 and G@(50%)-TiO_2 nanohybrid. This depreciation in performance could be attributed to the following: A downshift of the potential band edge of TiO_2 conduction band, formation of graphene cobweb inside the TiO_2 matrix obstructing fast charge collection at the electrode due to formation of charge trap sites [175][174] and decrease in electron transport and diffusion due to degradation in the crystallinity leading to charge transport resistance minimizing the number of photo-excited electrons transferring from the dye molecules to the photo anode[176]. Hence, incorporation of a moderate amount of graphene into TiO_2 is needed for effective photocatalytic property enhancement. In order to get deep insight to the interfacial charge transfer process within the fabricated DSSC, the electrochemical impedance spectroscopy (EIS) is used to investigate the charge transfer at the platinum counter electrode of DSSCs, recombination of electrons at the electrolyte-TiO_2 interface and electron diffusion in the electrolyte.

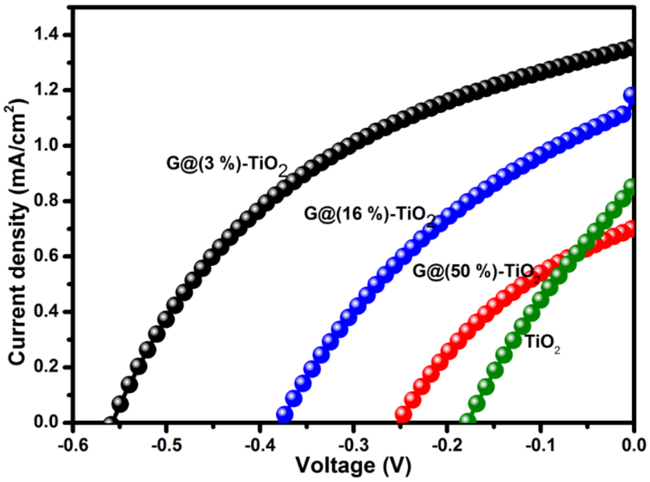

Figure 4.35 Current density-Voltage curves of TiO_2, G@(50%)-TiO_2, G@(16%)-TiO_2 and G@(3%)-TiO_2

The Nyquist plot of the DSSCs based on the G@k-TiO_2 nanocomposite photoanode obtained as shown in Fig. 4.36. It has been reported that the low-frequency response reflects the Warburg diffusion process of I/I^{3-} in the electrolyte, the middle-frequency region is associated with charge transfer and recombination at the TiO_2-dye-electrode interface and the high-frequency response is due to the charge transfer at the Pt counter electrode [172]. Since the DSSCs are fabricated with the same electrolyte, counter electrode, and dye but photoanode with different concentration of graphene, the photovoltaic performance depends on the Rct values.

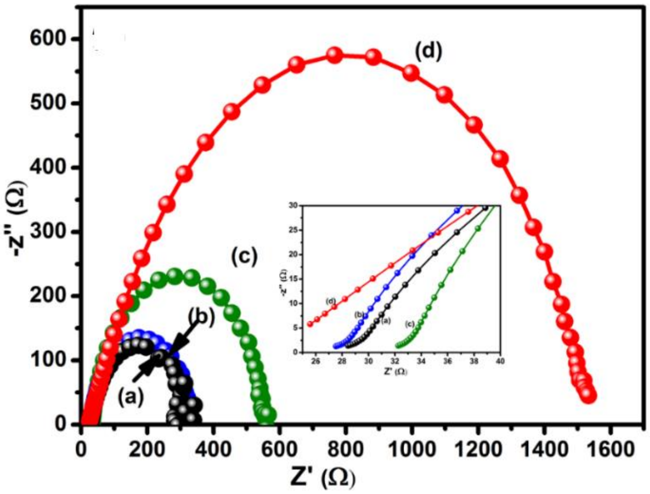

Figure 4.36 EIS Spectra (Nyquist plot) of G@k-TiO_2 nanohybrid (a) G@(3%)-TiO_2 (b) G@(16%)-TiO_2 (c) TiO_2 (d) G@(50%)-TiO_2

The semicircle in the middle-frequency region can be observed for the G@k-TiO_2 nanocomposite photoanode based DSSC and the electron transfer resistance is obtained from the arc of the semicircle. Photovoltaic parameters like current density, voltage and fill factor are usually affected by the charge-transfer resistance. Usually, a smaller diameter corresponds to lower interfacial resistance and reduced interfacial charge recombination. The comparison of the semicircles indicates that the diameter decreases in the order: G@ (50%)-TiO_2 > TiO_2 > G@ (16%)-TiO_2 > G@ (3%)-TiO_2 as shown in figure 4.36. Hence, the decrease in charge–transfer resistance is in accordance with the short-circuit current density value obtained from the DSSC. This suggests charge transfer resistance can be reduced at the TiO_2-G-dye-electrolyte interface with a moderate amount of graphene. This is because interfacial charge transfer is facilitated and charge recombination is reduced by 2D graphene. In particular, the G@ (3%)-TiO_2 has the smallest interfacial resistance implying the fastest interfacial electron transfer and high energy conversion efficiency. However, an increase of graphene concentration (from 3 % to 16 %), the interfacial resistance increases a little and still lower than the Rct value of TiO_2 NP but further increase in graphene concentration(from 16% to 50 %), the Rct value became higher than that of TiO_2. High interfacial resistance causes high charge recombination leading to low efficiency.

Table 4.3 Parameters obtained from the G@k-TiO_2 based DSSCs

Samples	**V_{OC} (V)**	**J_{SC} (mA/cm^2)**	**FF**	**η %**	**R_{CT} (kΩ)**
TiO_2	**0.1837**	**0.86**	**0.2785**	**0.55**	**0.51**
G@(3%)-TiO_2	**0.5558**	**1.36**	**0.4047**	**3.82**	**0.26**
G@(16%)-TiO_2	**0.3792**	**1.13**	**0.3459**	**1.86**	**0.30**
G@(50%)-TiO_2	**0.2520**	**0.71**	**0.3589**	**0.80**	**1.49**

The higher graphene concentration results in poor electron transport and diffusion because the crystallinity of TiO_2-NPs. Higher graphene concentration can also reduce the light harvesting capability of the sensitizing dye which decreases the number of photogenerated electrons under illumination[172]. This is the reason why the photocurrent became lower than that of TiO_2. In general, based on the EIS studies, in order to enhance the performance of TiO_2-NPs based DSSC by reducing charge carrier recombination, a moderate concentration of graphene is needed in TiO_2 matrix.

4.3.7 Photocatalytic activity analysis

The activity of the G@k-TiO_2 nanohybrid was investigated in the photocatalytic decomposition of methyl orange (MO) used as probe molecule under UV-Vis solar spectrum. As shown in figure 4.37(a), in the absence of any photo-catalyst the MO dyes are very stable. It was clear that the synthesized G@ (3%)-TiO_2 exhibited an enhanced degradation rate and the degradation efficiency was higher than that of TiO_2. This is mainly because of some aforementioned reasons that enhanced its performance in DSSC. These reasons include enhanced charge carrier transport, improved crystallinity and reduced charge transport resistance.

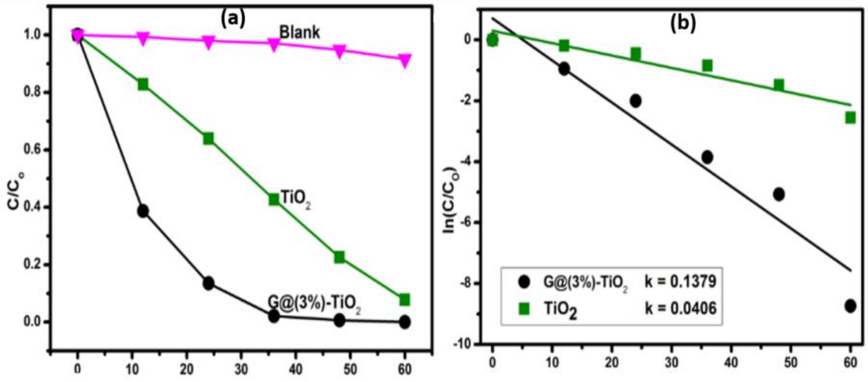

Figure 4.37 (A) Photo-degradation of MO by G@(3%)-TiO_2 and TiO_2 (B) First order kinetics of MO degradation by G@(3%)-TiO_2 and TiO_2

The photoactivity was further investigated by plotting ln(C/Co) against time in figure 4.37(b) shows the decomposition kinetics follows the linear profile. Hence, using the classical equation:$\ln\left(\frac{C}{Co}\right) = -w.t$, where w is the so called degradation rate constant. The presented w values which represent a good measurement of the overall Photo degradation rate is shown in figure 4.37(b) from fitting curves of the data for a period of 0 - 60 min. TiO_2 has 0.0406 min^{-1} and G@k-TiO_2 Nano hybrid with k = 0.1379 min^{-1} which shows there is 239.66 % increase in the degradation rate after addition of 3 % graphene concentration. The amount of MO dye that was removed can also be estimated by the depreciating absorption curve. Therefore, the UV-Vis absorbance spectrum of MO dye at different time intervals after removal of G@(3%)-TiO_2 Nano hybrid is shown in figure 4.38(a), this is used to determine the amount of MO dye removed at a specific time interval.

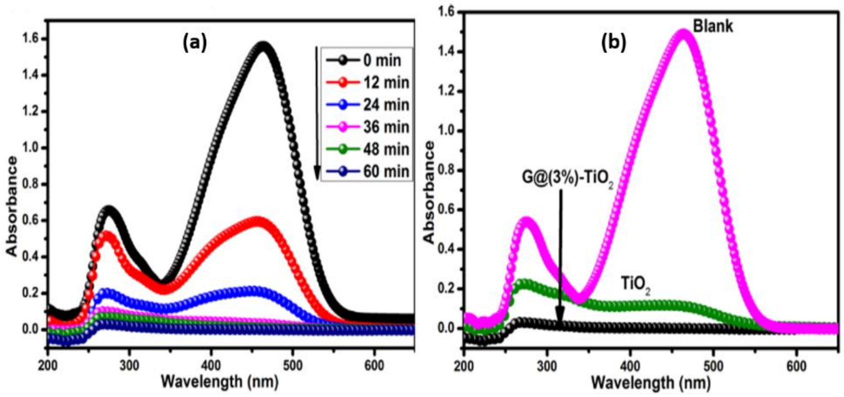

Figure 4.38 (a) Absorption spectra of MO dye degraded under UV-Vis light irradiation using G@(3%)-TiO_2 nanohybrid (b) Absorption spectra of MO solution after 60 mins of irradiation with G@(3%)-TiO_2 and TiO_2.

It was confirmed that G@ (3%)-TiO_2 Nano hybrid was so active that at 24 min of reaction about 53% of MO dye has been removed and the absorbance peak was blue shifted in stepwise average of 3 nm in both the UV and Vis absorption peak of MO. Hence, the broadening of the peak increases as the time of irradiation increases. The enhancement in degradation activity was also confirmed by the absorption spectrum of MO solution after 60 min activity of the TiO_2 and G@(3%)-TiO_2 nanohybrid as shown in figure 4.38(b). The result obtained shows that 99.64 % and 89.07 % of MO was degraded when G@(3%)-TiO_2 Nano hybrid and TiO_2 reacts with MO dye in water for 60 min.

4.3.8 Charge transfer mechanism in the solar applications

In figure 4.39, the graphene sheet serves as a bridge for electron transfer. This increases the acceleration of the photo-induced electrons. Under illumination in the DSSC, the photogenerated electrons from the dye move to the conduction of TiO_2. Since the TiO_2 NP is homogeneously dispersed to the surface of the graphene sheets, the electrons are therefore collected by the graphene sheets network. The electrons in the graphene sheets are then transferred to the FTO electrode, therefore, reducing charge recombination in TiO_2 NP. Hence, the electron generated in the DSSC is maintained within the conductive path via the presence of graphene sheets at the surface of TiO_2 NP. In the photo-degradation process, the electrons react with oxygen molecules to form superoxide radical anions (a). The hydroxyl groups traps the holes to yield hydroxyl radicals (b). The superoxide radical anions are protonated to generate highly reactive H_2O_2 molecules and hydroxyl radicals (c) and the methyl orange dye in water are oxidized by hydroxyl radicals to form H_2O and CO_2.

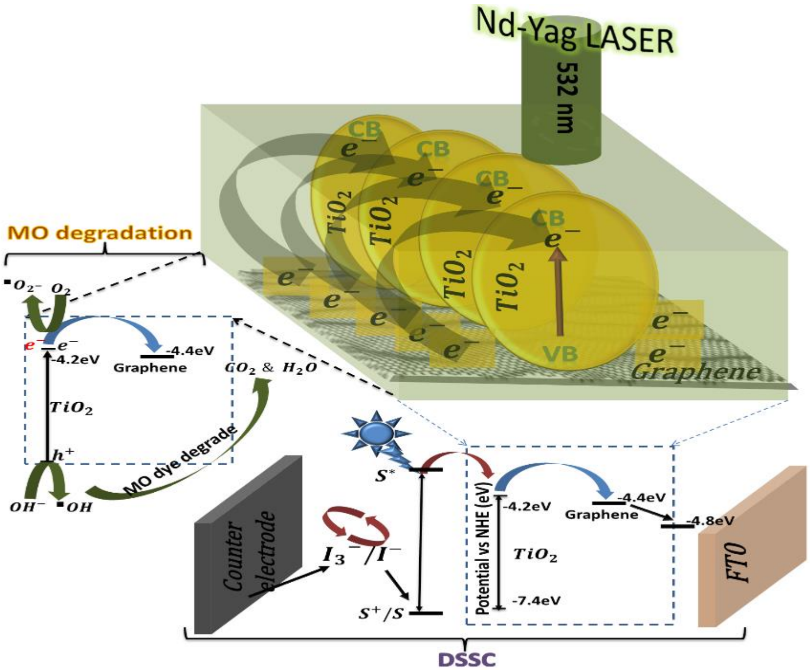

Figure 4.39 The Laser Ablation mechanism and its relation with DSSC and MO degradation mechanism

4.4 The TiO_2-SiC nanocomposite

4.4.1 Structural analysis of TiO_2-SiC nanocomposite

The XRD of SiC, TiO_2, and T-SiC composite is as shown in figure 4.40. The indexed XRD pattern of SiC indicates it has hexagonal phase (6H-SiC) with lattice parameters of a = 0.308 nm and *c* = 1.509 nm (JCPDS No. 29-1128)[177][178][122]. Although SiO_2 peak appears at 2θ=29.14^o which is indexed to (040) plane. This peak disappears in all the T-SiC nanocomposite due to its low intensity as compared with SiC and TiO_2 peak. The indexed TiO_2 nanoparticle with anatase phase (JCPDS 211272) appears in all the nanocomposites.

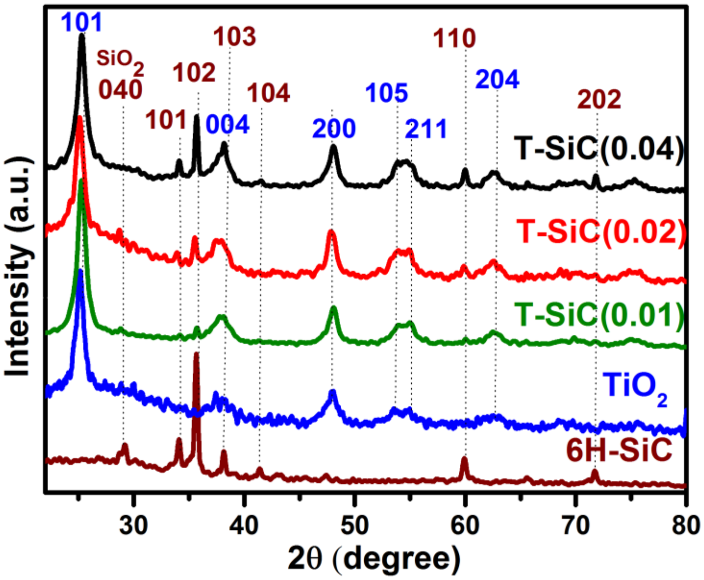

Figure 4.40 XRD pattern of TiO_2, 6H-SiC, T-SiC-10, T-SiC-20 and T-SiC-40

The presence of SiC improves the crystallinity of TiO_2 due to decrease in the roughness of the nanocomposites XRD pattern. However, in the synthesized T-SiC nanocomposites, it was observed that the number of SiC peaks indexed with (101), (103), (110) and (202) planes appears in the nanocomposites. The intensity of the peaks increases as the concentration of SiC increases in the T-SiC nanocomposites and they became well pronounced in the T-SiC-40 nanocomposite. Also observed is the perfect overlap between the (004) plane of TiO_2 and (103) plane of SiC which explains there is interaction in between the lattice of TiO_2 and SiC in the nanocomposites.

4.4.2 Raman spectra analysis of TiO_2-SiC nanocomposite

The Raman spectra of TiO_2, 6H-SiC, and synthesized T-SiC nanocomposite are shown in figure 4.41 In the Raman spectra of TiO_2, the Raman peak at 148 cm^{-1}(Eg) is associated with O-Ti-O bond bending mode, the 393 cm^{-1}(B1g) relates to oxygen atom liberation along the c-axis out of phase, At 513 cm^{-1}(A1g) and the 635 cm^{-1}(Eg) band are the Ti-O stretching mode All this bands confirms the presence of anatase phase [137][138].

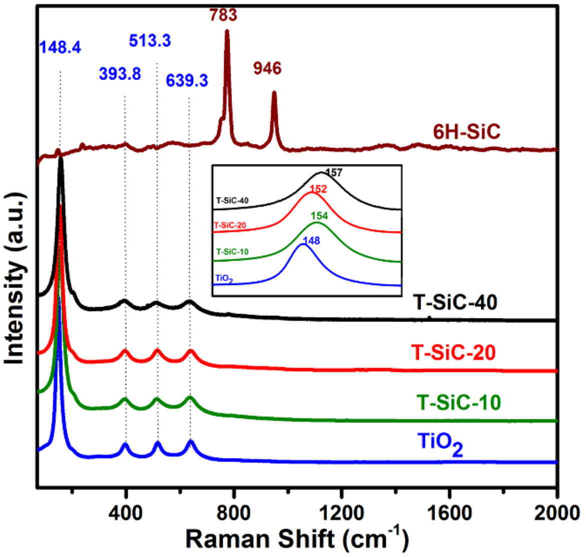

Figure 4.41 Raman Spectra of TiO_2, 6H-SiC, T-SiC-10, T-SiC-20 and T-SiC-40

The SiC Raman spectra show two Raman peaks present at 783 cm^{-1} and 946 cm^{-1} which are signatures of the characteristics transverse and longitudinal mode[179] associated with 6H-SiC. The 6H-SiC Raman peaks were not observed in the synthesized T-SiC nanocomposite. The change observed in the nanocomposite due to the presence of SiC is the frequency shift of ~2-6 cm^{-1} observed in the 148 cm^{-1} band of TiO_2 as shown in the inset at the middle of the spectra which could be due to presence of structural defects and /or size confinement[179] [180][181] .

4.4.3 Morphology of T-SiC-10 nanocomposite

The morphology of 6H-SiC integrated TiO_2 is shown in figure 4.42. The wool-like appearance of TiO_2 was changed into a wool containing aggregates of particles which are clearly known to be 6H-SiC formed within the crystals of TiO_2. This can be described as reinforcement of TiO_2 NP with 6H-SiC in surface coupled semiconductors of the nanocomposite. In order to confirm the image obtained in FESEM image, the TEM image shown in figure 4.42 (b) which shows the presence of large particles integrated within populated smaller particles. The larger particles have a lower concentration than the smaller particles because a low percentage weight of 6H-SiC (~10%) is present in the synthesized T-SiC-10 nanocomposite. The large particle is known to be 6H-SiC and the smaller particles represents of TiO_2 nanoparticles. Therefore, a perfect integration of 6H-SiC into the lattice of TiO_2 was well accomplished during the Pulsed laser ablation.

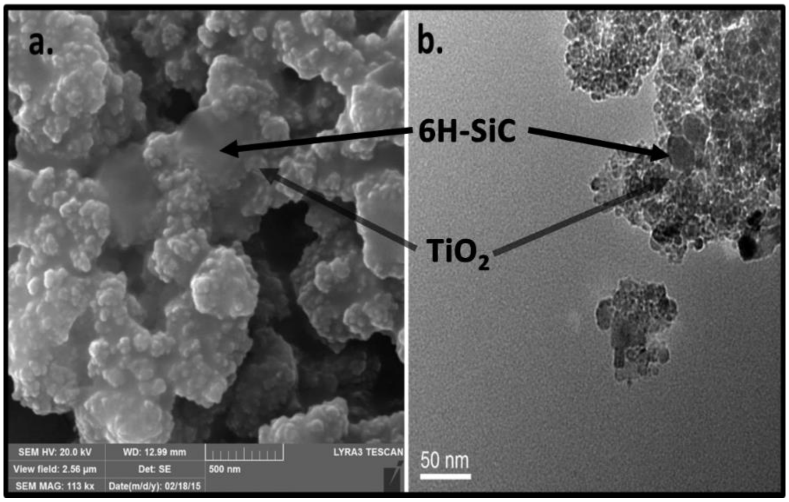

Figure 4.42 (a) FE-SEM Image and (b) TEM of T-SiC-10 nanocomposite

4.4.4 Optical analysis of T-SiC nanocomposite

The Absorption spectra and the corresponding tauc plot of 6H-SiC, TiO_2 NP and synthesized T-SiC nanocomposites (T-SiC-10, T-SiC-20 and T-SiC-40) are shown in figure 4.43(a) and (b) respectively . The SiC has a strong absorption in the deep UV–region at the absorption edge of 260 nm with a band gap of ~3.9 eV. However, the band gap of 3.17 eV is reported for the SiC in our previous work [122]. Therefore the broadened band gap is due to the presence of SiO_2 created on the surface of SiC after calcination. The TiO_2 nanoparticle has strong absorption at 324 nm with a band gap of ~3.32 eV. The T-SiC-10, T-SiC-20 and T-SiC-40 nanocomposites show absorption peak at 322, 320 and 315 nm which correspond to a band gap of 3.4, 3.42 and 3.46 eV respectively. Therefore, compared to TiO_2, there is a blue shift in the absorption peak due to the effect of deep absorption edge of SiC on absorption peak of TiO_2.

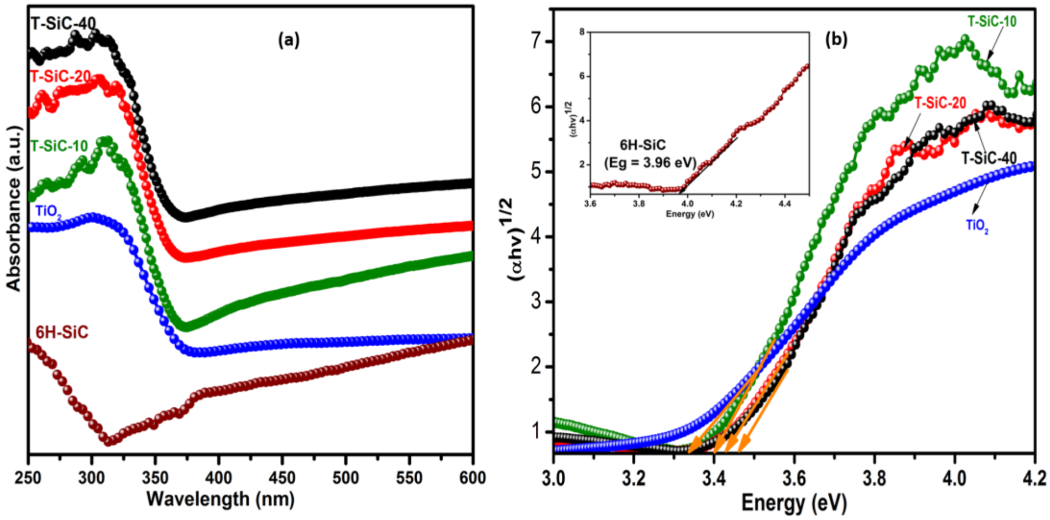

Figure 4.43 (a)Absorption spectra (b) Tauc plot of TiO_2, 6H-SiC, T-SiC-10, T-SiC-20 and T-SiC-40

Figure 4.44 shows the FTIR spectra of TiO_2, 6H-SiC, and T-SiC. At 790 cm^{-1} is a strong peak which corresponds to Si-C bond stretching mode[182]. This stretching mode present in all the synthesized T-SiC nanocomposite enhanced the TiO_2 stretching mode at this region. The 1104 cm^{-1} band assigned to the asymmetric Si-O-Si stretching vibration was also observed for the bond between the Silicon in 6H-SiC and Oxygen in TiO_2 NP. Also around this region is the C–H_2 bond within $SiCH_2$ wagging mode because 1104 cm^{-1} is broadened in all the synthesized T-SiC nanocomposite. The presence of the 1380 cm^{-1} peak is also observed in the T-SiC-10 nanocomposite, but absent in another nanocomposite such as T-SiC-20 and T-SiC-10 correspond to Ti-O-Ti bond in TiO_2[183]. This is because the quantity of 6H-SiC in the T-SiC-10 nanocomposite is very small, less than 12%, for TiO_2 bond to appear and become dominant. The band that appear at 1633 cm^{-1} was assigned to the bending vibration of the O–H bond of chemisorbed water during laser ablation and the broadband around 3377 cm^{-1} was due to the stretching mode of the O–H bond of free water which appears in TiO_2 and all the synthesized T-SiC nanocomposite due to presence of SiO_2.

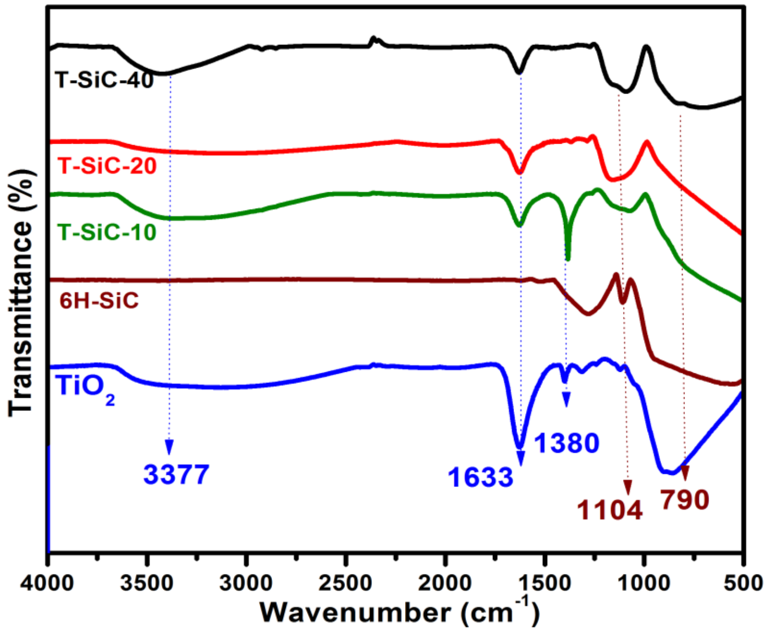

Figure 4.44 FTIR of TiO_2, 6H-SiC, T-SiC-10, T-SiC-20 and T-SiC-40

4.4.5 XPS analysis of T-SiC nanocomposite

XPS analysis was performed to investigate the chemical state of T-SiC nanocomposite. Figure 4.45 shows the high resolution spectra of Ti, Si, O and C found in the survey spectrum of T-SiC nanocomposite .The high resolution of Ti 2p spectrum demonstrated two peaks at 457.4 eV (Ti $2p_{3/2}$) and 463.4eV (Ti $2p_{1/2}$) which confirms the existence of Titanium. The Ti $2p_{3/2}$ was deconvoluted into two peaks at 455.9 eV and 458.0 eV which represents TiO [184] and TiO_2 [185] respectively. The Si 2p spectrum obtained was fitted into three characteristic peaks of Silicon state at 101.1eV, 101.9 eV and 102.8 eV which correspond to SiC[186], SiC-O [187]and TiO_2-SiO_2 [188]respectively. The O1s peaks were deconvoluted into two Gaussian peaks at 529.1 eV and 531.67 eV which are signatures of oxygen states in metal oxide(TiO_2 and SiO_2) and carbonates[189]. The high-resolution spectrum of C1s spectrum shows three small fraction peaks at 283.4 eV, 285.0 eV and 287.2 eV which are associated with carbide (SiC)[190], C-C and C with O bond[189]. Hence during Laser ablation, there is an exchange of elements between 6H-SiC and TiO_2

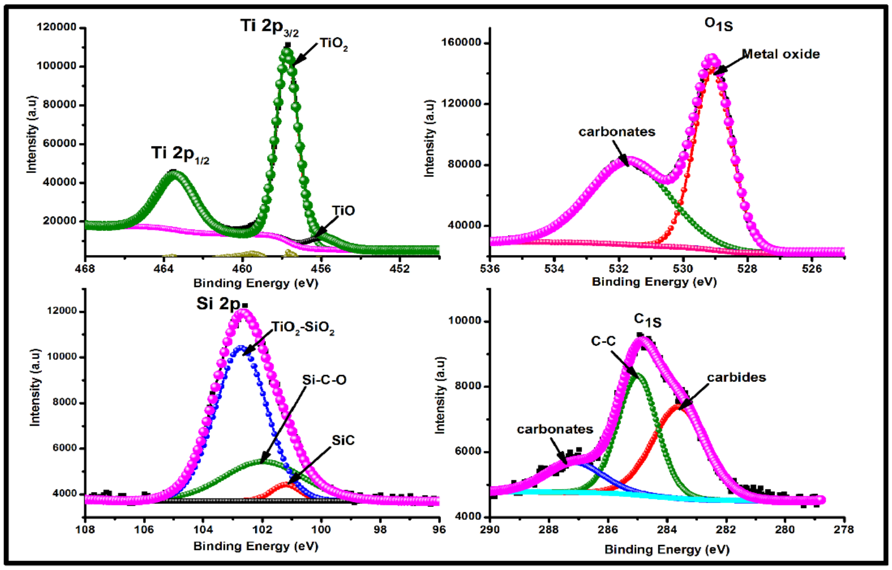

Figure 4.45 XPS spectral analysis of T-SiC nanocomposite showing deconvoluted peaks in the high resolution of the elements present (Ti, Si, O and C)

4.4.6 Photovoltaic performance analysis

The Current density-voltage (J-V) curves of TiO_2 and synthesized T-SiC nanocomposite are as shown in figure 4.46. Table 4.4 summarized the Open circuit voltage (Voc), Short circuit current, maximum current and voltage measured from these curves which are used to determine the Fill factor and Efficiency of the solar cells fabricated with these materials. It was observed that the Voc of the nanocomposite reduces the quantity of 6H-SiC increases. The Jsc of the T-SiC-10 is equal to that of TiO_2 as the quantity of 6H-SiC is very small (< 2%) in the matrix of the nanocomposite and the T-SiC-20 shows a higher Isc. This might be because the quantity of 6H-SiC is high enough to improve the pore size of TiO_2. T-SiC-40 nanocomposite shows a relatively very low Voc and Jsc as compared to TiO_2.

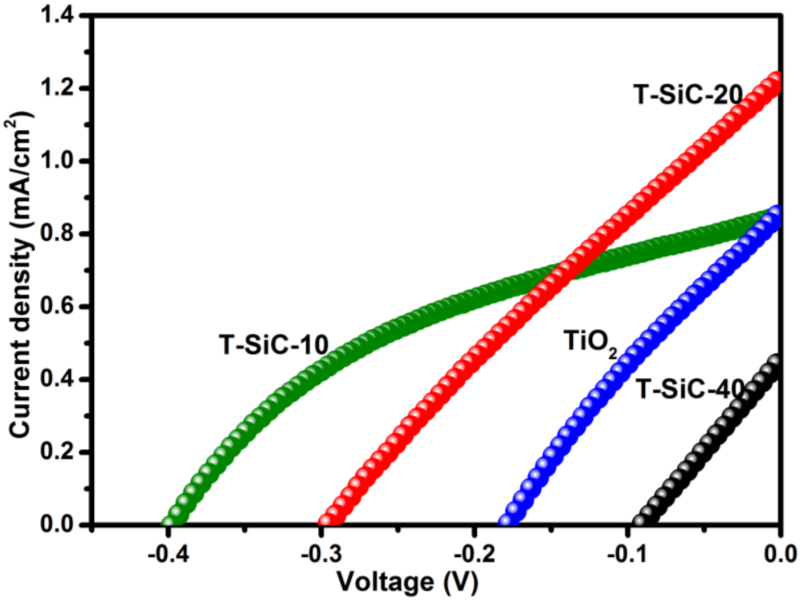

Figure 4.46 J-V curve of TiO_2, 6H-SiC, T-SiC-10, T-SiC-20 and T-SiC-40 based DSSC

This might be because the percentage of 6H-SiC is too high therefore reducing electron drift from the valence band to conduction band in the nanocomposite. The efficiency increases gradually from 0.55 % to 1.65 % when 10 wt% of SiC was introduced into TiO_2.

And then decreases to 0.12% when 40 wt% of SiC was present. The T-SiC-40 shows the lowest efficiency of 0.12 %. This means excessive SiC has led to decreased Jsc, Voc, and efficiency. This can be attributed to increasing in recombination of photogenerated electron and holes at the T-SiC/dye/electrolyte interfaces. To further investigate the charge recombination process, electrochemical impedance spectroscopic (EIS) measurement was conducted under constant illumination under a bias of their relative open circuit voltage.

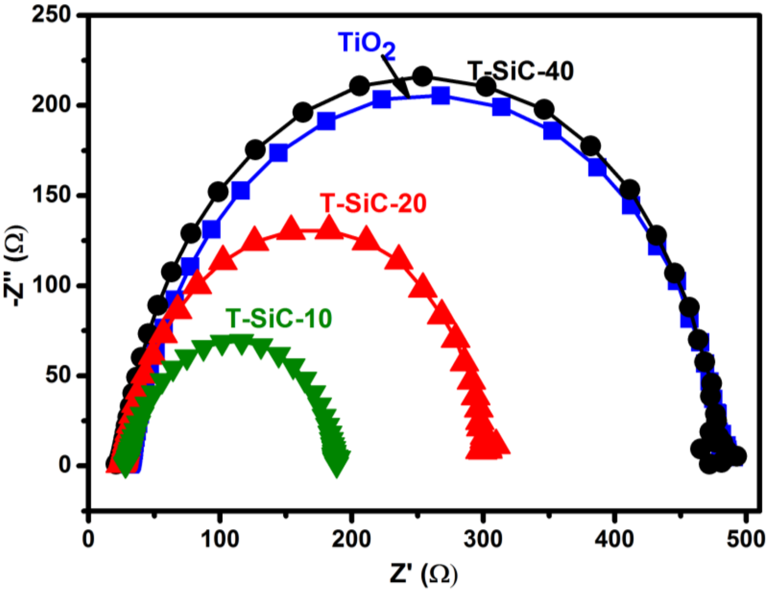

Figure 4.47 Nyquist plot of TiO_2, 6H-SiC, T-SiC-10, T-SiC-20 and T-SiC-40 based DSSC at V_{OC}.

Figure 4.47 are the Nyquist plots and the corresponding simplified equivalent circuit for the DSSCs, respectively. The diameters of the large semicircles observed in the Nyquist plot can be used to measure the charge transfer resistance (Rct) in TiO_2 and all the T-SiC nanocomposite. Since TiO_2 and all the T-SiC nanocomposite have the same interface with the counter electrode/ electrolyte in the DSSC, therefore, all other resistance observed that can be observed remain the same. The Rct values from the photoelectrode synthesized from TiO_2, T-SiC-10, T-SiC-20, and T-SiC-40 are 463 Ω, 181.6 Ω, 292.3 Ω and 465 Ω respectively as listed in Table 4.4. Hence, the Rct values reduce the concentration of 6H-SiC reduces from 40 wt. % to 10 wt. %. This indicates that a faster recombination occurs in T-SiC-40 nanocomposite due to the fact that electron gets retarded when oxidation resistance is too high due to the presence of high quantity of 6H-SiC. The charge transfer resistance changes accordingly with V_{OC} values and the efficiency of the DSSC. Hence, The T-SiC-40 shows the lowest efficiency of 0.12% and T-SiC-10 shows the highest efficiency of 1.65% which is more than that of TiO_2 because (i) The 6H-SiC introduced into TiO_2 matrix has excellent oxidation and corrosion resistance[191][192]. Such that, when the concentration of 6H-SiC is too high it can cause electron retardation in TiO_2 matrix which is the case of T-SiC-40 showing low performance.(ii) 6H-SiC used as a starting material is in micron size and after laser ablation the SiC in the nanocomposite has reduced in size that enhances its catalytic activity [193]–[197]. (iv) The TiO_2 nanoparticles are reinforced by SiC in the nanocomposite matrix[198]

Table 4.4 Parameters of the DSSCs with TiO_2, T-SiC-10, T-SiC-20 and T-SiC-40

Sample	J_{SC} (mA/cm^2)	Voc (V)	FF (%)	η (%)	Rct (kΩ)
TiO_2	**0.852**	**0.1787**	**0.2932**	**0.56**	**0.48**
T-SiC-10	**0.844**	**0.3951**	**0.3969**	**1.65**	**0.18**
T-SiC-20	**1.232**	**0.2949**	**0.2748**	**1.25**	**0.29**
T-SiC-40	**0.444**	**0.0884**	**0.2355**	**0.12**	**0.47**

4.4.7 Photocatalytic activity analysis

The Photocatalytic performance of TiO_2-SiC composites via methyl orange photodegradation experiments under UV-Vs light irradiation. Before photo-irradiation, the samples are kept in the solution for 30 mins so that adsorption equilibrium can be reached. The photocatalytic activity of the composite catalyst is shown in figure 4.48(a). Stability of MO dye was confirmed when the MO dye is exposed to the solar irradiation without a catalyst. The T-SiC-40 and T-SiC-20 shows a weak activity in which ~13% and 27 % respectively of MO is decomposed after irradiation for 24 min. Moreover, only 8 % and 22 % MO was removed when exposed to SiC and TiO_2 at the same irradiation time. The T-SiC-10 composite shows a significantly enhanced activity for the degradation of MO as shown in figure 4.48(b)

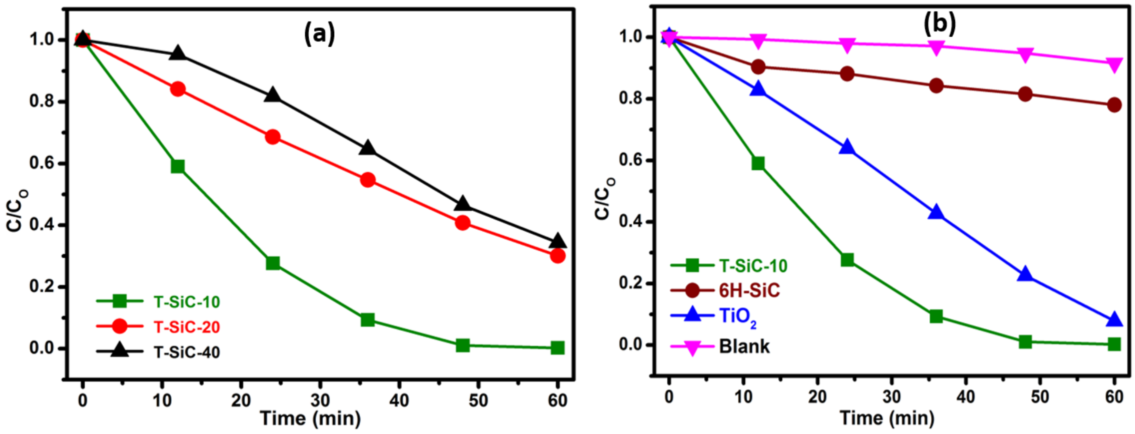

Figure 4.48 Photo-degradation of MO (A) T-SiC-10, T-SiC-20 and T-SiC-40 (B) TiO_2, 6H-SiC and T-SiC-10

This corresponds to the removal of 77 % of MO for the same irradiation time. The photodegradation activity increases from T-SiC-40 to T-SiC-10 in the same manner with the way SiC content reduced. The highest activity is obtained for T-SiC-10 composite in which 77% of MO was removed at 24 min and a removal of 96% is reached after 48 min. The T-SiC-20 and T-SiC-40 has a low performance in the degradation activity, but it is still better that SiC due to the presence of TiO_2. T-SiC-10 has a much better activity than TiO_2 because a moderate amount of SiC is needed for photocatalytic activity improvement. This might be due to visible light response shown in the absorption spectrum. In order to have a much better understanding of the reaction kinetics, the experiment data are fitted by a first order model and the results are shown as an inset in fig 4.49(a and b). The T-SiC-10 photocatalyst exhibits the highest rate constant of 0.1024 min^{-1} which is 20 and 3 times larger than those of individual SiC(0.0038) and TiO_2 (0.0406) respectively. With respect to T-SiC-20 and T-SiC-40 nanocomposite, the rate constant of T-SiC-10 is 4 and 5 times larger than respectively. The observed values of the kinetic rate constant decrease proportionally to the increase in percentage weight of SiC which demonstrate that the existence of SiC and TiO_2 heterostructure gives to improved performance.

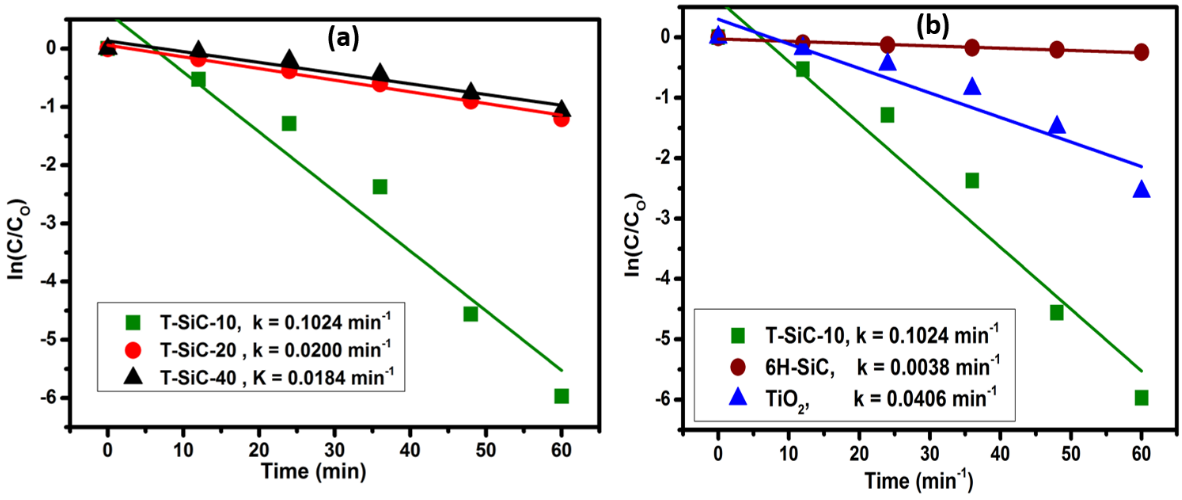

Figure 4.49 Linear fit of the Photo-degradation of MO using (A) T-SiC-10, T-SiC-20 and T-SiC-40 (B) TiO_2, 6H-SiC and T-SiC-10

4.5 Comparison of the Binary nanocomposites

4.5.1 Photocatalytic performance comparison

The best composite obtained from each family of binary composite namely: TiO_2-CdS-10, TiO_2-SiC-10, and ZnO-TiO_2, TiO_2-Graphene binary nanocomposites are prepared in the same experimental condition and applied for DSSC and methyl orange degradation with the same kind of materials and the same condition. Hence, the order of the effectiveness of the composites in the photodegradation of methyl orange was compared in Figure 4.50. The result obtained shows that: At 24 min, 57%, 78%, 88% and 96% of MO dye was removed when exposed to T-ox-CdS-10, T-SiC-10, G@ (3%)-TiO_2 and ZnO/TiO_2@ (9:1) respectively. The difference in the performance shows that ZnO/TiO_2 @ (9:1) shows the best performance and T-ox-CdS-10 has the least performance. The experiment was done under UV-Vis solar irradiation which makes it difficult to compare the performance of this nanocomposite in the visible spectral region that is more desirable but more significantly at 60 mins of irradiation the order of MO decomposition changes to G@ (3%)-TiO_2 >ZnO/TiO_2@ (9:1) >T-SiC-10 > T-ox-CdS-10.This means G@ (3%)-TiO_2 has the best performance at this moment. The overtaken performance at 60 mins can be associated to the Vis absorption this sample possess which gives it extra charge carriers for MO degradation. In order to reconfirm this activity, the rate constant was also compared with the percentage decomposition as shown in figure 4.51. This confirms the order in which rate constant differs is directly proportional to the order of percentage decomposition at 60 min. Hence, T-ox-CdS-10 still has the least performance at 60 min due to the high rate of recombination which hinders it performance.

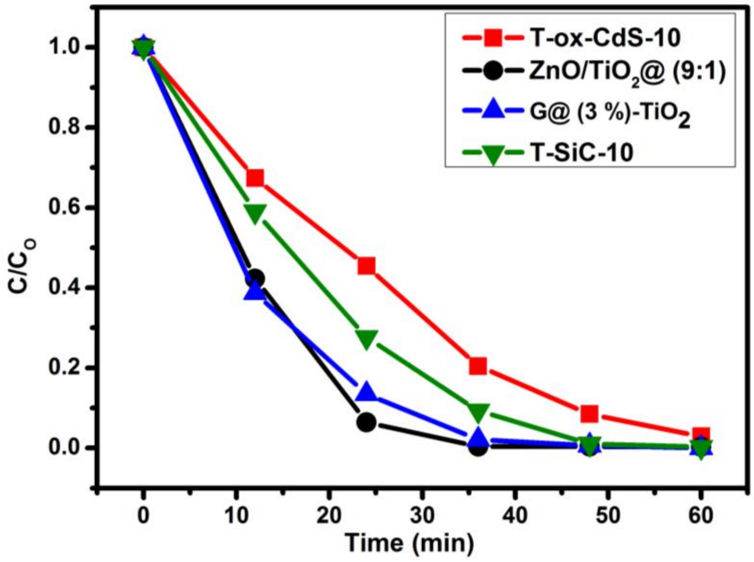

Figure 4.50 The comparison of MO reduction capability of the best binary nanocomposite (ZnO/TiO$_2$@1:9, T-ox-CdS-10, G@(3%)-TiO$_2$ and T-SiC-10)

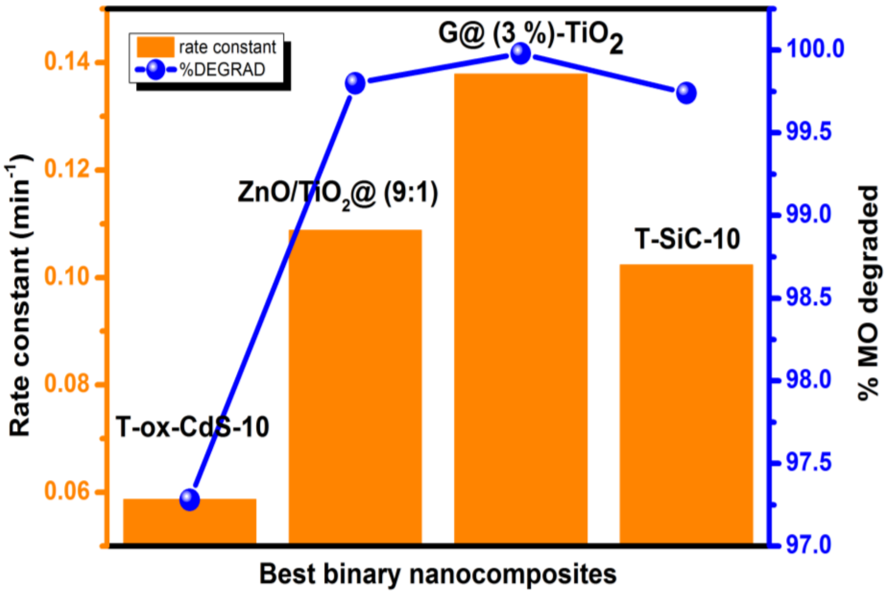

Figure 4.51 The comparison of rate constant (min^{-1}) and percentage of MO degraded (% MO degraded) of the best binary nanocomposite (ZnO/TiO$_2$@1:9, T-ox-CdS-10, G@(3%)-TiO$_2$ and T-SiC-10)

4.5.2 Photovoltaic performance comparison

The J-V curve obtained from the binary nanocomposites was also compared in figure 4.52.The short circuit current density increases in the order T-SiC-10< T-ox-CdS-10<G@ (3%)-TiO_2 <ZnO/TiO_2@ (9:1). This shows ZnO/TiO_2@ (9:1) has the highest current density based on the fact that reducing electron-hole recombination remains the most important factor affecting the current density of the dye-sensitized solar cell. The open circuit voltage increases in the order of T-SiC-10< ZnO/TiO_2@ (9:1) <G@ (3%)-TiO_2 < T-ox-CdS-10. This show T-ox-CdS-10 has the highest open circuit voltage. Hence, combining visible light absorption activity and reduced charge recombination is the major contributing factor from introducing graphene or CdS is needed to enhance the open circuit voltage of the dye-sensitized solar cell. The result obtained in the binary composite was combined and well described in figure 4.53 such that it was seen that ZnO/TiO_2@(9:1) with the highest percentage increase over TiO_2 has the least charge transport resistance, G@ (3%)-TiO_2 with the highest rate constant removes the highest percentage of MO after 60 min of solar irradiation. The photoconversion efficiency of the binary nanocomposite was compared in figure 4.50. This result shows that the ZnO/TiO_2@(9:1) has the highest photoconversion efficiency as the efficiency changes in the order: T-SiC-10< <G@ (3%)-TiO_2 < T-ox-CdS-10 < ZnO/TiO_2@ (9:1).this confirms that the reduction in charge recombination of the composite supersede visible absorption increase in the enhancement of efficiency but supersedes corrosion resistance property introduced by SiC.

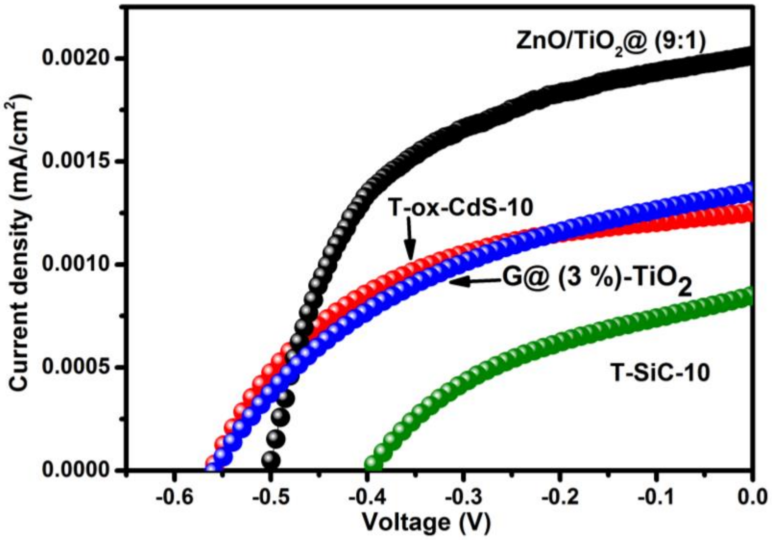

Figure 4.52 The comparison of J-V curve of the best binary nanocomposite (ZnO/TiO$_2$@1:9, T-ox-CdS-10, G@(3%)-TiO$_2$ and T-SiC-10)

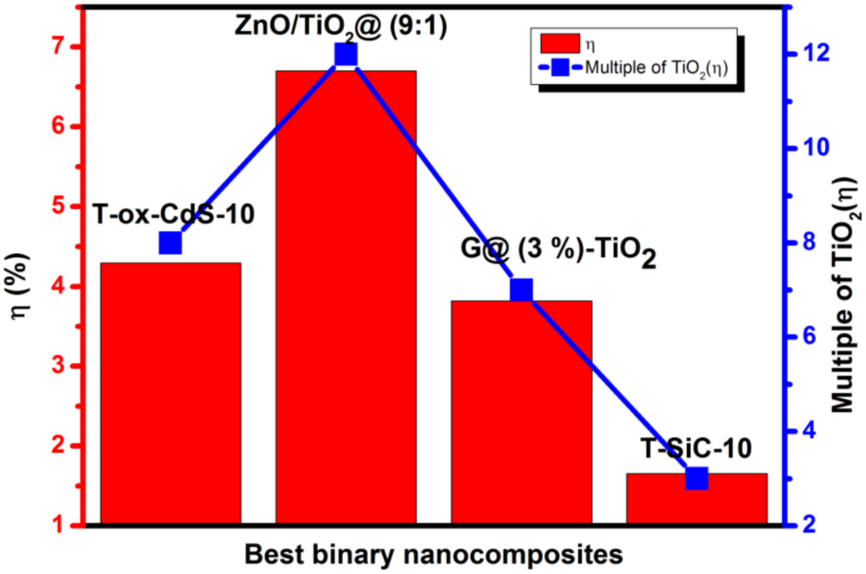

Figure 4.53 The comparison of overall efficiency and percentage of amount of percentage increase over TiO2(multiple of TiO$_2$(eff) of the best binary nanocomposite (ZnO/TiO$_2$@1:9, T-ox-CdS-10, G@(3%)-TiO$_2$ and T-SiC-10)

4.6 The Quaternary nanocomposites

The best binary nanocomposite has been successfully determined from the group of binary nanocomposites. This binary nanocomposites namely ZnO/TiO_2@9:1, T-ox-CdS-10, G@(3%)-TiO_2 and T-SiC-10) are first combined as single elements to form a quaternary nanocomposite. For example ZnO/TiO_2@9:1 + T-ox-CdS-10 + T-SiC-10 is denoted as (TZ+TC+TS). In another way, a computation described with pseudo code is also used as a channel for obtaining a quaternary nanocomposite while retaining the percentage weight used in each of the best binary nanocomposite (The pseudo code was written as follows:

```
Step 1: Q ($TiO_2$) ($TiO_2$ is common to all the binary nanocomposites)
Step 2: Compute    Q (ZnO) = Q ($TiO_2$) /9
                   Q (CdS) = Q ($TiO_2$)/10
                   Q (SiC) = Q ($TiO_2$)/10
Hence, ZnO/$TiO_2$/CdS/SiC
```

4.6.1 Photocatalytic activity analysis

The performance of the prepared quaternary nanocomposites was first investigated by investigating their photodegradation capability. However, the degradation of methyl orange dye in solution over ZnO NR, TZ+TC+TS and ZnO/TiO_2/CdS/Sic is shown in figure 4.54. A clear difference was observed in the activity of the nanocatalyst. It was observed that for irradiation time of 60 mins, the TZ+TC+TS quaternary nanocomposite is less active than ZnO NR but ZnO/TiO_2/CdS/SiC is more active than ZnO NR. This shows that, ZnO/TiO_2/CdS/SiC is a better quaternary nanocomposite compared to TZ+TC+TS nanocomposite. Therefore, it is confirmed that the pseudo code computation approach used in preparing the nanocomposite to retain the percentage weight of the base binary nanocomposite is better than direct combination used to prepare TZ+TC+TS quaternary nanocomposite.

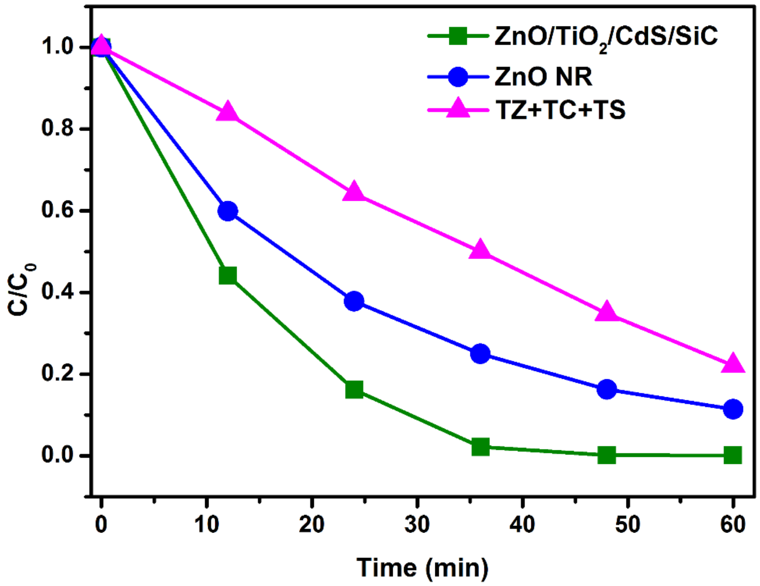

Figure 4.54 Methyl orange (MO) degradation activity of the quaternary nanocomposite

4.6.2 Structural analysis of quaternary nanocomposite

Figure 4.55 presents the XRD pattern of ZnO/TiO_2/CdS/G, and ZnO/TiO_2/CdS/SiC nanocomposite. The XRD patterns show that only the hexagonal wurtzite structure with lattice constant a = 3.248 Å and c = 5.206 Å almost match well with the reported value for ZnO crystal (JCPDS card, No.36-1451)[199] can be identified in the quaternary nanocomposites. This result implies ZnO nanocrystal structure was retained with TiO_2, CdS, and graphene or SiC in ZnO matrix. There are no clear peaks for TiO_2, CdS, and graphene in the XRD patterns of the nanocomposite. Further analysis shows that the position of the peaks also matches with other structures. therefore Figure 4.51(a) shows the ZnO/TiO_2/CdS/G nanocomposite shows Cadmium zinc oxide($Cd_{0.05}Zn_{0.95}$)O matches well with most of the peaks and few peaks also show signature of zinc carbide(ZnC_8) and Spinel ($Zn_2(TiO_4)$).

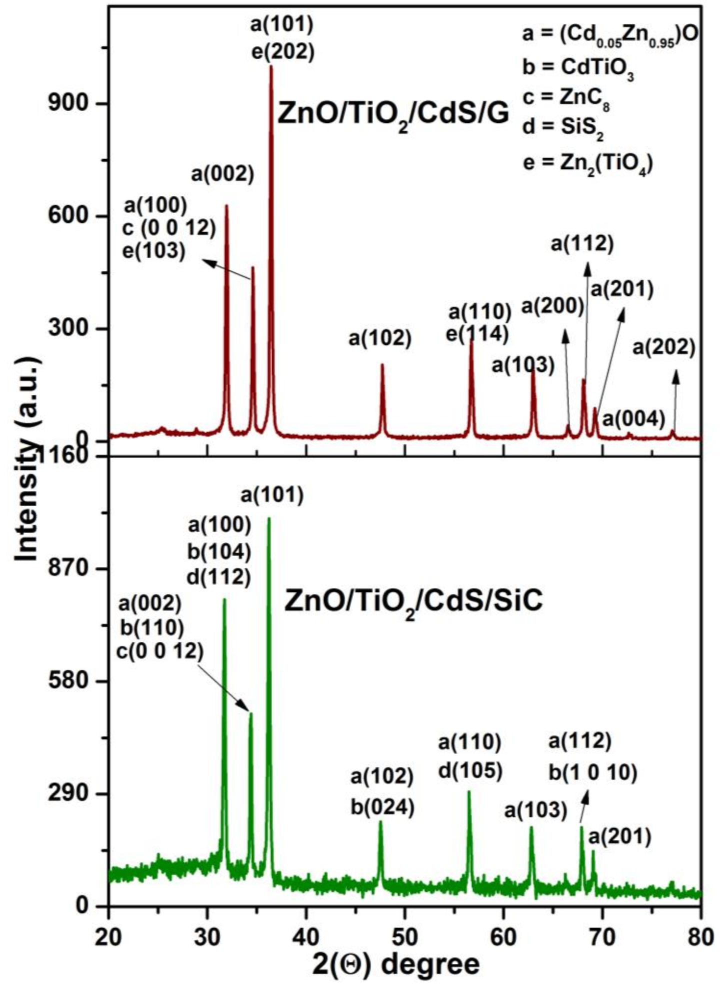

Figure 4.55 The XRD pattern of $ZnO/TiO_2/CdS/G$, and $ZnO/TiO_2/CdS/SiC$ nanocomposite

The XRD pattern of $ZnO/TiO_2/CdS/SiC$ nanocomposite is shown in Figure 4.51(b) . The diffraction pattern shows $ZnO/TiO_2/CdS/SiC$ nanocomposite is composed of $(Cd_{0.05}Zn_{0.95})O$, cadmium titanium oxide($CdTiO_3$), ZnC_8 and silicon disulfide(SiS_2). The $(Cd_{0.05}Zn_{0.95})O$, $CdTiO_3$, $Zn_2(TiO_4)$, ZnC_8 and SiS_2 are matched according to the DB card no: 01-071-5960, 00-029-0277, 01-074-6450, 00-051-0627 and 01-072-1423 respectively.

4.6.3 Raman spectra analysis of quaternary nanocomposite

The Raman spectra of ZnO/TiO$_2$/CdS/G and ZnO/TiO$_2$/CdS/SiC nanocomposite are depicted in figure 4.56. The Raman spectra of ZnO/TiO$_2$/CdS/G is more pronounced than that of ZnO/TiO$_2$/CdS/SiC. This is because the intensity of the peaks are higher and well defined. Therefore better crystallinity is observed in ZnO/TiO$_2$/CdS/G due to the presence of graphene as it was observed in the XRD pattern.

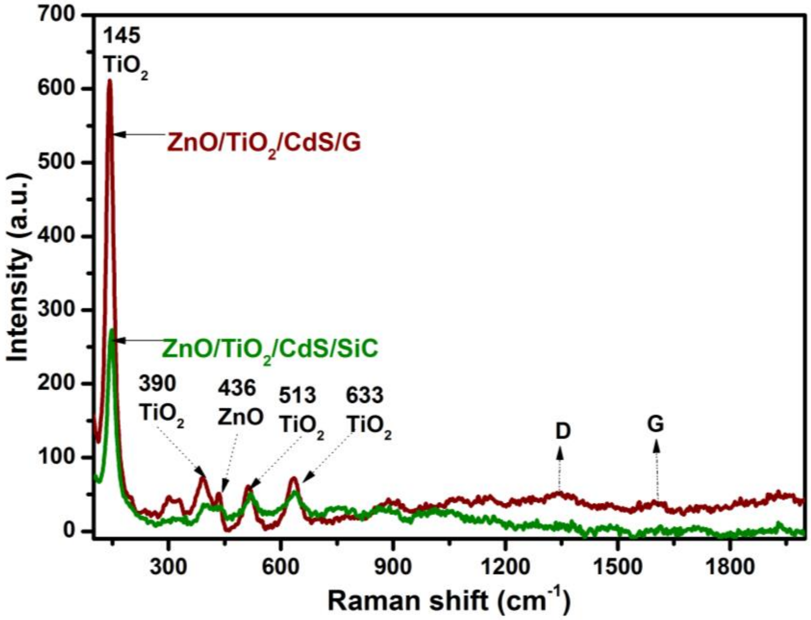

Figure 4.56 Raman spectra of ZnO/TiO$_2$/CdS/G, and ZnO/TiO$_2$/CdS/SiC nanocomposite

The E$_{high2}$ mode due to vibration of oxygen atom in ZnO lattice [136]of hexagonal wurtzite structure, Raman peak at 133.5 cm^{-1}(E$_g$), 390 cm^{-1}(B$_{1g}$) and 513 cm^{-1}(A$_{1g}$) band associated with bending mode of O-Ti-O bond, oxygen atom liberation along the c-axis out of phase and Ti-O stretching mode respectively in anatase phase TiO$_2$[137], [138], red shift of Eg band which indicates the presence of oxygen vacancies and overlap between the B$_{1g}$ band of TiO$_2$ centered at 393 cm^{-1} and the 435 cm^{-1} optical phonons of ZnO which shows interaction occur between the nanoparticles in the nanocomposite are present in

$ZnO/TiO_2/CdS/G$ and $ZnO/TiO_2/CdS/SiC$ nanocomposite. Also observed is the slight appearance of the D and G band of graphene in $ZnO/TiO_2/CdS/G$ which confirms the presence of graphene.

4.6.4 Morphology of quaternary nanocomposite

The morphology of ZnO NR, $ZnO/TiO_2/CdS/G$ is shown in figure 4.57. $ZnO/TiO_2/CdS/G$ nanocomposite shows a pod-like appearance after complete entanglement of TiO_2, CdS and graphene to the ZnO nanorods as shown in figure 4.57(a). The TEM image of ZnO/TiO_2/CdS/graphene quaternary nanocomposite is shown in figure 4.57(b). The growth of TiO_2 NP, CdS and ZnO NR on graphene sheets was confirmed in the image. This explains the reason why the graphene was not observed in the SEM image. It was evident that all the particles on the base graphene were interconnected and the surface of ZnO NR which is dominant becomes populated with spherically shaped particles that lead to its nano pod appearance in the SEM image. The crystallinity is confirmed with the HRTEM image in figure 4.57(c) which show clear fringes with a spacing of ~0.34 nm. The SAED in figure 4.57(d) shows a few diffraction spot because of surface adhesion of the nanoparticles. The morphology of $ZnO/TiO_2/CdS/SiC$ is shown in figure 4.59.In the SEM image shown in figure 4.58(a) $ZnO/TiO_2/CdS/SiC$ shows a well-compacted aggregate of the ZnO, TiO_2 and CdS particles as compared to $ZnO/TiO_2/CdS/G$ due to the presence of SiC which is known useful for reinforcement. Figure 4.58(b) shows the TEM image of $ZnO/TiO_2/CdS/SiC$ quaternary nanocomposite. The interfacial connection between the SiC, CdS, spherical TiO_2 and ZnO nanorods was clearly seen. The atomic planes were seen overlapping in the HRTEM image shown in figure 4.58(c) obtained for the quaternary nanocomposite. The fringe spacing of 0.251 nm and 0.283 was observed which correspond to TiO_2 NP and ZnO

NR. The diffraction pattern of wurtzite-type hexagonal ZnO NR was dominant in the SAED image shown in figure 4.58(d) and this is consistent with the XRD spectra. The percentage weight of the nanoparticles was almost consistent with the requirement obtained from the pseudo code. This is shown in figure 4.58(e) from the EDS spectrum ignoring the concentration of oxygen and carbon whereby Si is ~10% of Ti, Cd is ~ 10 % of Ti and Ti is ~9% of Zn.

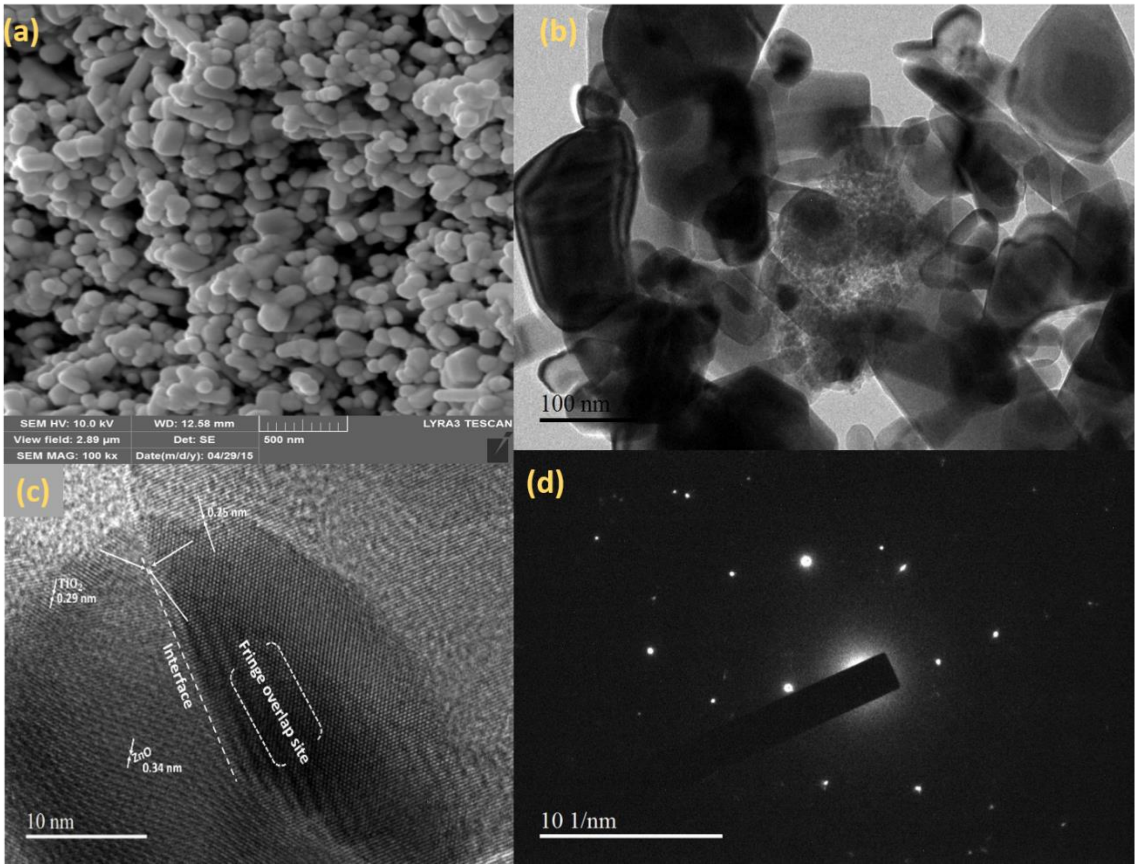

Figure 4.57 (a) FESEM image (b) TEM image (c) HRTEM image and (d) SAED of ZnO/TiO_2/CdS/G nanocomposite

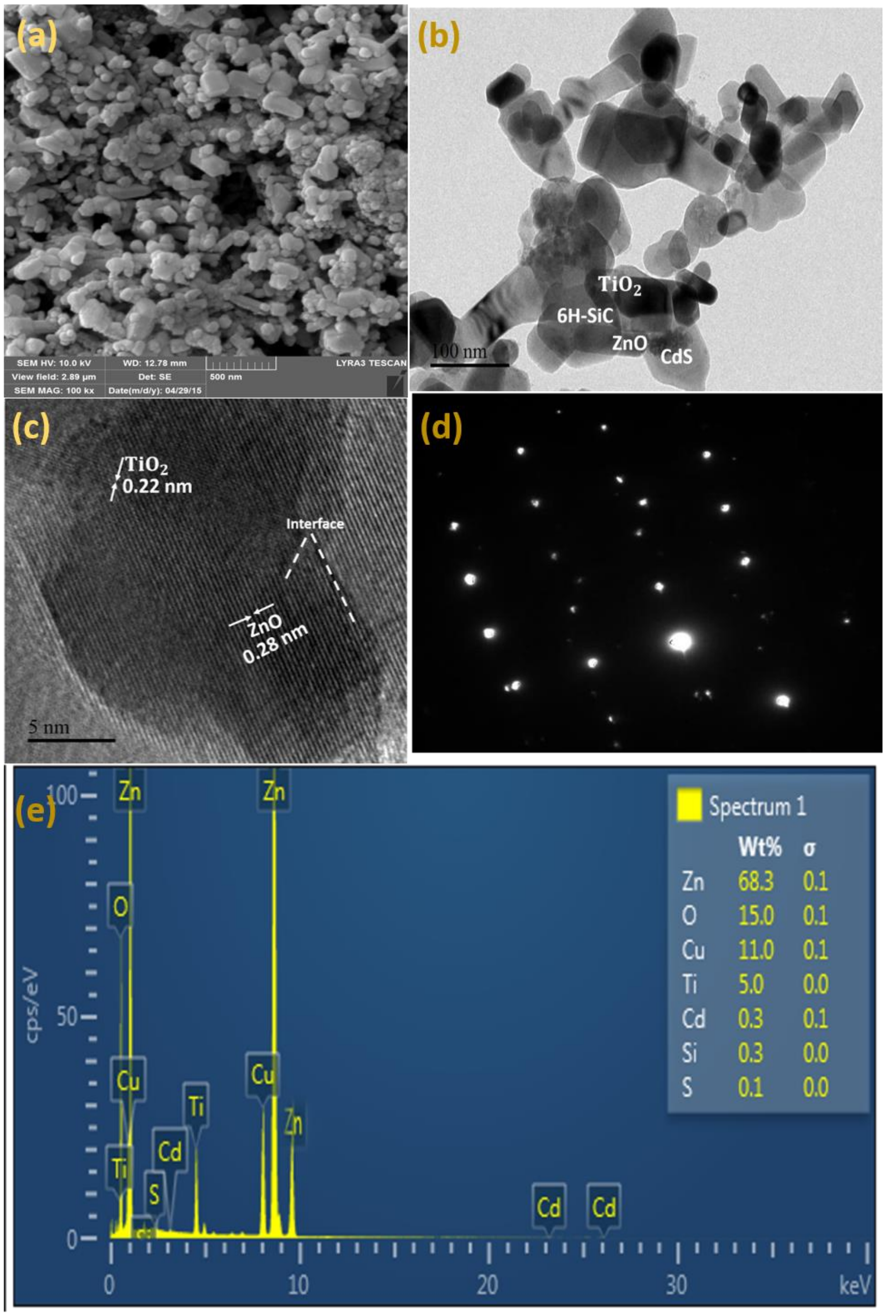

Figure 4.58 (a) FESEM image (b) TEM image (c) HRTEM image and (d) SAED (e) EDS of ZnO/TiO2/CdS/SiC nanocomposite

4.6.5 Optical analysis of quaternary nanocomposite

The light scattering ability of ZnO and ZnO/TiO_2/CdS/G is investigated using the UV-vis absorption spectra. Figure 4.59 shows the absorption spectra of ZnO NR and ZnO/TiO_2/CdS/G nanocomposite. The ZnO NR has an absorption threshold at ~363 nm. The ZnO/TiO_2/CdS/G and ZnO/TiO_2/CdS/SiC has a broad absorption edge which extends from 300 nm to 372 nm wavelength which covers even the deep UV region. This enhances the use of UV light in the nanocomposite compared to ZnO NR [81] and it shows band to band transition occurs between the UV-active components (TiO_2 and graphene) of the nanocomposite which improves its absorption in the UV- spectral region. However, the incorporation of CdS which are red in color, the nanocomposite exhibits a broad absorption edge in the Vis spectral region. Furthermore, a visible absorption peak around 450 nm towards the Vis and near IR region is a signature of the CdS present in the nanocomposite, the formation of Ti-O-C bands (C in graphene or SiC) and conveyance of electrons through multiple CB which leads to reduced charge transfer recombination.

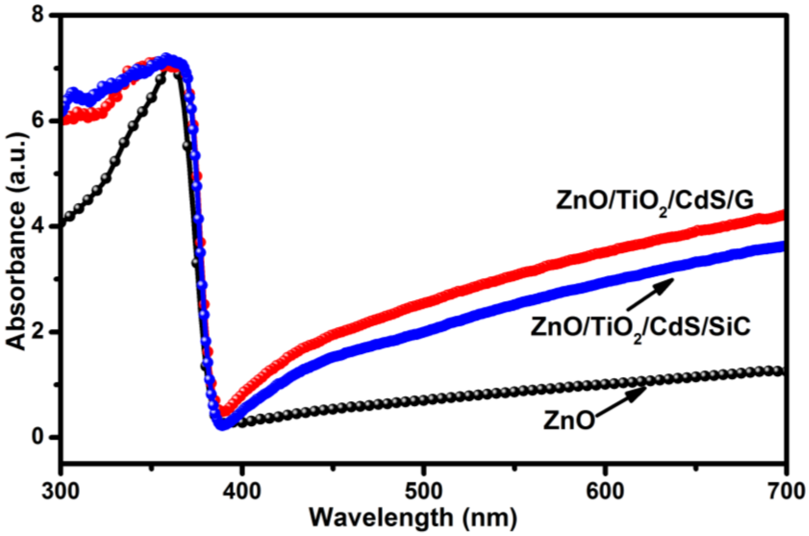

Figure 4.59 The UV-Vis absorption spectra of ZnO/TiO_2/CdS/G and ZnO/TiO_2/CdS/SiC quaternary nanocomposite compared with ZnO nanorod

4.6.6 XPS Analysis of quaternary nanocomposite

i. ZnO/TiO_2/CdS/G nanocomposite

XPS analysis of nanocomposite was done to further investigate the oxidation state of the elements (Zn, Ti, O, Cd, S, and C) in ZnO/TiO_2/CdS/G nanocomposite. The spin-orbit split was observed in Zn 2p, Ti 2p and Cd 3d peak of the synthesized nanocomposite. The Zn $2p_{3/2,}$ Ti $2p_{3/2}$, Cd $3d_{5/2}$, O 1s, S 2p and C 1s regions are shown in Figure 4.60(a-f). The spectrum of the Zn2p2/3 peaks shown in figure 4.60(a) was decomposed into three components. The peak at 1022.1 eV can be attributed to ZnO (Zn–O bonding state) [200], the second peak located at 1022.9[201] confirming the presence of zinc sulfate[189]. The values of the binding energies (BE) obtained for the Ti $2p_{3/2}$ peaks shown in figure 4.60(b) are at 458.5 eV[202] and 459.7 eV[203][204] both verify the presence of Ti–O.

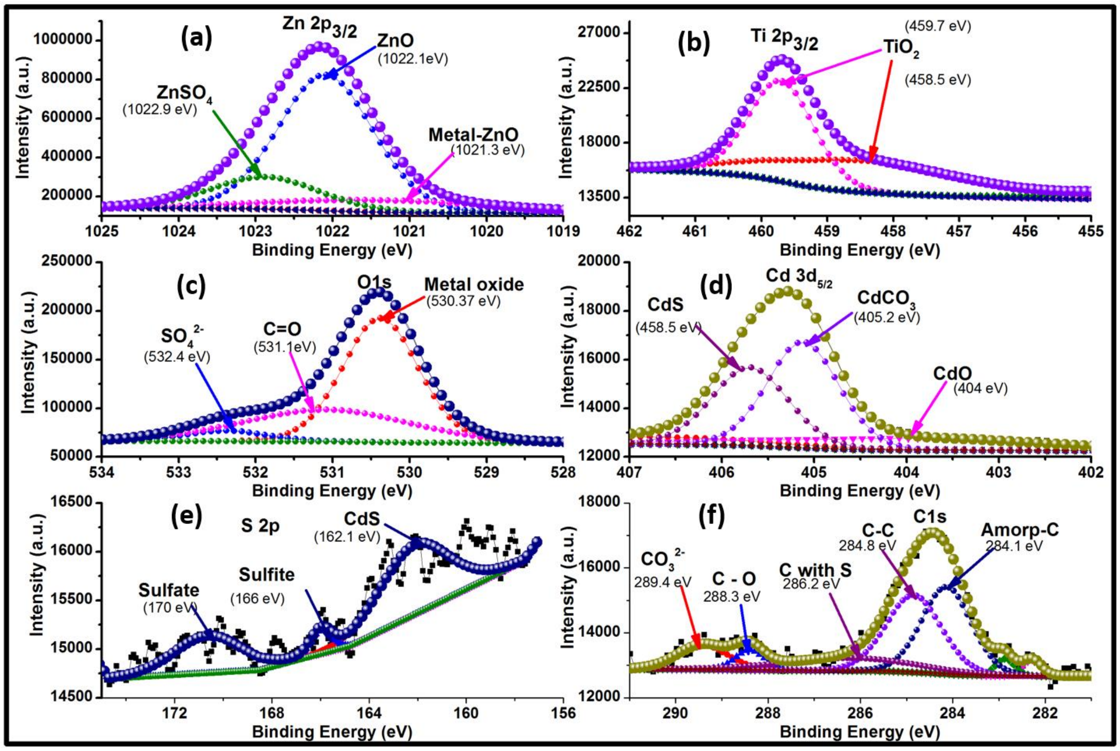

Figure 4.60 XPS spectra of ZnO/TiO_2/CdS/G

Deconvolution of the O 1s spectra shown in figure 4.60(c) indicates three main peaks around 530.4 eV, 531.1 and 532.4 eV which were assigned to O atoms in metal oxide[205], C=O(oxygen doubled bonded to aromatic carbon) [206], lattice oxygen (O_2^{2-})[207] and sulfates [189]. Cd $3d_{5/2}$peak is deconvoluted into two peaks as shown in figure 4.60(d) with binding energies at 405.7 eV which confirm the chemical identity of the CdS quantum dots[208], and at 405.2 eV assigned to Cd^{2+} of CdS nanoparticles [209][210] or $CdCO_3$[189] due to reaction of carbon in graphene with oxygen in the oxide semiconductors and Cd in the CdS and. The S 2p peak is resolved into three peaks as shown in figure 4.60(e). The peak located at 162.1 eV can be assigned to S^{2-}[211]of CdS, the peak at 166.0 eV for sulfite and the peak positioned at 170.0eV should be due to the sulfate ($SO4^{2-}$)on the surface. The C 1s can be deconvoluted into five peak component as shown in figure 4.57(f) with binding energies at 286.2 eV for the C-O species] [212] or C with S[189] , at 284.1 eV ascribed to the amorphous carbon coated on the surface of the particles [213][214], 284.8eV for C-C [189], 288.3 eV for the carbonyl (C-O) [215]and 289.4 eV for carbonates[189]. It can be observed that the XPS analysis also reveals the information about the entanglement of the nanoparticles in the nanocomposites. Such that: Zn and Ti have a bond with O (oxygen) in ZnO and TiO_2 and the Zn has a bond with S (sulphur). The Cd and S in CdS have a bond with O_2 either directly or indirectly, the Carbon (C) in graphene has a bond with O and S, This shows the quantum entanglement if knotted to the Sulphur in CdS and Oxygen in the oxide semiconductors (TiO_2 and ZnO).

ii. TiO_2/ZnO/CdS/SiC

The XPS analysis was also carried out to investigate the chemical composition of TiO_2/ZnO/CdS/SiC and the valence states of the elements present therein. The high-resolution scans of Ti 2p, Cd 3d, S 2p, Si 2p, O1s, C1s and Zn 2p states are given in Fig. 4.61(a-g). The spin-orbit split was observed in Ti 2p, Cd 3d, and Zn 2p states. Zn $2p_{3/2}$ of the spin-orbit split peak of Zn shown in Fig. 4.61(a) was fitted into peaks with positions at 1021.9 eV, 1022.6 eV and 1023.1 eV associated with Zn^{2+} bonds, di-zinc silicon tetraoxide (Zn_2SiO_4) bond[216] and sulfate in the sample respectively The Ti $2p_{3/2}$ peak in Fig. 4.61(b) was fitted into two peaks with position at 458.5 eV and 460.0 eV corresponding to TiO_2 and Titanium dioxide/silicon dioxide (TiO_2/SiO_2) respectively[190] .

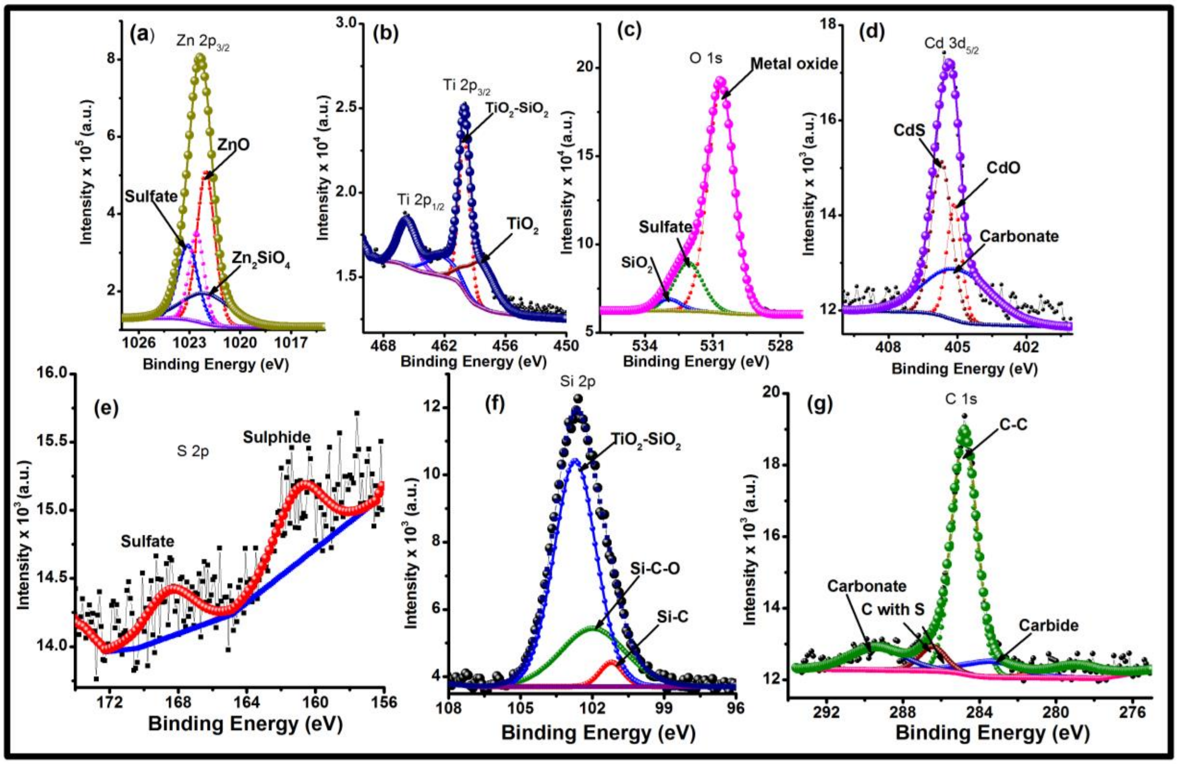

Figure 4.61 XPS spectra of ZnO/TiO_2/CdS/SiC

The O1s peak in Fig. 4.61(c) was deconvoluted into peaks located at 530.6 eV, 532.1 eV and 533.0 eV which are assigned to metal oxide, sulfates, and SiO_2 respectively[189]. The Cd $3d_{3/2}$ peak of the spin-orbit split peak shown in Fig. 4.61(d) was fitted into peaks with positions at 405.0 eV, 405.1 eV, and 405.7 eV which are attributed to the presence of CdO,

$CdCO_3$ and Cd^{2+} in CdS [217] respectively. The Sulfur peak in Fig. 4.61(e) located at 160.9 eV and 168.5 eV were attributed to the presence of S^{2-} state in CdS and the presence of Sulphate (SO_4^{2-}) in the sample which explains the reaction between the cat-ions of CdS and ZnO/TiO_2 interface [37]. The Si 2p spectrum shown in figure 4.61(f) obtained was fitted into three characteristic peaks of Silicon state at 101.1eV, 101.89 eV and 102.84 eV which correspond to SiC[186], SiC-O [187]and TiO_2-SiO_2 [188]respectively. The high-resolution spectrum of C1s spectrum in fig. 4.61 (g) shows three small fraction peaks at 283.4eV,284.8 eV, 286.45 eV and 289.35 eV which are associated with carbide (SiC)[190], C-C(The adventitious carbon C1s main peak used to calibrate the peak positions), C with S bond[189] and carbonate respectively.

4.6.7 Photovoltaic performance analysis

The photocurrent-voltage (J-V) curves of the DSSC assembled using ZnO and ZnO/TiO_2/CdS/G (G= graphene) as photoanode measured under solar irradiation is shown in figure 4.62. The incident light was 30 mW/cm^2. The effective area of the cell is ≤ 0.25 cm^2.The open circuit voltage, short circuit current density, Fill factor and power conversion efficiency known as the performance parameters of the DSSC obtained from fig 4.62. The ZnO-based DSSC shows a power conversion efficiency of 3.47 % with a short circuit current density value of 4.25 mA/cm^2 and an open circuit voltage value of 0.55 V. In comparison, It was observed that DSSC based on ZnO/TiO_2/CdS/G photoanode shows a power conversion efficiency of 9.47 % with a short circuit current density value of 14.4 mA/cm^2 and an open circuit voltage value of 0.51 V. As compared with ZnO NR, The Jsc of ZnO/TiO_2/CdS/G was increased by ~3.4 times due to improvement in surface area caused by the presence of TiO_2, improvement in optical absorbance by the presence of CdS or acceleration of electron permeation due to the presence of graphene sheet and interfacial connection between the TiO_2-NP, ZnO-NR, CdS-NP, and graphene sheet reducing charge recombination also improves electron transfer and hole trapping. However, the efficiency of ZnO NR was increased by ~3 times in the $ZnO/TiO_2/CdS/G$. Interestingly, It is observed that DSSC based on $ZnO/TiO_2/CdS/SiC$ photoanode shows a power conversion efficiency of 14.6 % with a short circuit current density value of 19.2 mA/cm^2 and an open circuit voltage value of 0.57 V. As compared with ZnO NR and $ZnO/TiO_2/CdS/G$ the J_{SC} was increased by ~6.8 and 2 times respectively.

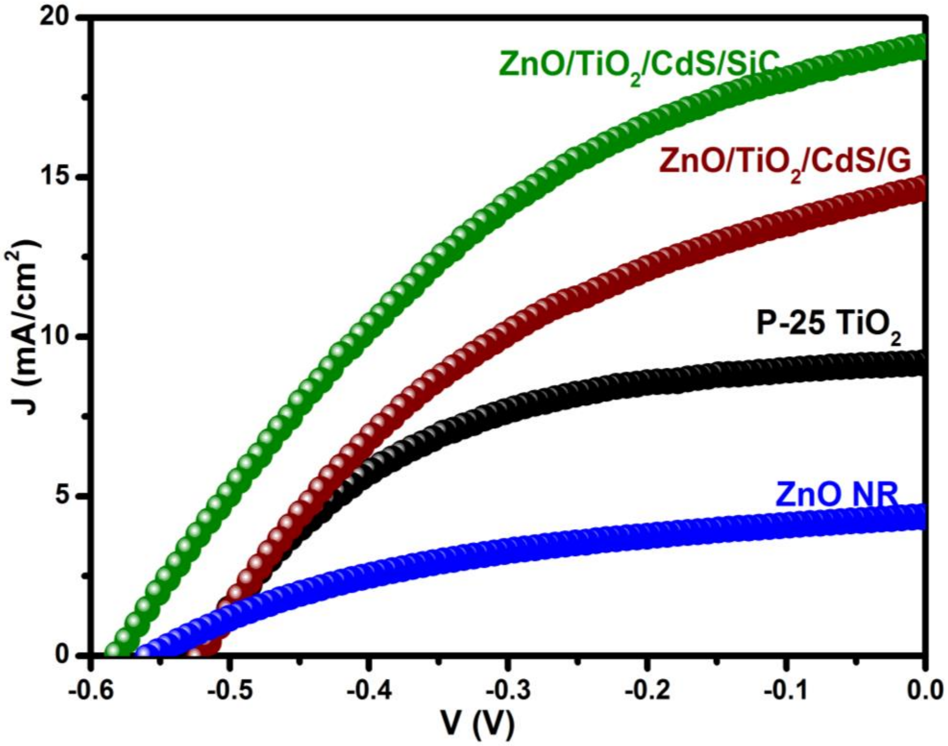

Figure 4.62 Photocurrent- voltage curve of ZnO NR, P-25 TiO_2, $ZnO/TiO_2/CdS$/graphene and $ZnO/TiO_2/CdS/SiC$

This explains the effect of material negative impact cancellation. This means in $ZnO/TiO_2/CdS/SiC$ composite, the self-oxidation undergone by the visible light active CdS is cancelled by the oxidation resistant SiC Hence, excellent separation of photogenerated charge carriers is accompanied with excellent electron generation and transport in the nanocomposite. Therefore, electron generation and conduction will be tremendously improved. Further comparison was done with DSSC based on P-25 photoanode which shows a power conversion efficiency of 7.81 % with a short circuit current density value of 9.4 mA/cm^2 and an open circuit voltage value of 0.51 V. This shows that the quaternary composites (ZnO/TiO_2/CdS/G and ZnO/TiO_2/CdS/SiC) have a better performance than the well-known bi-phase P-25 TiO_2 which has been reported the best in the fabrication of dye-sensitized solar cell due to the excellent reduced charge recombination and surface area for dye adsorption. The electrochemical impedance spectroscopy (EIS) measurements were carried out to evaluate the charge transfer resistance processes in the DSSC.

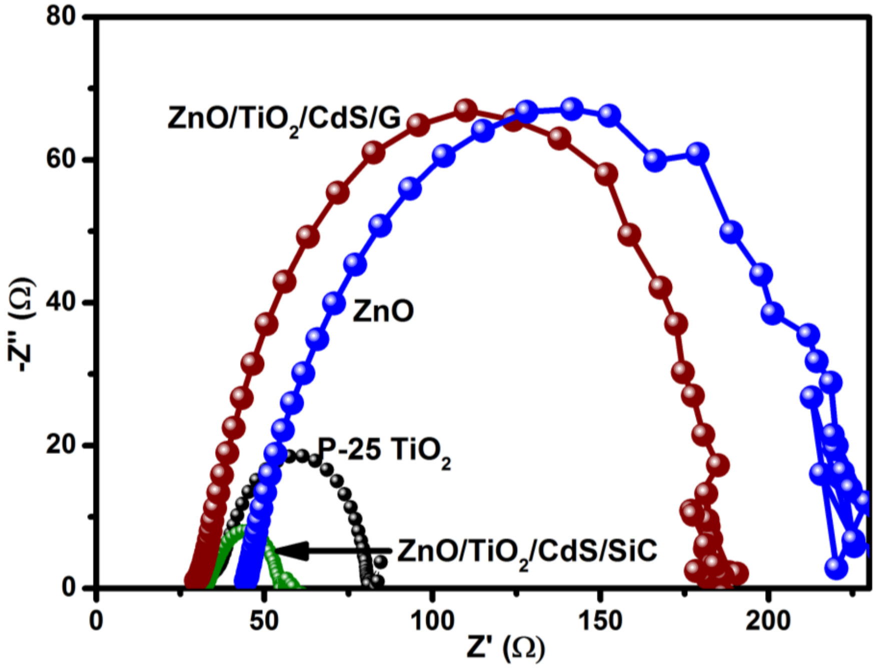

Figure 4.63 Nyquist curve of ZnO NR, P-25 TiO_2, ZnO/TiO_2/CdS/graphene and ZnO/TiO_2/CdS/SiC

The Nyquist plot of EIS spectra described by semicircles is shown in figure 4.63. The semicircle represented with R_2 is the electron transfer resistance at the photoelectrode/dye/electrolyte interface. The R_2 value of ZnO/TiO_2/CdS/SiC (~23 Ω) is tremendously lower than the charge transfer resistance of ZnO (~173.7 Ω), $ZnO/TiO_2/CdS/G$ (~153 Ω) and P-25 TiO_2 (~80 Ω). This indicates a reduction in the electron–hole recombination which is in good agreement with the observed increase in V_{OC} value as compared with other photoanodes. P-25 TiO_2 has shown an R_{CT} value lower than the value of $ZnO/TiO_2/CdS/G$ which is not consistent with the J_{SC} and efficiency value. This shows that improved performance of $ZnO/TiO_2/CdS/G$ over P-25 TiO_2 was not due to improved charge transfer generation but improved charge generation from CdS and graphene.

Table 4.5 Parameters of the DSSCs with ZnO NR, P-25 TiO_2, $ZnO/TiO_2/CdS/G$ and $ZnO/TiO_2/CdS/SiC$

	J_{SC} (mA/cm^2)	**Voc (V)**	**FF**	**η (%)**	**Rct (kΩ)**
ZnO NR	**4.25**	**0.55**	**0.43**	**3.47**	**173**
P-25 TiO_2	**9.38**	**0.51**	**0.49**	**7.81**	**80**
$ZnO/TiO_2/CdS/G$	**14.30**	**0.51**	**0.40**	**9.47**	**153**
$ZnO/TiO_2/CdS/SiC$	**19.20**	**0.57**	**0.40**	**14.59**	**23**

4.6.8 Charge transfer mechanism in the DSSC

i. $ZnO/TiO_2/CdS/G$ based DSSC

The charge transfer mechanism in the DSSC is shown in figure 4.64. Under Solar irradiation, the CdS and N719 dye are excited and the photogenerated electrons migrate to the conduction band of TiO_2, which could be subsequently collected by the ZnO. The photo-induced holes migrating away to recombine with the electrons in the conduction band are therefore trapped by the valence band of ZnO and TiO_2. The graphene captures and improve the rate of transfer of photo-generated electrons between graphene/CdS/TiO_2/ZnO Nanohybrid interfaces hence reducing the rate of photogenerated electron-hole pair recombination. The electrons in the conduction band finally migrate to the FTO substrate. On the other hand, the redox electrolyte (I_2 based electrolyte) regenerates the lost electrons in CdS and N719 Dye. At the counter electrode, the lost electron in the electrolyte is regenerated. The circuit is completed by transferring the electrons to the external load (Autolab potentiostat) through the electrode.

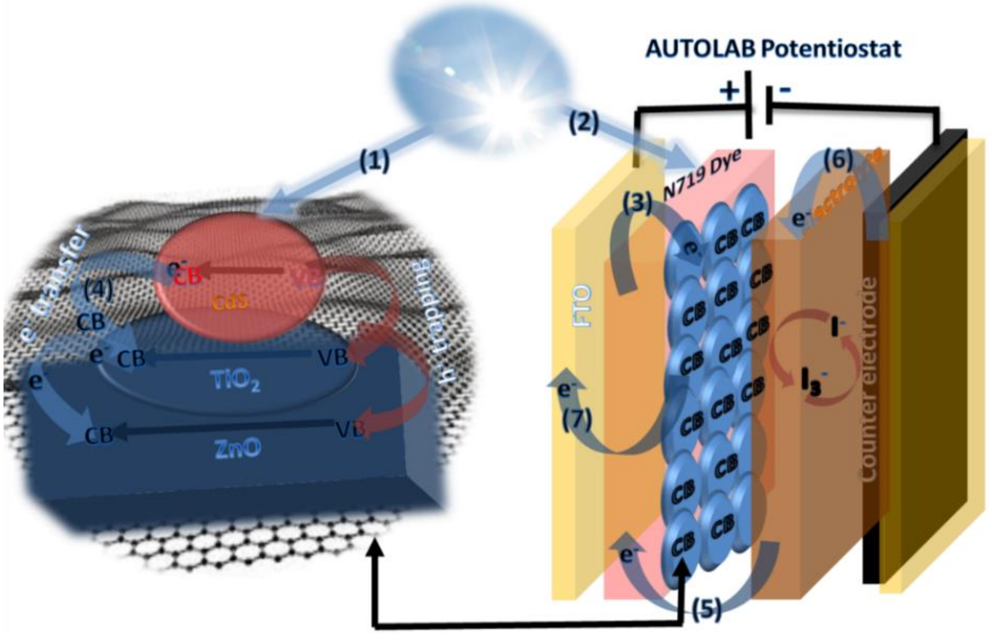

Figure 4.64 Charge injection mechanism diagram of the DSSC

ii. ZnO/TiO_2/CdS/SiC based DSSC

The Kinetics of electron transfer in the DSSC is shown in figure 4.65. Under Solar irradiation, the CdS and N719 dye are excited and the photogenerated electrons migrate to the conduction band of SiC, which is transferred TiO_2 CB. The photo-induced holes procreated in the CdS are trapped at the valence band of CdS by the SiC. This assists in charge transport separation. The electrons in TiO_2 CB and excited electrons from N719 dye converge at the FTO substrate. On the other hand, the lost electrons in CdS and N719

Dye is replaced by the redox electrolyte (I_2 based electrolyte). Since the counter electrode has a contact with the liquid electrolyte within the DSSC, the platinum catalyst coated counter substrate regenerates the electron lost by the electrolyte. The connection of an external load (Autolab potentiostat) through the electrode is used to complete the circuit.

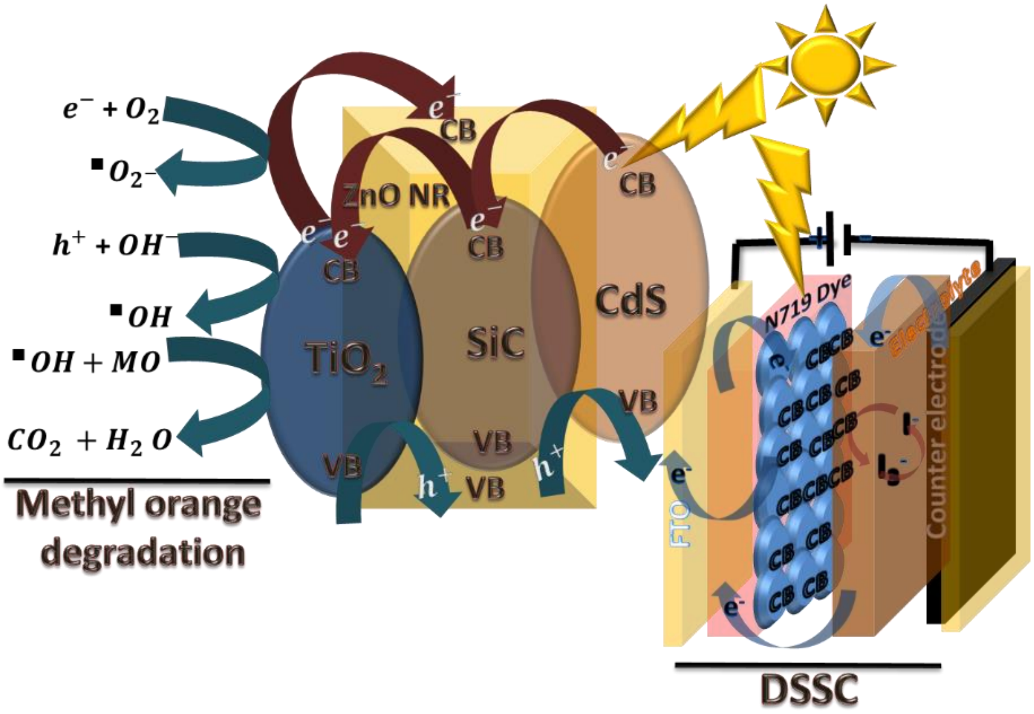

Figure 4.65 Charge transfer mechanism of ZnO/TiO_2/CdS/SiC based DSSC

CHAPTER FIVE

CONCLUSION AND FUTURE PROSPECTS

5.1 Conclusion.

So far in this work the following has been successfully achieved.

(a) CdS was successfully prepared from Cadmium acetate dihydrate by temperature controlled precipitation method.

(b) Transparent deionized water suspended Graphene sheets was successfully prepared by chemical vapor technique.

(c) Pulsed laser ablation technique was successfully used to prepare the following:

i. ZnO NR/TiO_2 NP nanocomposite

ii. TiO_2/CdS nanocomposite

iii. TiO_2/SiC nanocomposite

iv. TiO_2/graphene nanohybrid

v. ZnO/TiO_2/CdS/graphene nanocomposite

vi. ZnO/TiO_2/CdS/SiC nanocomposite

(d) The structural property and morphology of the nanocomposite were studied using XRD, Raman spectroscopy, SEM, and TEM.

(e) The optical property of the nanocomposite was investigated using UV-Vis spectrophotometry and FTIR.

(f) The elemental composition of the nanocomposite was confirmed using XPS.

(g) The photocatalytic and photovoltaic performance of the nanocomposite and nanohybrid were successfully investigated for the first time.

(h) The Photocatalytic performance of the nanocomposite was successfully investigated in the photodegradation of methyl orange (MO) under UV-Vis solar spectrum.

(i) The photovoltaic performance of the nanocomposite was obtained successfully when applied as photoanode in a DSSC.

(j) The photocatalytic performance of the nanocomposite follow the following trend:

i. ZnO/TiO_2 nanocomposite: ZnO/TiO_2 @ (9:1) > ZnO/TiO_2 @ (5:5) >ZnO NR> ZnO/TiO_2@ (3:7)>TiO_2 > ZnO/TiO_2@ (7:3)

ii. TiO_2/CdS nanocomposite: T-ox-CdS-20<CdS<T-ox-CdS-40<TiO_2<T-ox-CdS-10

iii. TiO_2/SiC nanocomposite: T-SiC-10 > T-SiC-20>TiO_2>T-SiC-40

(k) The trend of the photovoltaic performance of the nanocomposite is in the order:

i. ZnO/TiO_2 nanocomposite: ZnO/TiO_2@ (9:1)>ZnO NR >ZnO/TiO_2@ (7:3)> TiO_2 >ZnO/TiO_2@ (5:5)> ZnO/TiO_2@ (3:7)

ii. TiO_2/CdS nanocomposite: T-ox-CdS-10> T-ox-CdS-40>TiO_2> CdS > T-ox-CdS-20

iii. TiO_2/SiC nanocomposite: T-SiC-10> T-SiC-20>TiO_2>T-SiC-40

iv. TiO_2/graphene nanocomposite: G@ (50%)-TiO_2 < TiO_2 < G@ (16%)-TiO_2 <G@ (3%)-TiO_2

Therefore, the following conclusions can be derived from this work.

i. Moderate amount of SiC, CdS and graphene are needed for photocatalytic and photovoltaic enhancement.

ii. Computation is necessary when combining binary nanocomposite.

iii. Pulsed Laser Ablation technique is a useful technique in providing entanglement between nanoparticles by ion exchange.

iv. Quaternary nanocomposite can provide a breakthrough to semiconductors heterostructures with reduced setbacks.

v. The photocatalytic and photovoltaic applications are almost similar when less oxidizing catalysts are taken into consideration.

vi. The problem of low efficiency in DSSC still lies in the setback faced by the photoanode.

5.2 Future Prospects

The following recommendations can be made after successful completion of this work.

- Other visible light sensitive catalyst chalcogenide may be used in place of CdS
- Noble metals like silver and gold may be tried in place of the chalcogenides
- Another metal oxide may be used to replace TiO_2 and ZnO
- Nobel metal doped quaternary or pentenary composite can be synthesized
- Catalysts produced by PLAL can also be used applied for CO_2 conversion.
- With PLAL, there is no limitation to the number of semiconductor catalyst that can be combined to form heterostructure.
- Computation may be used as a tool ternary and quaternary nanocomposites
- Other carbon-based materials like carbon nanotube, fullerene may also be used to replace graphene in the quaternary composite.

REFERENCES

[1] K. Bhattarai, W. M. Stalick, S. McKay, G. Geme, and N. Bhattarai, “Biofuel: an alternative to fossil fuel for alleviating world energy and economic crises.,” *J. Environ. Sci. Health. A. Tox. Hazard. Subst. Environ. Eng.*, vol. 46, no. 12, pp. 1424–42, 2011.

[2] S. A. Montzka, E. J. Dlugokencky, and J. H. Butler, “Non-CO2 greenhouse gases and climate change.,” *Nature*, vol. 476, no. 7358, pp. 43–50, Aug. 2011.

[3] D. K. Bhattacharyya, “Issues in the disposal of waste containing naturally occurring radioactive material,” *Appl. Radiat. Isot.*, vol. 49, no. 3, pp. 215–226, 1998.

[4] G. Destouni and H. Frank, “Renewable energy,” *Ambio*, vol. 39, no. June, pp. 18–21, 2010.

[5] A. Goetzberger and C. Hebling, “Photovoltaic materials, past, present, future,” *Sol. Energy Mater. Sol. Cells*, vol. 62, no. 1, pp. 1–19, 2000.

[6] O. Isabella, A. H. M. Smets, and M. Zeman, “Thin-film silicon-based quadruple junction solar cells approaching 20% conversion efficiency,” *Sol. Energy Mater. Sol. Cells*, vol. 129, pp. 82–89, 2014.

[7] K. Masuko, M. Shigematsu, T. Hashiguchi, D. Fujishima, M. Kai, N. Yoshimura, T. Yamaguchi, Y. Ichihashi, T. Mishima, N. Matsubara, T. Yamanishi, T. Takahama, M. Taguchi, E. Maruyama, and S. Okamoto, “Achievement of More Than 25% Conversion Efficiency With Crystalline Silicon Heterojunction Solar Cell,” *IEEE J. Photovoltaics*, vol. 4, no. 6, pp. 1433–1435, 2014.

[8] T. Saga, “Advances in crystalline silicon solar cell technology for industrial mass production,” *NPG Asia Mater.*, vol. 2, no. 3, pp. 96–102, Jul. 2010.

[9] H. Liu and Z. L. Wang, “Etching silicon wafer without hydrofluoric acid,” *Appl. Phys. Lett.*, vol. 87, no. 26, pp. 1–3, 2005.

[10] B. O’Regan and M. Grätzel, “A low-cost, high-efficiency solar cell based on dye-sensitized colloidal TiO2 films,” *Nature*, vol. 353, pp. 737–740, 1991.

[11] S. Mathew, A. Yella, P. Gao, R. Humphry-Baker, B. F. E. Curchod, N. Ashari-Astani, I. Tavernelli, U. Rothlisberger, M. K. Nazeeruddin, and M. Grätzel, “Dye-sensitized solar cells with 13% efficiency achieved through the molecular engineering of porphyrin sensitizers.,” *Nat. Chem.*, vol. 6, no. 3, pp. 242–7, Mar. 2014.

[12] H. Hug, M. Bader, P. Mair, and T. Glatzel, “Biophotovoltaics: Natural pigments in dye-sensitized solar cells,” *Appl. Energy*, vol. 115, pp. 216–225, Feb. 2014.

[13] H. M. Upadhyaya, S. Senthilarasu, M. H. Hsu, and D. K. Kumar, “Recent progress and the status of dye-sensitised solar cell (DSSC) technology with state-of-the-art conversion efficiencies,” *Sol. Energy Mater. Sol. Cells*, vol. 119, pp. 291–295, 2013.

[14] S. N. Singh, Ed., *Microbial Degradation of Synthetic Dyes in Wastewaters*. Cham: Springer International Publishing, 2015.

[15] D. W. Hendricks, *Water Treatment Unit Processes: Physical and Chemical*. CRC Press, 2006.

[16] J. T. McCloskey and J. T. Oris, “Effect of water temperature and dissolved oxygen concentration on the photo-induced toxicity of anthracene to juvenile bluegill sunfish (Lepomis macrochirus).,” *Aquat. Toxicol.*, vol. 21, no. 3–4, pp. 145–156, 1991.

[17] T. Nguyen, F. A. Roddick, and L. Fan, “Biofouling of water treatment membranes: a review of the underlying causes, monitoring techniques and control measures.,” *Membranes (Basel).*, vol. 2, no. 4, pp. 804–40, Jan. 2012.

[18] S. C. Yan, Z. S. Li, and Z. G. Zou, “Photodegradation of rhodamine B and methyl orange over boron-doped g-C3N4 under visible light irradiation.,” *Langmuir*, vol. 26, no. 6, pp. 3894–3901, 2010.

[19] D. A. Gish, G. K. Kiema, M. O. Jensen, and M. J. Brett, “Dye Sensitized Solar Cells Using Nanostructured Thin Films of Titanium Dioxide,” *MRS Proc.*, vol. 836, p. L5.13, Feb. 2011.

[20] C. Sima, C. Grigoriu, and S. Antohe, “Comparison of the dye-sensitized solar cells performances based on transparent conductive ITO and FTO,” *Thin Solid Films*, vol. 519, no. 2, pp. 595–597, 2010.

[21] M. A. Aouaj, R. Diaz, a. Belayachi, F. Rueda, and M. Abd-Lefdil, “Comparative study of ITO and FTO thin films grown by spray pyrolysis,” *Mater. Res. Bull.*, vol. 44, no. 7, pp. 1458–1461, 2009.

[22] M. Hoffmann and S. Martin, “Environmental applications of semiconductor photocatalysis,” *Chem. ...*, 1995.

[23] D. Han, J. Heo, and D. Kwak, “Texture, Morphology and Photovoltaic Characteristics of Nanoporous F: SnO_2 Films,” *J. Electr. ...*, 2009.

[24] O. Lupan, V. Guérin, and I. Tiginyanu, “Well-aligned arrays of vertically oriented ZnO nanowires electrodeposited on ITO-coated glass and their integration in dye sensitized solar cells,” *... Photochem. ...*, 2010.

[25] C. Bauer and G. Boschloo, “Ultrafast studies of electron injection in Ru dye

sensitized SnO 2 nanocrystalline thin film," *Int. J. …*, 2002.

[26] H. Li, Y. Li, and M. Chen, "Molecular design of organic sensitizers absorbing over a broadened visible region for dye-sensitized solar cells," *RSC Adv.*, vol. 4, no. 101, pp. 57916–57922, Oct. 2014.

[27] D.-Y. Chen, Y.-Y. Hsu, H.-C. Hsu, B.-S. Chen, Y.-T. Lee, H. Fu, M.-W. Chung, S.-H. Liu, H.-C. Chen, Y. Chi, and P.-T. Chou, "Organic dyes with remarkably high absorptivity; all solid-state dye sensitized solar cell and role of fluorine substitution.," *Chem. Commun. (Camb).*, vol. 46, no. 29, pp. 5256–8, Aug. 2010.

[28] W. Hu, F. Bai, X. Gong, X. Zhan, H. Fu, and T. Bjornholm, *Organic Optoelectronics*, vol. 5. John Wiley & Sons, 2012.

[29] A. McEvoy, L. Castaner, and T. Markvart, *Solar Cells: Materials, Manufacture and Operation*. Newnes, 2012.

[30] C. Teng, X. Yang, S. Li, M. Cheng, A. Hagfeldt, L. Wu, and L. Sun, "Tuning the HOMO energy levels of organic dyes for dye-sensitized solar cells based on Br-/Br3- electrolytes.," *Chemistry*, vol. 16, no. 44, pp. 13127–38, Nov. 2010.

[31] C.-C. Ko and V. Wing-Wah Yam, "Transition metal complexes with photochromic ligands—photosensitization and photoswitchable properties," *J. Mater. Chem.*, vol. 20, no. 11, pp. 2063–2070, Mar. 2010.

[32] Y. Bai, Y. Cao, J. Zhang, M. Wang, R. Li, P. Wang, S. M. Zakeeruddin, and M. Grätzel, "High-performance dye-sensitized solar cells based on solvent-free electrolytes produced from eutectic melts.," *Nat. Mater.*, vol. 7, no. 8, pp. 626–30, Aug. 2008.

[33] S. Suhaimi, M. M. Shahimin, Z. A. Alahmed, J. Chysky, and A. H. Reshak,

"Materials for Enhanced Dye-sensitized Solar Cell Performance: Electrochemical Application," *Int. J. Electrochem. Sci.*, vol. 10, no. 4, pp. 2859–2871, 2015.

[34] A. Nogueira, C. Longo, and M. De Paoli, "Polymers in dye sensitized solar cells: overview and perspectives," *Coord. Chem. Rev.*, 2004.

[35] H. Kusama and H. Arakawa, "Influence of pyrazole derivatives in I−/I 3− redox electrolyte solution on Ru (II)-dye-sensitized TiO 2 solar cell performance," *Sol. energy Mater. Sol. cells*, 2005.

[36] Z. Wang, K. Sayama, and H. Sugihara, "Efficient eosin y dye-sensitized solar cell containing Br-/Br3-electrolyte," *J. Phys. ...*, 2005.

[37] B. Bergeron and A. Marton, "Dye-sensitized SnO2 electrodes with iodide and pseudohalide redox mediators," *J. Phys. ...*, 2005.

[38] G. Oskam and B. Bergeron, "Pseudohalogens for dye-sensitized TiO2 photoelectrochemical cells," *J. Phys. ...*, 2001.

[39] S. Sapp and C. Elliott, "Substituted polypyridine complexes of cobalt (II/III) as efficient electron-transfer mediators in dye-sensitized solar cells," *J. ...*, 2002.

[40] T. Stergiopoulos and E. Rozi, "Influence of electrolyte co-additives on the performance of dye-sensitized solar cells," *Nanoscale Res. ...*, 2011.

[41] P. Chawla and M. Tripathi, "Nanocomposite Polymer Electrolyte for Enhancement in Stability of Betacyanin Dye Sensitized Solar Cells," *ECS Solid State Lett.*, vol. 4, no. 6, pp. Q21–Q23, Apr. 2015.

[42] C.-L. Chen, H. Teng, and Y.-L. Lee, "Preparation of highly efficient gel-state dye-sensitized solar cells using polymer gel electrolytes based on poly(acrylonitrile-co-vinyl acetate)," *J. Mater. Chem.*, vol. 21, no. 3, p. 628, 2011.

[43] I. Chung, B. Lee, J. He, R. P. H. Chang, and M. G. Kanatzidis, “All-solid-state dye-sensitized solar cells with high efficiency,” *Nature*, vol. 485, no. 7399, pp. 486–489, 2012.

[44] L. Tao, Z. Huo, Y. Ding, Y. Li, S. Dai, L. Wang, J. Zhu, X. Pan, B. Zhang, J. Yao, M. K. Nazeeruddin, and M. Grätzel, “High-efficiency and stable quasi-solid-state dye-sensitized solar cell based on low molecular mass organogelator electrolyte,” *J. Mater. Chem. A*, vol. 3, no. 5, pp. 2344–2352, Jan. 2015.

[45] P. Wang, S. M. Zakeeruddin, J. E. Moser, M. K. Nazeeruddin, T. Sekiguchi, and M. Grätzel, “A stable quasi-solid-state dye-sensitized solar cell with an amphiphilic ruthenium sensitizer and polymer gel electrolyte.,” *Nat. Mater.*, vol. 2, no. 6, pp. 402–7, 2003.

[46] N. Papageorgiou, W. Maier, and M. Grätzel, “An iodine/triiodide reduction electrocatalyst for aqueous and organic media,” *J. Electrochem. …*, 1997.

[47] G. Syrrokostas and A. Siokou, “Degradation mechanisms of Pt counter electrodes for dye sensitized solar cells,” *Sol. Energy Mater. …*, 2012.

[48] J. Jeon, Y. C. Park, S. S. Han, W. A. Goddard, Y. S. Lee, and H. Kim, “Rapid Dye Regeneration Mechanism of Dye-Sensitized Solar Cells.,” *J. Phys. Chem. Lett.*, vol. 5, no. 24, pp. 4285–90, Dec. 2014.

[49] M. Grätzel, “Conversion of sunlight to electric power by nanocrystalline dye-sensitized solar cells,” *J. Photochem. Photobiol. A Chem.*, vol. 164, no. 1–3, pp. 3–14, 2004.

[50] M. Grätzel, “Dye-sensitized solar cells,” *J. Photochem. Photobiol. C Photochem. Rev.*, vol. 4, no. 2, pp. 145–153, Oct. 2003.

[51] T. Katagi, “Photodegradation of pesticides on plant and soil surfaces.,” *Rev. Environ. Contam. Toxicol.*, vol. 182, pp. 1–189, Jan. 2004.

[52] N. R. Dhar, “Formation of hydroxyl radical from the photolysis of water and the generation of formaldehyde,” *Trans. Faraday Soc.*, vol. 30, p. 142, Jan. 1934.

[53] M. a Tarr, “Chemical Degradation Methods for Wastes and Pollutants,” *Combustion*, 2003.

[54] M. M. Benjamin and D. F. Lawler, *Water Quality Engineering: Physical / Chemical Treatment Processes*. John Wiley & Sons, 2013.

[55] D. I. Kondarides, “Photocatalysis,” in *CATALYSIS – Photocatalysis*, 2009, pp. 1 – 11.

[56] C. Chen, W. Ma, and J. Zhao, “Semiconductor-mediated photodegradation of pollutants under visible-light irradiation.,” *Chem. Soc. Rev.*, vol. 39, no. 11, pp. 4206–19, Nov. 2010.

[57] M. R. Hoffmann, S. T. Martin, W. Choi, and D. W. Bahnemannt, “Environmental Applications of Semiconductor Photocatalysis,” *Chem. Rev.*, vol. 95, no. 1, pp. 69–96, 1995.

[58] X. Chen and S. S. Mao, “Titanium dioxide nanomaterials: synthesis, properties, modifications, and applications.,” *Chem. Rev.*, vol. 107, no. 7, pp. 2891–959, Jul. 2007.

[59] F. Amano, K. Nogami, M. Tanaka, and B. Ohtani, “Correlation between surface area and photocatalytic activity for acetaldehyde decomposition over bismuth tungstate particles with a hierarchical structure.,” *Langmuir*, vol. 26, no. 10, pp. 7174–80, May 2010.

[60] N. M. Flores, U. Pal, R. Galeazzi, and A. Sandoval, “Effects of morphology, surface area, and defect content on the photocatalytic dye degradation performance of ZnO nanostructures,” *RSC Adv.*, vol. 4, no. 77, pp. 41099–41110, Aug. 2014.

[61] E. Lichtfouse, J. Schwarzbauer, and D. Robert, *CO2 Sequestration, Biofuels and Depollution*, vol. 5. 2015.

[62] M. A. Barakat and R. Kumar, *Photocatalytic Activity Enhancement of Titanium Dioxide Nanoparticles: Degradation of Pollutants in Wastewater*. Springer, 2015.

[63] K. Sridharan, E. Jang, and T. J. Park, “Novel visible light active graphitic C3N4-TiO2 composite photocatalyst: Synergistic synthesis, growth and photocatalytic treatment of hazardous pollutants,” *Appl. Catal. B Environ.*, vol. 142–143, pp. 718–728, 2013.

[64] A. Habib, T. Shahadat, N. M. Bahadur, I. M. I. Ismail, and A. J. Mahmood, “Synthesis and characterization of ZnO-TiO 2 nanocomposites and their application as photocatalysts,” *Int. Nano Lett.*, vol. 3, no. 5, pp. 1–8, 2013.

[65] A. A. Madhavan, A. Mohandas, A. Licciulli, K. P. Sanosh, P. Praveen, R. Jayakumar, S. V. Nair, A. S. Nair, and A. Balakrishnan, “Electrospun continuous nanofibers based on a TiO2–ZnO–graphene composite,” *RSC Adv.*, vol. 3, no. 47, p. 25312, 2013.

[66] A. C. Lee, R. H. Lin, C. Y. Yang, M. H. Lin, and W. Y. Wang, “Preparations and characterization of novel photocatalysts with mesoporous titanium dioxide (TiO2) via a sol-gel method,” *Mater. Chem. Phys.*, vol. 109, no. 2–3, pp. 275–280, 2008.

[67] M. a. Behnajady, H. Eskandarloo, N. Modirshahla, and M. Shokri, “Investigation of the effect of sol-gel synthesis variables on structural and photocatalytic

properties of TiO2 nanoparticles," *Desalination*, vol. 278, no. 1–3, pp. 10–17, 2011.

[68] T. C. Dang, D. L. Pham, H. C. Le, and V. H. Pham, "TiO 2 /CdS nanocomposite films: fabrication, characterization, electronic and optical properties," *Adv. Nat. Sci. Nanosci. Nanotechnol.*, vol. 1, no. 1, p. 015002, Mar. 2010.

[69] H. Zhao, L. Liu, J. M. Andino, and Y. Li, "Bicrystalline TiO2 with controllable anatase–brookite phase content for enhanced CO2 photoreduction to fuels," *J. Mater. Chem. A*, vol. 1, no. 28, p. 8209, 2013.

[70] D. C. Hurum, A. G. Agrios, S. E. Crist, K. A. Gray, T. Rajh, and M. C. Thurnauer, "Probing reaction mechanisms in mixed phase TiO2 by EPR," *J. Electron Spectros. Relat. Phenomena*, vol. 150, no. 2–3, pp. 155–163, 2006.

[71] X. Zhang, J. Qin, Y. Xue, P. Yu, B. Zhang, L. Wang, and R. Liu, "Effect of aspect ratio and surface defects on the photocatalytic activity of ZnO nanorods.," *Sci. Rep.*, vol. 4, p. 4596, 2014.

[72] D. C. Reynolds, D. C. Look, B. Jogai, J. E. Hoelscher, and R. E. Sherriff, "Time-resolved photoluminescence lifetime measurements of the Γ[sub 5] and Γ[sub 6] free excitons in ZnO," *J. Appl. Phys.*, vol. 88, no. 4, p. 2152, 2000.

[73] A. B. F. Martinson, J. E. McGarrah, M. O. K. Parpia, and J. T. Hupp, "Dynamics of charge transport and recombination in ZnO nanorod array dye-sensitized solar cells.," *Phys. Chem. Chem. Phys.*, vol. 8, no. 40, pp. 4655–4659, 2006.

[74] C. Transport, Z. Nanorod, and A. D. Solar, "Charge Transport in ZnO Nanorod Array Dye-Sensitized Solar Cells," *Electrochem. Soc. Interface*, vol. 15, no. 4, pp. 53–54, 2006.

[75] D. Bi, G. Boschloo, S. Schwarzmüller, L. Yang, E. M. J. Johansson, and A. Hagfeldt, “Efficient and stable CH3NH3PbI3-sensitized ZnO nanorod array solid-state solar cells.,” *Nanoscale*, vol. 5, no. 23, pp. 11686–91, 2013.

[76] Y. Gu, I. L. Kuskovsky, M. Yin, S. O’Brien, and G. F. Neumark, “Quantum confinement in ZnO nanorods,” *Appl. Phys. Lett.*, vol. 85, no. 17, p. 3833, Oct. 2004.

[77] L. Wu, J. Xing, Y. Hou, F. Y. Xiao, Z. Li, and H. G. Yang, “Fabrication of regular ZnO/TiO2 heterojunctions with enhanced photocatalytic properties.,” *Chemistry*, vol. 19, no. 26, pp. 8393–6, Jun. 2013.

[78] L. E. Greene, M. Law, B. D. Yuhas, and P. Yang, “ZnO-TiO2 Core-Shell Nanorod/P3HT Solar Cells,” *J. Phys. Chem. C*, vol. 111, no. 50, pp. 18451–18456, 2007.

[79] M. Agrawal, S. Gupta, A. Pich, N. E. Zafeiropoulos, and M. Stamm, “A facile approach to fabrication of ZnO-TiO2 hollow spheres,” *Chem. Mater.*, vol. 21, no. 21, pp. 5343–5348, 2009.

[80] N. Wang, C. Sun, Y. Zhao, S. Zhou, P. Chen, and L. Jiang, “Fabrication of three-dimensional ZnO/TiO2 heteroarchitectures via a solution process,” *Journal of Materials Chemistry*, vol. 18, no. 33. p. 3909, 2008.

[81] C. Cheng, A. Amini, C. Zhu, Z. Xu, H. Song, and N. Wang, “Enhanced photocatalytic performance of TiO2-ZnO hybrid nanostructures.,” *Sci. Rep.*, vol. 4, p. 4181, Jan. 2014.

[82] J. A. Seabold, K. Shankar, R. H. T. Wilke, M. Paulose, O. K. Varghese, C. A. Grimes, and K.-S. Choi, “Photoelectrochemical Properties of Heterojunction

CdTe/TiO 2 Electrodes Constructed Using Highly Ordered TiO 2 Nanotube Arrays,” *Chem. Mater.*, vol. 20, no. 16, pp. 5266–5273, Aug. 2008.

[83] W. K. Bae, J. Joo, L. A. Padilha, J. Won, D. C. Lee, Q. Lin, W. Koh, H. Luo, V. I. Klimov, and J. M. Pietryga, “Highly effective surface passivation of PbSe quantum dots through reaction with molecular chlorine.,” *J. Am. Chem. Soc.*, vol. 134, no. 49, pp. 20160–8, Dec. 2012.

[84] H. Wang, T. Kubo, J. Nakazaki, T. Kinoshita, and H. Segawa, “PbS-Quantum-Dot-Based Heterojunction Solar Cells Utilizing ZnO Nanowires for High External Quantum Efficiency in the Near-Infrared Region,” *J. Phys. Chem. Lett.*, vol. 4, no. 15, pp. 2455–2460, Aug. 2013.

[85] F. Liu, J. Zhu, J. Wei, Y. Li, L. Hu, Y. Huang, O. Takuya, Q. Shen, T. Toyoda, B. Zhang, J. Yao, and S. Dai, “Ex Situ CdSe Quantum Dot-Sensitized Solar Cells Employing Inorganic Ligand Exchange To Boost Efficiency,” *J. Phys. Chem. C*, vol. 118, no. 1, pp. 214–222, Jan. 2014.

[86] Y. Cui, J. Wang, S. R. Plissard, A. Cavalli, T. T. T. Vu, R. P. J. van Veldhoven, L. Gao, M. Trainor, M. A. Verheijen, J. E. M. Haverkort, and E. P. A. M. Bakkers, “Efficiency enhancement of InP nanowire solar cells by surface cleaning.,” *Nano Lett.*, vol. 13, no. 9, pp. 4113–7, Sep. 2013.

[87] P. K. Santra and P. V Kamat, “Mn-doped quantum dot sensitized solar cells: a strategy to boost efficiency over 5%.,” *J. Am. Chem. Soc.*, vol. 134, no. 5, pp. 2508–11, Feb. 2012.

[88] M. A. Mahadik, P. S. Shinde, M. Cho, and J. S. Jang, “Fabrication of a ternary CdS/ZnIn 2 S 4 /TiO 2 heterojunction for enhancing photoelectrochemical

performance: effect of cascading electron–hole transfer," *J. Mater. Chem. A*, 2015.

[89] Y. Cui, "In-situ synthesis of C3N4/CdS composites with enhanced photocatalytic properties," *Chinese J. Catal.*, vol. 36, no. 3, pp. 372–379, Mar. 2015.

[90] S. Bingham and W. A. Daoud, "Recent advances in making nano-sized TiO 2 visible-light active through rare-earth metal doping," *J. Mater. Chem.*, vol. 21, no. 7, pp. 2041–2050, Feb. 2011.

[91] S. Song, X. Wang, and H. Zhang, "CeO2-encapsulated noble metal nanocatalysts: enhanced activity and stability for catalytic application," *NPG Asia Mater.*, vol. 7, no. 5, p. e179, May 2015.

[92] M. M. Khan, S. a Ansari, M. I. Amal, J. Lee, and M. H. Cho, "Highly visible light active Ag@TiO2 nanocomposites synthesized using an electrochemically active biofilm: a novel biogenic approach.," *Nanoscale*, vol. 5, pp. 4427–35, 2013.

[93] E. Traversa, M. Luisa, D. I. Vona, P. Nunziante, S. Licoccia, T. Chimiche, R. Tor, and R. Scientifica, "Sol-Gel Preparation and Characterization of Ag-TiO 2 Nanocomposite Thin Films," *J. SolGel Sci. Technol.*, vol. 19, no. 1, pp. 733–736, 2000.

[94] Y. Wen, H. Ding, and Y. Shan, "Preparation and visible light photocatalytic activity of Ag/TiO_2/graphene nanocomposite.," *Nanoscale*, vol. 3, no. 10, pp. 4411–7, Oct. 2011.

[95] S. Linic, P. Christopher, and D. B. Ingram, "Plasmonic-metal nanostructures for efficient conversion of solar to chemical energy," *Nat. Mater.*, vol. 10, no. 12, pp. 911–921, 2011.

[96] T. Kawawaki, Y. Takahashi, and T. Tatsuma, "Enhancement of dye-sensitized

photocurrents by gold nanoparticles: effects of dye-particle spacing.," *Nanoscale*, vol. 3, no. 7, pp. 2865–7, Jul. 2011.

[97] E. Kazuma, N. Sakai, and T. Tatsuma, "Nanoimaging of localized plasmon-induced charge separation.," *Chem. Commun. (Camb).*, vol. 47, no. 20, pp. 5777–5779, 2011.

[98] Z. Fan, J. Yan, L. Zhi, Q. Zhang, T. Wei, J. Feng, M. Zhang, W. Qian, and F. Wei, "A three-dimensional carbon nanotube/graphene sandwich and its application as electrode in supercapacitors," *Adv. Mater.*, vol. 22, no. 33, pp. 3723–3728, 2010.

[99] S. Mao, G. Lu, and J. Chen, "Three-dimensional graphene-based composites for energy applications.," *Nanoscale*, vol. 7, no. 16, pp. 6924–43, Apr. 2015.

[100] C. Hu, T. Lu, F. Chen, and R. Zhang, "A brief review of graphene–metal oxide composites synthesis and applications in photocatalysis," *J. Chinese Adv. Mater. Soc.*, Apr. 2013.

[101] Q. Zhang, Y. Q. He, X. G. Chen, D. H. Hu, L. J. Li, T. Yin, and L. L. Ji, "Structure and photocatalytic properties of TiO2-Graphene Oxide intercalated composite," *Chinese Sci. Bull.*, vol. 56, no. 3, pp. 331–339, 2011.

[102] G. Williams, B. Seger, and P. V. Kamat, "TiO2-graphene nanocomposites. UV-assisted photocatalytic reduction of graphene oxide," *ACS Nano*, vol. 2, no. 7, pp. 1487–1491, 2008.

[103] J. Du, X. Lai, N. Yang, J. Zhai, D. Kisailus, F. Su, D. Wang, and L. Jiang, "Hierarchically ordered macro-mesoporous TiO2-graphene composite films: Improved mass transfer, reduced charge recombination, and their enhanced photocatalytic activities," *ACS Nano*, vol. 5, no. 1, pp. 590–596, 2011.

[104] X. Xin, X. Zhou, J. Wu, X. Yao, and Z. Liu, “Scalable synthesis of TiO2/graphene nanostructured composite with high-rate performance for lithium ion batteries,” *ACS Nano*, vol. 6, no. 12, pp. 11035–11043, 2012.

[105] C. Zhang, U. Chaudhary, D. Lahiri, A. Godavarty, and A. Agarwal, “Photocatalytic activity of spark plasma sintered TiO2–graphene nanoplatelet composite,” *Scr. Mater.*, vol. 68, no. 9, pp. 719–722, 2013.

[106] Z. Zhang, W. Yang, X. Zou, F. Xu, X. Wang, B. Zhang, and J. Tang, “One-pot, solvothermal synthesis of TiO2–graphene composite nanosheets,” *J. Colloid Interface Sci.*, vol. 386, no. 1, pp. 198–204, 2012.

[107] L.-L. Tan, W.-J. Ong, S.-P. Chai, and A. R. Mohamed, “Reduced graphene oxide-TiO2 nanocomposite as a promising visible-light-active photocatalyst for the conversion of carbon dioxide.,” *Nanoscale Res. Lett.*, vol. 8, no. 1, p. 465, Jan. 2013.

[108] P. P. Patil, D. M. Phase, S. A. Kulkarni, S. V. Ghaisas, S. K. Kulkarni, S. M. Kanetkar, S. B. Ogale, and V. G. Bhide, “Pulsed-laser – induced reactive quenching at liquid-solid interface: Aqueous oxidation of iron,” *Phys. Rev. Lett.*, vol. 58, no. 3, pp. 238–241, Jan. 1987.

[109] H. S. Desarkar, P. Kumbhakar, and A. K. Mitra, “One-step synthesis of Zn/ZnO hollow nanoparticles by the laser ablation in liquid technique,” *Laser Phys. Lett.*, vol. 10, no. 5, p. 055903, May 2013.

[110] C. H. Liang, Y. Shimizu, T. Sasaki, and N. Koshizaki, “Preparation of ultrafine TiO2 nanocrystals via pulsed-laser ablation of titanium metal in surfactant solution,” *Appl. Phys. A Mater. Sci. Process.*, vol. 80, no. 4, pp. 819–822, 2005.

[111] M. A. Gondal, T. F. Qahtan, M. A. Dastageer, Y. W. Maganda, and D. H. Anjum, "Synthesis of Cu/Cu2O nanoparticles by laser ablation in deionized water and their annealing transformation into CuO nanoparticles.," *J. Nanosci. Nanotechnol.*, vol. 13, no. 8, pp. 5759–66, Aug. 2013.

[112] a. B. Hartanto, X. Ning, Y. Nakata, and T. Okada, "Growth mechanism of ZnO nanorods from nanoparticles formed in a laser ablation plume," *Appl. Phys. A Mater. Sci. Process.*, vol. 78, pp. 299–301, 2004.

[113] L. Yang, P. W. May, L. Yin, and T. B. Scott, "Growth of self-assembled ZnO nanoleaf from aqueous solution by pulsed laser ablation," *Nanotechnology*, vol. 18, no. 21, p. 215602, 2007.

[114] M. A. Gondal, Q. A. Drmosh, and T. A. Saleh, "Preparation and characterization of SnO2 nanoparticles using high power pulsed laser," *Appl. Surf. Sci.*, vol. 256, no. 23, pp. 7067–7070, 2010.

[115] Y. Mastai, R. Polsky, Y. Koltypin, a. Gedanken, and G. Hodes, "Pulsed sonoelectrochemical synthesis of cadmium selenide nanoparticles," *J. Am. Chem. Soc.*, vol. 121, no. 23, pp. 10047–10052, 1999.

[116] R. Zamiri, A. Zakaria, H. A. Ahangar, A. R. Sadrolhosseini, and M. A. Mahdi, "Fabrication of silver nanoparticles dispersed in palm oil using laser ablation.," *Int. J. Mol. Sci.*, vol. 11, no. 11, pp. 4764–4770, 2010.

[117] R. M. Tilaki, A. I. zad, and S. M. Mahdavi, "The effect of liquid environment on size and aggregation of gold nanoparticles prepared by pulsed laser ablation," *J. Nanoparticle Res.*, vol. 9, no. 5, pp. 853–860, 2006.

[118] a. V. Kabashin and M. Meunier, "Synthesis of colloidal nanoparticles during

femtosecond laser ablation of gold in water," *J. Appl. Phys.*, vol. 94, no. 12, pp. 7941–7943, 2003.

[119] F. Mafune, J. Kohno, Y. Takeda, and T. Kondow, "Formation of Stable Platinum Nanoparticles by Laser Ablation in Water," *J. Phys. Chem. B,* vol. 107, no. 18, pp. 4218–4223, 2003.

[120] Z. Yan, R. Bao, and D. B. Chrisey, "Excimer laser ablation of a Pt target in water: the observation of hollow particles.," *Nanotechnology*, vol. 21, no. 14, p. 145609, 2010.

[121] R. M. Tilaki, a. Iraji zad, and S. M. Mahdavi, "Size, composition and optical properties of copper nanoparticles prepared by laser ablation in liquids," *Appl. Phys. A*, vol. 88, no. 2, pp. 415–419, 2007.

[122] M. A. Gondal, M. A. Ali, M. A. Dastageer, and X. Chang, "CO2 Conversion into Methanol Using Granular Silicon Carbide (α6H-SiC): A Comparative Evaluation of 355 nm Laser and Xenon Mercury Broad Band Radiation Sources," *Catal. Letters,* vol. 143, no. 1, pp. 108–117, 2013.

[123] R. Berjoan, J. Rodriguez, and F. Sibieude, "AES study of the SiO2/SiC interface in the oxidation of CVD β-SiC," *Surf. Sci.*, vol. 271, no. 1–2, pp. 237–243, Jan. 1992.

[124] Y. Lee and M. Kang, "The optical properties of nanoporous structured titanium dioxide and the photovoltaic efficiency on DSSC," *Mater. Chem. Phys.*, vol. 122, no. 1, pp. 284–289, 2010.

[125] K. G. Deepa, P. Lekha, and S. Sindhu, "Efficiency enhancement in DSSC using metal nanoparticles: A size dependent study," *Sol. Energy,* vol. 86, no. 1, pp. 326–330, 2012.

[126] B. K, V. N. Singh, and N. S. John, “Hybrid materials of ZnO nanostructures with reduced graphene oxide and gold nanoparticles: Enhanced photodegradation rates in relation to their composition and morphology,” *Phys. Chem. Chem. Phys.*, Nov. 2015.

[127] P. Rodnyi and I. Khodyuk, “Optical and luminescence properties of zinc oxide (Review),” *Opt. Spectrosc.*, vol. 111, no. 5, pp. 776–785, 2011.

[128] W. Yu, Z. Zhang, K. Zhang, X. Teng, S. Wu, L. Zhang, M. Chen, and G. Fu, “Influence of Annealing on Photoluminescence of ZnO:Mn Thin Flims Grown by Sol-Gel Technique,” in *2009 Symposium on Photonics and Optoelectronics*, 2009, pp. 1–4.

[129] M. K. Kavitha, K. B. Jinesh, R. Philip, P. Gopinath, and H. John, “Defect engineering in ZnO nanocones for visible photoconductivity and nonlinear absorption.,” *Phys. Chem. Chem. Phys.*, vol. 16, no. 45, pp. 25093–100, Dec. 2014.

[130] C. Cheng, A. Amini, C. Zhu, Z. Xu, H. Song, and N. Wang, “Enhanced photocatalytic performance of TiO2-ZnO hybrid nanostructures.,” *Sci. Rep.*, vol. 4, p. 4181, Jan. 2014.

[131] M. A. Gondal, A. M. Ilyas, T. A. Fasasi, M. A. Dastageer, Z. S. Seddigi, T. F. Qahtan, M. Faiz, and G. D. Khattak, “Synthesis of Green TiO2/ZnO/CdS Hybrid Nano-catalyst for Efficient Light Harvesting using an Elegant Pulsed Laser Ablation in Liquids Method,” *Appl. Surf. Sci.*, Sep. 2015.

[132] R. Augustine, E. A. Dominic, I. Reju, B. Kaimal, N. Kalarikkal, and S. Thomas, “Electrospun polycaprolactone membranes incorporated with ZnO nanoparticles as

skin substitutes with enhanced fibroblast proliferation and wound healing," *RSC Adv.*, vol. 4, no. 47, p. 24777, Jun. 2014.

[133] W. N. Wang, I. W. Lenggoro, Y. Terashi, T. O. Kim, and K. Okuyama, "One-step synthesis of titanium oxide nanoparticles by spray pyrolysis of organic precursors," *Mater. Sci. Eng. B-Solid State Mater. Adv. Technol.*, vol. 123, no. 3, pp. 194–202, 2005.

[134] M. Sato, H. Hara, T. Nishide, and Y. Sawada, "A water-resistant precursor in a wet process for TiO2 thin film formation," *J. Mater. Chem.*, vol. 6, no. 11, p. 1767, Jan. 1996.

[135] E. Zaleta-Alejandre, M. Zapata-Torres, M. García-Hipólito, M. Aguilar-Frutis, G. Alarcón-Flores, J. Guzmán-Mendoza, and C. Falcony, "Structural and luminescent properties of europium doped TiO 2 thick films synthesized by the ultrasonic spray pyrolysis technique," *J. Phys. D. Appl. Phys.*, vol. 42, no. 9, p. 095102, May 2009.

[136] S. Dhara and P. K. Giri, "Quick single-step mechanosynthesis of ZnO nanorods and their optical characterization: milling time dependence," *Appl. Nanosci.*, vol. 1, no. 4, pp. 165–171, Sep. 2011.

[137] L. N. Dlamini, R. W. Krause, G. U. Kulkarni, and S. H. Durbach, "Photodegradation of bromophenol blue with fluorinated TiO2 composite," *Appl. Water Sci.*, vol. 1, no. 1–2, pp. 19–24, Jun. 2011.

[138] J. Li, F. Li, C. Li, G. Yang, Z. Xu, and S. Zhang, "Evidences of grain boundary capacitance effect on the colossal dielectric permittivity in (Nb + In) co-doped TiO2 ceramics.," *Sci. Rep.*, vol. 5, p. 8295, Jan. 2015.

[139] P. Zhang, X. Li, Q. Zhao, and S. Liu, "Synthesis and optical property of one-

dimensional spinel ZnMn2O4 nanorods.," *Nanoscale Res. Lett.*, vol. 6, no. 1, p. 323, Jan. 2011.

[140] H. Luo, H. Su, C. Dong, K. Xiao, and X. Li, "Electrochemical and passivation behavior investigation of ferritic stainless steel in simulated concrete pore media," *Data Br.*, Sep. 2015.

[141] G. Zorn, J. E. Baio, T. Weidner, V. Migonney, and D. G. Castner, "Characterization of poly(sodium styrene sulfonate) thin films grafted from functionalized titanium surfaces.," *Langmuir*, vol. 27, no. 21, pp. 13104–12, Nov. 2011.

[142] M. J. Jackman, A. G. Thomas, and C. Muryn, "Photoelectron Spectroscopy Study of Stoichiometric and Reduced Anatase TiO 2 (101) Surfaces: The Effect of Subsurface Defects on Water Adsorption at Near-Ambient Pressures," *J. Phys. Chem. C*, vol. 119, no. 24, pp. 13682–13690, Jun. 2015.

[143] D.-L. Sun, J.-R. Deng, and Z.-S. Chao, "Catalysis over zinc-incorporated berlinite (ZnAlPO4) of the methoxycarbonylation of 1,6-hexanediamine with dimethyl carbonate to form dimethylhexane-1,6-dicarbamate.," *Chem. Cent. J.*, vol. 1, p. 27, Jan. 2007.

[144] P. WEHNER, "XPS study of the reduction and reoxidation of ZnO-supported palladium," *J. Catal.*, vol. 88, no. 1, pp. 246–248, Jul. 1984.

[145] M. Wei, J. Wan, Z. Hu, B. Wang, and Z. Peng, "Synthesis, electron transfer and photocatalytic activity of TiO 2 nanotubes sensitized by meso-tetra(4-carboxyphenyl)porphyrin under visible-light irradiation," *RSC Adv.*, vol. 5, no. 72, pp. 58184–58190, Jul. 2015.

[146] H. Lu, W. Tian, J. Guo, and L. Li, “Interface Engineering through Atomic Layer Deposition towards Highly Improved Performance of Dye-Sensitized Solar Cells.,” *Sci. Rep.*, vol. 5, p. 12765, Jan. 2015.

[147] W.-Q. Wu, B.-X. Lei, H.-S. Rao, Y.-F. Xu, Y.-F. Wang, C.-Y. Su, and D.-B. Kuang, “Hydrothermal fabrication of hierarchically anatase TiO2 nanowire arrays on FTO glass for dye-sensitized solar cells.,” *Sci. Rep.*, vol. 3, p. 1352, Jan. 2013.

[148] T. K. Jana, A. Pal, and K. Chatterjee, “Self assembled flower like CdS–ZnO nanocomposite and its photo catalytic activity,” *J. Alloys Compd.*, vol. 583, pp. 510–515, Jan. 2014.

[149] S. Yan, L. Sun, Y. Sheng, N. Huang, and Z. Xiao, “Novel regrowth mechanism of CdS nanowire in hydrothermal synthesis,” *New J. Chem.*, vol. 35, no. 2, p. 299, 2011.

[150] L. N. Dlamini, R. W. Krause, G. U. Kulkarni, and S. H. Durbach, “Photodegradation of bromophenol blue with fluorinated TiO2 composite,” *Appl. Water Sci.*, vol. 1, no. 1–2, pp. 19–24, 2011.

[151] S. Sahoo and A. K. Arora, “Laser-power-induced multiphonon resonant Raman scattering in laser-heated CdS nanocrystal,” *J. Phys. Chem. B*, vol. 114, no. 12, pp. 4199–4203, 2010.

[152] A. G. Kontos, V. Likodimos, E. Vassalou, I. Kapogianni, Y. S. Raptis, C. Raptis, and P. Falaras, “Nanostructured titania films sensitized by quantum dot chalcogenides.,” *Nanoscale Res. Lett.*, vol. 6, no. 1, p. 266, Jan. 2011.

[153] M. I. Vasilevskiy, a G. Rolo, M. J. M. Gomes, O. V Vikhrova, and C. Ricolleau, “Impact of disorder on optical phonons confined in CdS nano-crystallites

embedded in a SiO2 matrix," *J. Physics-Condensed Matter*, vol. 13, no. 14, pp. 3491–3509, 2001.

[154] A. U. Ubale, K. S. Chipade, M. V. Bhute, P. P. Raut, G. P. Malpe, Y. S. Sakhare, and M. R. Belkhedkar, "Structural, Optical and Electrical Properties of Nanostructured CdS:CuS Composite Thin Films Grown by CBD Method," *International Journal of Materials and Chemistry*, vol. 2, no. 4. Scientific & Academic Publishing, pp. 165–172, 2012.

[155] R. Beranek and H. Kisch, "Tuning the optical and photoelectrochemical properties of surface-modified TiO2.," *Photochem. Photobiol. Sci.*, vol. 7, no. 1, pp. 40–8, Jan. 2008.

[156] S. S. Mali, C. a. Betty, P. N. Bhosale, and P. S. Patil, "Synthesis, Characterization of Hydrothermally Grown MWCNT-TiO2 Photoelectrodes and Their Visible Light Absorption Properties," *ECS J. Solid State Sci. Technol.*, vol. 1, no. 2, pp. M15–M23, 2012.

[157] B. C. Smith, *Infrared Spectral Interpretation: A Systematic Approach*. CRC Press, 1998.

[158] K. Gotoh, T. Kinumoto, E. Fujii, A. Yamamoto, H. Hashimoto, T. Ohkubo, A. Itadani, Y. Kuroda, and H. Ishida, "Exfoliated graphene sheets decorated with metal/metal oxide nanoparticles: Simple preparation from cation exchanged graphite oxide," *Carbon N. Y.*, vol. 49, pp. 1118–1125, 2011.

[159] L. ZHU, T. GHOSH, C.-Y. PARK, Z.-D. Meng, and W.-C. OH, "Enhanced Sonocatalytic Degradation of Rhodamine B by Graphene-TiO2 Composites Synthesized by an Ultrasonic-Assisted Method," *Chinese J. Catal.*, vol. 33, no. 7–

8, pp. 1276–1283, 2012.

[160] B. Choudhury, M. Dey, and A. Choudhury, “Defect generation, d-d transition, and band gap reduction in Cu-doped TiO2 nanoparticles,” *Int. Nano Lett.*, vol. 3, no. 1, p. 25, Apr. 2013.

[161] S. Zhang, H. Niu, Y. Lan, C. Cheng, J. Xu, and X. Wang, “Synthesis of TiO 2 Nanoparticles on Plasma-Treated Carbon Nanotubes and Its Application in Photoanodes of Dye-Sensitized Solar Cells,” *J. Phys. Chem. C*, vol. 115, no. 44, pp. 22025–22034, Nov. 2011.

[162] O. Baghriche, S. Rtimi, C. Pulgarin, C. Roussel, and J. Kiwi, “RF-plasma pretreatment of surfaces leading to TiO2 coatings with improved optical absorption and OH-radical production,” *Appl. Catal. B Environ.*, vol. 130–131, pp. 65–72, Feb. 2013.

[163] J. Yin, Q. Xu, Z. Wang, X. Yao, and Y. Wang, “Highly ordered TiO 2 nanostructures by sequential vapour infiltration of block copolymer micellar films in an atomic layer deposition reactor,” *J. Mater. Chem. C*, vol. 1, no. 5, pp. 1029–1036, Jan. 2013.

[164] F.-Z. Wang, D.-C. Shang, M.-G. Wang, S.-G. Hu, and Y.-Q. Li, “Incorporation and substitution mechanism of cadmium in cement clinker,” *J. Clean. Prod.*, 2015.

[165] J. (Jeanne) Yang, H. Cheng, and R. L. Frost, “Synthesis and characterisation of cobalt hydroxy carbonate Co2CO3(OH)2 nanomaterials,” *Spectrochim. Acta Part A Mol. Biomol. Spectrosc.*, vol. 78, no. 1, pp. 420–428, Jan. 2011.

[166] A. Celebioglu, S. Vempati, C. Ozgit-Akgun, N. Biyikli, and T. Uyar, “Water-soluble non-polymeric electrospun cyclodextrin nanofiber template for the

synthesis of metal oxide tubes by atomic layer deposition," *RSC Adv.*, vol. 4, no. 106, pp. 61698–61705, Nov. 2014.

[167] M. Xing, X. Li, and J. Zhang, "Synergistic effect on the visible light activity of Ti3+ doped TiO2 nanorods/boron doped graphene composite," *Sci. Rep.*, vol. 4, p. 5493, Jun. 2014.

[168] J. Yu, J. Jin, B. Cheng, and M. Jaroniec, "A noble metal-free reduced graphene oxide–CdS nanorod composite for the enhanced visible-light photocatalytic reduction of CO2 to solar fuel," *J. Mater. Chem. A*, vol. 2, no. 10, p. 3407, Feb. 2014.

[169] S. Sun, L. Gao, and Y. Liu, "Enhanced dye-sensitized solar cell using graphene-TiO[sub 2] photoanode prepared by heterogeneous coagulation," *Appl. Phys. Lett.*, vol. 96, no. 8, p. 083113, Feb. 2010.

[170] Z. Peining, A. S. Nair, P. Shengjie, Y. Shengyuan, and S. Ramakrishna, "Facile fabrication of TiO 2-graphene composite with enhanced photovoltaic and photocatalytic properties by electrospinning," *ACS Appl. Mater. Interfaces*, vol. 4, no. 2, pp. 581–585, 2012.

[171] T. Lan, H. Qiu, F. Xie, J. Yang, and M. Wei, "Rutile TiO2 mesocrystals/reduced graphene oxide with high-rate and long-term performance for lithium-ion batteries.," *Sci. Rep.*, vol. 5, p. 8498, Jan. 2015.

[172] J. Fan, S. Liu, and J. Yu, "Enhanced photovoltaic performance of dye-sensitized solar cells based on TiO2 nanosheets/graphene composite films," *J. Mater. Chem.*, vol. 22, no. 33, p. 17027, Jul. 2012.

[173] S. P. Lim, A. Pandikumar, N. M. Huang, and H. N. Lim, "Reduced graphene

oxide-titania nanocomposite-modified photoanode for efficient dye-sensitized solar cells," *Int. J. Energy Res.*, vol. 39, no. 6, pp. 812–824, May 2015.

[174] P. S. Chandrasekhar and V. K. Komarala, "Effect of graphene and Au@SiO 2 core–shell nano-composite on photoelectrochemical performance of dye-sensitized solar cells based on N-doped titania nanotubes," *RSC Adv.*, vol. 5, no. 103, pp. 84423–84431, Oct. 2015.

[175] U. Mehmood, S. Ahmed, I. A. Hussein, and K. Harrabi, "Improving the efficiency of Dye sensitized solar cells by TiO2–graphene nanocomposite photoanode," *Photonics Nanostructures - Fundam. Appl.*, vol. 16, pp. 34–42, Aug. 2015.

[176] S.-B. Kim, J.-Y. Park, C.-S. Kim, K. Okuyama, S.-E. Lee, H.-D. Jang, and T.-O. Kim, "Effects of Graphene in Dye-Sensitized Solar Cells Based on Nitrogen-Doped TiO 2 Composite," *J. Phys. Chem. C*, vol. 119, no. 29, pp. 16552–16559, Jul. 2015.

[177] G. Wei, W. Qin, G. Wang, J. Sun, J. Lin, R. Kim, D. Zhang, and K. Zheng, "The synthesis and ultraviolet photoluminescence of 6H–SiC nanowires by microwave method," *J. Phys. D. Appl. Phys.*, vol. 41, p. 235102, 2008.

[178] M. A. Gondal, M. A. Ali, X. F. Chang, K. Shen, Q. Y. Xu, and Z. H. Yamani, "Pulsed laser-induced photocatalytic reduction of greenhouse gas CO2 into methanol: A value-added hydrocarbon product over SiC.," *J. Environ. Sci. Health. A. Tox. Hazard. Subst. Environ. Eng.*, vol. 47, no. 11, pp. 1571–6, Jan. 2012.

[179] H. Zhang, W. Ding, K. He, and M. Li, "Synthesis and Characterization of Crystalline Silicon Carbide Nanoribbons.," *Nanoscale Res. Lett.*, vol. 5, no. 8, pp. 1264–1271, 2010.

[180] S. L. Zhang, B. F. Zhu, F. Huang, Y. Yan, E. Y. Shang, S. Fan, and W. Han, "Effect of defects on optical phonon Raman spectra in SiC nanorods," *Solid State Commun.*, vol. 111, no. 11, pp. 647–651, 1999.

[181] Y. Yao, S. T. Lee, and F. H. Li, "Direct synthesis of 2H–SiC nanowhiskers," *Chem. Phys. Lett.*, vol. 381, no. 5–6, pp. 628–633, Nov. 2003.

[182] T. Kaneko, D. Nemoto, A. Horiguchi, and N. Miyakawa, "FTIR analysis of a-SiC:H films grown by plasma enhanced CVD," *J. Cryst. Growth*, vol. 275, pp. 1097–1101, 2005.

[183] C. H. Huang, H. L. Bai, Y. L. Huang, S. L. Liu, S. I. Yen, and Y. S. Tseng, "Synthesis of Neutral SiO2/TiO2 Hydrosol and Its Application as Antireflective Self-Cleaning Thin Film," *Int. J. Photoenergy*, p. 8, 2012.

[184] H. F. Franzen, M. X. Umana, J. R. McCreary, and R. J. Thorn, "XPS spectra of some transition metal and alkaline earth monochalcogenides," *Journal of Solid State Chemistry*, vol. 18, no. 4. pp. 363–368, 1976.

[185] R. Castillo, B. Koch, P. Ruiz, and B. Delmon, "Influence of the Amount of Titania on the Texture and Structure of Titania Supported on Silica," *J. Catal.*, vol. 161, no. 2, pp. 524–529, Jul. 1996.

[186] L. I. Johansson, F. Owman, P. Martensson, C. Persson, and U. Lindefelt, "Electronic structure of 6H-SiC(0001)," *Phys. Rev. B*, vol. 53, no. 20, pp. 13803–13807, 1996.

[187] T. M. and S. Naritsuka, *Carbon Nanotubes - Synthesis, Characterization, Applications*. InTech, 2011.

[188] R. P. Netterfield, P. J. Martin, C. G. Pacey, W. G. Sainty, D. R. McKenzie, and G.

Auchterlonie, “Ion-assisted deposition of mixed TiO2-SiO2 films,” *J. Appl. Phys.*, vol. 66, no. 4, p. 1805, 1989.

[189] J. F. Moulder, W. F. Stickle, P. E. Sobol, and K. D. Bomben, *Handbook of X-ray Photoelectron Spectroscopy*, vol. 3, no. 4. 1979.

[190] “NIST X-ray Photoelectron Spectroscopy (XPS) Database, Version 3.5.” [Online]. Available: http://srdata.nist.gov/xps/Default.aspx. [Accessed: 27-Sep-2015].

[191] T. Narushima, T. Goto, T. Hirai, and Y. Iguchi, “High-temperature oxidation of silicon carbide and silicon nitride,” *Materials Transactions, JIM*, vol. 38, no. 10. pp. 821–835, 1997.

[192] K. Watari, H. Nakano, K. Sato, K. Urabe, K. Ishizaki, S. Cao, and K. Mori, “Effect of Grain Boundaries on Thermal Conductivity of Silicon Carbide Ceramic at 5 to 1300 K,” *J. Am. Ceram. Soc.*, vol. 86, no. 10, pp. 1812–1814, Oct. 2003.

[193] E. W. Wong, “Nanobeam Mechanics: Elasticity, Strength, and Toughness of Nanorods and Nanotubes,” *Science (80-.).*, vol. 277, no. 5334, pp. 1971–1975, Sep. 1997.

[194] S. Z. Deng, Z. B. Li, W. L. Wang, N. S. Xu, J. Zhou, X. G. Zheng, H. T. Xu, J. Chen, and J. C. She, “Field emission study of SiC nanowires/nanorods directly grown on SiC ceramic substrate,” *Appl. Phys. Lett.*, vol. 89, no. 2, p. 023118, 2006.

[195] Z. Pan, H.-L. Lai, F. C. K. Au, X. Duan, W. Zhou, W. Shi, N. Wang, C.-S. Lee, N.-B. Wong, S.-T. Lee, and S. Xie, “Oriented Silicon Carbide Nanowires: Synthesis and Field Emission Properties,” *Adv. Mater.*, vol. 12, no. 16, pp. 1186–1190, Aug. 2000.

[196] H. W. Shim, J. D. Kuppers, and H. Huang, “Strong friction of silicon carbide nanowire films.,” *Nanotechnology*, vol. 20, no. 2, p. 025704, Jan. 2009.

[197] X. D. Han, Y. F. Zhang, K. Zheng, X. N. Zhang, Z. Zhang, Y. J. Hao, X. Y. Guo, J. Yuan, and Z. L. Wang, “Low-temperature in situ large strain plasticity of ceramic SiC nanowires and its atomic-scale mechanism.,” *Nano Lett.*, vol. 7, no. 2, pp. 452–7, Mar. 2007.

[198] I. Garcia, J. Fransaer, and J.-P. Celis, “Electrodeposition and sliding wear resistance of nickel composite coatings containing micron and submicron SiC particles,” *Surf. Coatings Technol.*, vol. 148, no. 2–3, pp. 171–178, Dec. 2001.

[199] R. Govindaraj, R. Govindan, M. Geetha, and P. M. Anbarasan, “Structural, morphological and luminescence studies on pristine and La doped zinc oxide (ZnO) nanoparticles,” *Opt. - Int. J. Light Electron Opt.*, vol. 126, no. 17, pp. 1555–1558, Sep. 2015.

[200] B. Zhong, X. Tang, X. Huang, L. Xia, X. Zhang, G. Wen, and Z. Chen, “Metal–semiconductor Zn/ZnO core–shell nanocables: facile and large-scale fabrication, growth mechanism, oxidation behavior, and microwave absorption performance,” *CrystEngComm*, vol. 17, no. 14, pp. 2806–2814, Mar. 2015.

[201] F. Kayaci, C. Ozgit-Akgun, N. Biyikli, and T. Uyar, “Surface-decorated ZnO nanoparticles and ZnO nanocoating on electrospun polymeric nanofibers by atomic layer deposition for flexible photocatalytic nanofibrous membranes,” *RSC Adv.*, vol. 3, no. 19, p. 6817, Apr. 2013.

[202] F. Lv, C. Gao, P. Zhang, C. Dong, C. Zhang, and D. Xue, “Bipolar resistive switching behavior of CaTiO 3 films grown by hydrothermal epitaxy,” *RSC Adv.*,

vol. 5, no. 51, pp. 40714–40718, May 2015.

[203] B. Guo, Q. Zhang, G. Li, J. Yao, and C. Hu, “Aromatic C–N bond formation via simultaneous activation of C–H and N–H bonds: direct oxyamination of benzene to aniline,” *Green Chem.*, vol. 14, no. 7, p. 1880, Jul. 2012.

[204] X. Zhang, Y. Liu, K. Wang, M. Gao, and H. Pan, “Remarkably improved hydrogen storage properties of nanocrystalline TiO2-modified NaAlH4 and evolution of Ti-containing species during dehydrogenation/hydrogenation,” *Nano Res.*, vol. 8, no. 2, pp. 533–545, Jan. 2015.

[205] Z. Jin, L. Gao, Q. Zhou, and J. Wang, “High-performance flexible ultraviolet photoconductors based on solution-processed ultrathin ZnO/Au nanoparticle composite films.,” *Sci. Rep.*, vol. 4, p. 4268, Jan. 2014.

[206] J. Zhao, L. Liu, and F. Li, *Graphene Oxide: Physics and Applications*. Springer, 2014.

[207] C. Zhang, C. Feng, P. Zhang, Z. Guo, Z. Chen, S. Li, and H. Liu, “K 0.25 Mn 2 O 4 nanofiber microclusters as high power cathode materials for rechargeable lithium batteries,” *RSC Adv.*, vol. 2, no. 4, pp. 1643–1649, Jan. 2012.

[208] K. Koç, F. Z. Tepehan, and G. G. Tepehan, “Growth kinetics of MPS-capped CdS quantum dots in self-assembled thin films.,” *Nanoscale Res. Lett.*, vol. 7, no. 1, p. 610, Jan. 2012.

[209] L. Guo, X. Wang, C. Zhong, and L. Li, “Synthesis and photoluminescence of CdS QDs in ZrO 2 nanotubes by sequential chemical bath deposition,” *J. Phys. D. Appl. Phys.*, vol. 44, no. 16, p. 165403, Apr. 2011.

[210] D. Chen, Y. Du, H. Zhu, and Y. Deng, “Synthesis and characterization of a

microfibrous TiO2–CdS/palygorskite nanostructured material with enhanced visible-light photocatalytic activity,” *Appl. Clay Sci.*, vol. 87, pp. 285–291, Jan. 2014.

[211] D. Wang, Q. Wang, and T. Wang, “Shape controlled growth of pyrite FeS2 crystallites via a polymer-assisted hydrothermal route,” *CrystEngComm*, vol. 12, no. 11, p. 3797, Oct. 2010.

[212] H. Xu, Y. Yan, T. Wan, and S. Li, “Degradation properties of the electrostatic assembly PDLLA/CS/CHS nerve conduit.,” *Biomed. Mater.*, vol. 4, no. 4, p. 045006, Aug. 2009.

[213] J. H. Kim, K. Fu, J. Choi, K. Kil, J. Kim, X. Han, L. Hu, and U. Paik, “Encapsulation of S/SWNT with PANI web for enhanced rate and cycle performance in lithium sulfur batteries.,” *Sci. Rep.*, vol. 5, p. 8946, Jan. 2015.

[214] X. Han, Z. Zhao, Y. Xu, D. Liu, H. Zhang, and C. Zhao, “Synthesis and characterization of F-doped nanocrystalline Li 4 Ti 5 O 12 /C compounds for lithium-ion batteries,” *RSC Adv.*, vol. 4, no. 79, pp. 41968–41975, Aug. 2014.

[215] S. Muralikrishna, K. Sureshkumar, T. S. Varley, D. H. Nagaraju, and T. Ramakrishnappa, “In situ reduction and functionalization of graphene oxide with l -cysteine for simultaneous electrochemical determination of cadmium(ii), lead(ii), copper(ii), and mercury(ii) ions,” *Anal. Methods*, vol. 6, no. 21, pp. 8698–8705, Sep. 2014.

[216] R. Mu, A. Steigert, N. Lin, R. Wilks, M. Bär, and Y. Zhang, “The chemical structure of the ZnO/SiC heterointerface as revealed by electron spectroscopies,” *J. Phys. D. Appl. Phys.*, vol. 48, no. 30, p. 305304, Aug. 2015.

[217] V. Nirmal Kumar, R. Suryakarthick, S. Karuppusamy, M. Gupta, Y. Hayakawa, and R. Gopalakrishnan, “Effect of precursor concentration on the properties and tuning of conductivity between p-type and n-type Cu 1−X Cd X S 2 thin films deposited by a single step solution process as a novel material for photovoltaic applications,” *RSC Adv.*, vol. 5, no. 29, pp. 23015–23021, Feb. 2015.

VITAE

ILYAS ABDUL-MOJEED OLABISI

abdulmojeedilyas@yahoo.com
Oke-Itunu Estate, Olla Road ● Ejigbo, Osun State, Nigeria
Tel: 08033812090, +966533584746 (till Dec, 2015)

Objective: To strive for precision and excellence at all times

PERSONAL DETAILS

- Date of Birth: 21st Dec, 1986
- L.G.A: Ejigbo, Osun State
- Marital Status: Married
- Religion: Islam

EDUCATION

King Fahd University of Petroleum and Minerals**,** Saudi Arabia

M. S. in Physics, December 2015

Dissertation: Design and Fabrication of Dye sensitized solar cell using self-synthesized quaternary (TiO_2/ZnO/CdS/Graphene) nanocomposite by pulsed Laser ablation Technique

---

Ladoke Akintola University of Technology Ogbomoso, Nigeria,

B. Tech (Hons) in Pure and Applied Physics (**First Class Division**), December 2009

Dissertation: Frequency Response Hybridization Analysis of 8 DB Modified Log-Periodic Dipole Array Antenna Operating at 850-2000 MHz Band

---

Federal Government College Ogbomoso Oyo State, Nigeria.

West African Examination Council (WAEC) Certificate, **1997-2003**

RESEARCH INTEREST

- Synthesis of nanomaterials
- Fabrication of solar energy conversion devices like Dye sensitized solar cell
- Pulsed Laser Ablation in liquid
- Thin Film technology
- Photodegradation experiment
- Computational modeling of composite materials for photocatalytic applications

WORK/RESEARCH EXPERIENCE

King Fahd University of Petroleum and Minerals (KFUPM) Dhahran, Saudi Arabia

Department of Physics, Laser Research Group

Research Scientist, June 2013 to Dec. 2015

- Nanocomposite materials
- Dye sensitized solar cells
- Pulsed Laser Ablation in Liquid
- Water Photodegradation

Ladoke Akintola University of Technology (LAUTECH), Nigeria

Department of Pure and Applied Physics, Solid state physics/solar energy division

Teaching/ Graduate Research Assistant, June 2012 to 2014

- Synthesis of Oxide semiconductors
- Thin film deposition technique
- Organic solar cells

Federal University of Technology Yola (FUTY) – Adamawa State, Nigeria

Physics Department, **Research Assistant** (June2010 to June 2011).

- 100 level Tutor (Certificate of National Service (5th July, 2011))

Nigerian Television Authority (NTA) Ogbomoso –Oyo State, Nigeria

Engineering Department, **Transmitter Operator** (June2008 to Dec 2008).

LANGUAGE SKILLS

YORUBA (native language)

ENGLISH

COMPUTATIONAL SKILLS

Computational method: Spartan, X-ray photoelectron spectroscopy (XPS) analysis

Operating systems: Linux, Windows

Scientific Computing: Mathematica and Origin Pro

Microsoft Software: MS Office Suite

Analysis method: X-ray diffraction technique, Scanning electron microscope and Transmission electron microscope imaging, X-ray photoelectron spectroscopy (XPS), UV-Vis absorption, Photoluminescence, FTIR and Raman Spectroscopy.

AWARDS

First prize award (Golden Feather) – Sixth Student Conference: Engineering and Basic Science (Presentation), Saudi Arabia (2015)

Faculty Prize for Best Graduating Student in the faculty of Pure and Applied Science- Ladoke Akintola University of Technology, Ogbomoso Nigeria (2009)

PUBLICATIONS

M.A. Gondal, T.A. Fasasi, A. Mekki, T.A. Saleh, **A.M. Ilyas**, T.F. Qahtan, X. Chang, *Phase Transformation and Structural characterization studies of Aluminium Oxide* (Al_2O_3) *Nanoparticles synthesized using Pulsed Laser Ablation in Liquids Elegant Method*, Appl. Surf. Sci. (2015) (Accepted)

M.A. Gondal, **A.M. Ilyas**, T.A. Fasasi, M.A. Dastageer, Z.S. Seddigi, T.F. Qahtan, et al., *Synthesis of Green* TiO_2*/ZnO/CdS Hybrid Nano-catalyst for Efficient Light Harvesting using an Elegant Pulsed Laser Ablation in Liquids Method*, Appl. Surf. Sci. (2015). doi:10.1016/j.apsusc.2015.09.213.

A. M. Ilyas, M. A. Gondal, S. Akhtar, A. H. Shukri, T. Laoui, Z. H Yamani ,*Synthesis of graphene decorated* TiO_2 *nanohybrid for enhanced photovoltaic and photocatalytic properties using nanosecond pulsed laser ablation in Liquid* (subm. to Solar Energy Mat.)

A.M Ilyas, M.A Gondal, and Z.H Yamani, *Photo-chemical sensitization of* TiO_2 *using varied concentration of CdS and its solar application*. (Ready for submission)

A.M Ilyas, M.A Gondal, and Z.H Yamani, *Synthesis and Optimization of TiO2/ZnO nanocomposite catalyst using Pulsed Laser Ablation in liquid and its solar application.* (Ready for submission)

A.M Ilyas, M.A Gondal, , Z.H Yamani , M. Faiz *Photo-chemical reinforcement of* TiO_2 *using varied concentration of SiC and its solar application.* (Ready for submission)

A.M Ilyas, M.A Gondal, and Z.H Yamani, *Synthesis of quaternary $ZnO/TiO_2/CdS$/graphene nanocomposite used as photoanode in dye sensitized solar cell*. (Ready for submission)

A.M Ilyas, M.A Gondal, and Z.H Yamani, *Synthesis of entangled quaternary $ZnO/TiO_2/CdS/SiC$ nanocomposite used as photoanode in dye sensitized solar cell*. (Ready for submission)

M.A. Gondal, **A. M. Ilyas**, T.A. Fasasi, M.A. Dastageer ,T. F. Qahtan (2015) *Synthesis of Ag-ZnO Core-Shell Composite Structures Using Pulsed Laser Ablation in Liquids (PLAL) for Visible Light Applications*(under preparation)

A.A. Naqvi, F.Z., Khiari, M. Maslehuddin, M.A. Gondal, O.S.B Al-Amoudi, M.S. Ukashat, **A.M. Ilyas** et al., *Pulse height Tests of a large diameter fast $LaBr_3:Ce$ scintillation detector*, Applied Radiation and Isotopes (Elsevier)(2015)

CONFERENCE PRESENTATIONS AND POSTERS

A.M. Ilyas, M.A. Gondal, Z.H. Yamani *Pseudo-coded enhancement of ZnO photocatalytic property by pulsed laser quantum entanglement of $TiO_2/CdS/SiC$*, 4th Nano today conference (Accepted) (December 6-10, 2015**)**

M.A. Gondal, **A. M. Ilyas**, T.A. Fasasi, M.A. Dastageer ,T. F. Qahtan (2015) *Synthesis of Ag-ZnO Core-Shell Composite Structures Using Pulsed Laser Ablation in Liquids (PLAL) for Visible Light Applications,* Interantional Conference on Atomic, Molecular and Optical Physics (AMOP), Al-Jouf (31st march - 2ndApril, 2015)

M.A. Gondal, T.A. Fasasi, **A. M. Ilyas**, M.A. Dastageer, T. F. Qahtan (2015) *Synthesis and Characterization of Phase Transition of Al_2O_3 Nanoparticles Via Pulsed Laser Ablation in Liquids*, International Conference on Atomic, Molecular and Optical Physics (AMOP), Al-Jouf (31st march - 2ndApril, 2015)

Abdul-Mojeed O Ilyas *Novel Quantum dot Organic Paper Mache Solar cell optimized with Green Composite Catalyst synthesized using Pulsed Laser Ablation in Liquid,* Sixth scientific conference of Higher Education in KSA (2015)

Abdul-Mojeed O Ilyas *Fabrication of unique solar cell using Honey and Zinc oxide/Titanium oxide Nano-composite synthesized using Pulsed Laser Ablation*, 5th scientific conference of Higher Education in KSA (2014)

M. A. Gondal, **A.M. Ilyas**, and T. F. Qahtan**,** *Synthesis of ZnO-TiO_2 Nano-composites using pulsed Laser Ablation in Liquids (PLAL)*, Third Saudi International Meeting on Frontiers of Physics**,** Jazan University, Saudi Arabia (2014)

Abdulmojeed I, *Structural and optical characterization of ZnO nanoparticles synthesized using Different precursors,* Conference (Humboldt-Kolleg) Evolution of Nanotechnology, Nanomedicine and Nanotoxicology Research in Nigeria; a call for multidisciplinary collaborations (2013)